Using scanning Doppler lidar to enhance aviation safety in Iceland

Shu Yang

Doctor of Philosophy in Applied Sciences

October 2021

School of Technology

Reykjavík University

Ph.D. Dissertation

Using scanning Doppler lidar to enhance aviation safety in Iceland

Dissertation of 30 ECTS credits submitted to the School of Technology
at Reykjavík University in partial fulfillment of
the requirements for the degree of
Doctor of Philosophy (Ph.D.) in Applied Sciences

October 2021

Thesis Committee:

Dr. David C. Finger, Supervisor
Asst. Professor, Reykjavík University.
Iceland
Head of the Technology Department,
Energy Institute at the Johannes Kepler
University. Linz, Austria

Dr. Sibylle von Löwis of Menar, Supervisor
Weather observation networks group leader,
Icelandic Meteorological Office.
Iceland

Dr. Guðrún Nína Petersen, Supervisor
Atmospheric Scientist, Icelandic
Meteorological Office. Iceland

Dr. Maxime Hervo, Examiner
Meteo Swiss, Switzerlan

Using scanning Doppler lidar to enhance aviation safety in Iceland

Dissertation submitted in partial fulfillment of Doctor of Philosophy in Applied Sciences

Department of Engineering
School of Technology
Reykjavik University
Menntavegur 1
102, Reykjavik
Iceland

Telephone: +354 599 6200
Author ORCID: 0000-0001-5763-431X
ISBN: 978-9935-9620-4-1

Using scanning Doppler lidar to enhance aviation safety in Iceland

Shu Yang

July 2021

Abstract

Lidar systems have been used widely to measure wind profiles and atmospheric aerosols. The scanning Doppler lidars operated by the Icelandic Meteorological Office can provide continuous measurements of the wind velocity and direction based on the Doppler effect, from the emitted signal, as well as the backscatter coefficient and depolarization ratio for retrieving aerosol properties. In this project, we investigate the use of Doppler lidars in Iceland, especially for enhancing aviation safety. The project was divided into three main tasks have been conducted: 1) atmospheric turbulence measurements; 2) airborne aerosol detection; 3) real-time lidar signal classification with machine learning algorithms. In the first task, an algorithm was developed based on the Kolmogorov theory to retrieve eddy dissipation rate, as an indicator of turbulence intensity, from lidar wind measurements. The method was tested on two cases from 2017. In the second task, the Doppler lidar was used in combination with ceilometers, a sun-photometer and other instruments, to detect aerosols, including dust and volcanic ash in Iceland. In the third task, both supervised and unsupervised machine learning algorithms were developed to identify the noise signal and classify the lidar measurements, with the aim of providing real-time lidar signal classification for potential end-users. The results indicate that the Doppler lidar can significantly improve aviation safety and complement meteorological measurements by detecting atmospheric turbulence or volcanic ash clouds in Iceland.

Key words

Doppler lidar, Iceland, atmospheric turbulence, aerosols, dust, machine learning

Notkun skanna dopplerliða til að auka flugöryggi á Íslandi

Shu Yang

júlí 2021

Útdráttur

Vind- og agnasjár (e. lidar) hafa verið notaðar víða til að mæla vindsnið og nema svifryk og aðrar agnir í lofthjúpnum. Veðurstofa Ísland á tvo Doppler agnasjár sem geta veitt samfelldar mælingar á vindhraða og -stefnu, byggðar á Dopplerhrifa, og endurkastsstuðul og tvípólunarhlutfall (e. depolarization ratio) agna. Í þessu verkefni var könnuð notkun Doppler agnasjár á Íslandi til að auka flugöryggi. Verkefninu var skipt niður í þrjá verkþætti: i) ókyrrðarmælingar í jaðarlaginui; ii) svifryk og aðrar agnir í lofthjúpnum; iii) rauntímaflokkun agna með vélrænu námi (e. machine learning). Í verkþætti i) var þróuð reikniaðferð byggð á kenningu Kolmogorov til að meta sveipeyðingarákefð (e. eddy dissipation rate) frá vindmælingum, sem vísbendingu um ókyrrðarstyrk Aðferðin var prófuð í tveimur tilvikum frá árið 2017. Í verkþætti ii) voru gögn frá Doppler agnasjánni notuð, með gögnum úr skýjahæðamæli, sólarljósamæli og öðrum tækjum til að greina svifryk, þar með talið ryk og eldfjallaösku á Íslandi. Í verkþættii iii) var þróaðvélrænt nám, bæði undir eftirliti og án eftirlits, til að bera kennsl á suð og flokka mælingarnar með það að markmiði að veita rauntímaliðaflokkun fyrir hugsanlega notendur. Niðurstöðurnar benda til þess að Doppler vind- og agnasjá geti bætt verulega flugöryggi og verið góð viðbót við hefðbundnari veðurmælingar á Íslandi, með því að greina ókyrrð og öskuí lofti.

Lykilorð

Doppler vind- og agnasjá, Ísland, ókyrrð í lofti, agnir í lofthjúp, ryk, vélrænt nám

The undersigned hereby certify that they recommend to the School of Technology, Department of Engineering, Reykjavík University for acceptance this Dissertation entitled **Using scanning Doppler lidar to enhance aviation safety in Iceland** submitted by **Shu Yang** in partial fulfillment of the requirements for the degree of **Doctor of Philosophy (Ph.D.) in Applied Sciences**

.....
date

.....
Dr. David C. Finger, Supervisor
Asst. Professor, Reykjavík
University. Iceland
Head of the Technology
Department, Energy Institute at the
Johannes Kepler University, Linz,
Austria

.....
Dr. Sibylle von Löwis of Menar, Supervisor
Weather observation networks group leader,
Icelandic Meteorological Office.
Iceland

.....
Dr. Guðrún Nína Petersen,
Supervisor
Atmospheric Scientist,
Icelandic Meteorological Office.
Iceland

.....
Dr. Maxime Hervo, Examiner
Meteo Swiss, Switzerland

The undersigned hereby grants permission to the Reykjavík University Library to reproduce single copies of this Dissertation entitled **Using scanning Doppler lidar to enhance aviation safety in Iceland** and to lend or sell such copies for private, scholarly or scientific research purposes only.

The author reserves all other publication and other rights in association with the copyright in the Dissertation, and except as herein before provided, neither the Dissertation nor any substantial portion thereof may be printed or otherwise reproduced in any material form whatsoever without the author's prior written permission.

.....

date

.....

Shu Yang
Doctor of Philosophy

I dedicate this to my love Jing, who supported me in every possible way.

Acknowledgements

This work was funded by ISAVIA. Additional equipment, data and facilities were generously donated by Icelandic Meteorological Office (IMO) and Reykjavik University (RU).

I would like to thank the following people, without whom I cannot finish my Ph.D. research:

I would like to thank my primary supervisor, Dr. David C. Finger, who guided me on all aspects as a Ph.D., students: how to do a research, how to collaborate with others, how to write a paper, how to present my work, how to communicate with the public, and how to become an independent researcher.

I would like to thank my supervisors from IMO, Dr. Guðrún Nína Petersen and Dr. Sibylle von Löwis, who gave me countless advices regarding my work, my papers, and also led me the way to know the amazing country Iceland better.

I would like to thank Dr. Ewan O'Connor, who welcomed me in Helsinki and truly showed me the beauty of lidar this amazing instrument.

I would like to thank Dr. Jana Preißler and Dr. Ludovic Thobois from Leosphere, who offered tremendous technical support and insightful suggestions regarding the lidar measurement.

I would like to especially thank Dr. Matthias Wiegner, who was a really respected person I have met. He generously offered his help when the first time we met in Vienna and continuously supported me since then. He always cared about my Ph.D. and unfortunately I cannot finish before he left us. He will be deeply missed by me forever.

I would like to thank Mr. Fengchao Peng who generously agreed to help me with the machine learning when I approach him as a really noob on this topic, and shared a lot of great research ideas.

I would like to thank Dr. Pavla Dagsson Waldhauserova who shared her experience and knowledge about the dust in Iceland, and her kindly invitation to let me present my work within the community.

Besides, I would like to thank the following people, without whom I cannot survive the 5 years in Iceland alone:

I would like to thank Miao, Qin, Zichun, Jinkai, Qiongna, Yan, Yuxi, Yonatan, Vijay from RU; and Tingting, Siqi, Anton, Xue, Han, Zhiqian, from HI. I really enjoyed the time spent with these lovely people.

I would like to thank Verity and Sigrun from RU who kindly supported my study and work in the university.

I would like to thank Ke Chuck Xiao who visited me in a dark wintertime. Hope he can graduate as a Ph.D. soon.

I would like to thank my parents, who supported me fully and remotely, and also for the visiting in 2019 to encourage me.

Last but not the least, I would like to thank Jing, who supported me before, during the Ph.D. Without her encouragement, I cannot even finish this by 2020.

Preface

This dissertation is original work by the Shu Yang et al. (2020 a,b, 2021), of which I am the author. The three work will be presented in three chapters (Chapter 2, 3, and 4) separately.

The published three papers are:
Yang, S., Petersen, G. N., von Löwis, S., Preißler, J., & Finger, D. C. (2020). Determination of eddy dissipation rate by Doppler lidar in Reykjavik, Iceland. Meteorological Applications, 27(5), e1951.
Yang, S., Preißler, J., Wiegner, M., von Löwis, S., Petersen, G. N., Parks, M. M., & Finger, D. C. (2020). Monitoring Dust Events Using Doppler Lidar and Ceilometer in Iceland. Atmosphere, 11(12), 1294.
Yang, S., Peng, F., von Löwis, S., Petersen, G. N., & Finger, D. C. (2021). Using Machine Learning Methods to Identify Particle Types from Doppler Lidar Measurements in Iceland. Remote Sensing, 13(13), 2433.

Contents

List of Abbreviations

ICAO International Civil Aviation Organization
Ph.D. Doctor of Philosophy
Lidar Light Detection And Ranging
EARLINET European Aerosol Research Lidar Network
EDR Eddy Dissipation Rate
IMO Icelandic Meteorological Office
VAD velocity-azimuth-display
LOS line of sight
CNR carry to noise ratio
CI confidence index
FFT Fast Fourier transform
UTC Coordinated Universal Time
RVK Reykjavik
KEF Keflavik
AWS automatic weather station
RCS range corrected signal
AOD aerosol optical depth
AERONET Aerosol Robotic Network
PM Particulate Matter
RH relative humidity
DBSCAN density-based spatial clustering of applications with noise
CALIPSO Cloud-Aerosol Lidar and Infrared Pathfinder Satellite Observation
RF Random Forest
SVM support Vector Machine
LUT look up table
TP true positive
TF true negative
FP False positive
FN False negative
TPR True Positive Rate
PPV Positive Predictive Values
FDR False discovery rates
FNR False Negative Rate

Chapter 1

Introduction

1.1 Background

Air traffic is an important transportation way, especially for long-distance and timeliness trips, such as passengers transport. According to the annual report of the ICAO (International Civil Aviation Organization, (ICAO, 2019)), 4.4 billion passengers were recorded travelling all around the world in 2019. Especially for insular nations, like Iceland, air traffic plays an important role for the local population and economy.

Increasing air traffic requires increasing aviation safety levels. Aviation safety is affected by two main factors, i) mechanical maintenance of the airplanes and ii) meteorological conditions in the airspace. This Ph.D. project focuses on the detection and monitoring the aviation-related meteorological factors, i.e. atmospheric turbulence and airborne aerosols, using a relatively new observing system: a ground-based lidar (Light Detection And Ranging) system.

It is the first time that a Doppler lidar was deployed in Iceland for atmospheric science research, which will deepen the knowledge of lidar's performance in a subpolar region like Iceland. The local observation can provide the most in time information for the lidar users, from meteorologists to air traffic controllers. Besides, the lidar measurement in Iceland can be supplementary to a broader remote sensing network, e.g. the European Aerosol Research Lidar Network, EARLINET.

1.2 Wind measurement by lidar in Iceland

As weather could severely impact aviation operations, people realized that an accurate meteorology observation and forecast is important for aviation safety back in 1900s, e.g. (Dines, 1917). The most common meteorological parameter that is related to aircraft accidents is wind and turbulences (Gultepe et al., 2019).

Iceland is known for extreme and highly variable weather conditions with frequent strong winds and gusts exceeding 25 m/s (Ólafsson et al., 2007; Ólafsson and Ágústsson, 2007). The crossing-shaped runway in the main international airport, Keflavik International

Airport, makes it more frequent to encounter crosswinds, which makes the airport an ideal location for aircraft manufacturers to test new aircraft (Norris, 2019). An accurate observation of the wind field thus could enhance aviation safety for sure. With the help of Doppler wind lidar, it is possible to provide the air traffic controller with a real-time wind measurement with high temporal and spatial resolution. With this high-resolution measurement, identify the hazardous atmospheric turbulence is achievable.

Atmospheric turbulence is considered as small scale, irregular air motion, i.e. rapid irregular change in wind direction and/or speed, which can be generated by mechanical or thermal processes. Several airports around the world have installed Doppler lidar to detect and quantify atmospheric turbulences (Chan, 2010; Misaka et al., 2008). In Europe, it has been proven that commercial Doppler lidar can be used for wind measurement (Thobois et al., 2015; Tuononen et al., 2017; Wächter & Rettenmeier, 2009). It is the first time in Iceland to explore the use of Doppler lidar in Iceland on wind measurement, and a method of wind component retrieval and atmospheric turbulence intensity quantification is developed.

1.3 Atmospheric aerosols observation by lidar in Iceland

The atmospheric aerosols can also impact aviation safety. The most hazardous situation is that the volcanic ash could have a significant impact on jet aircraft's engine performance, flight safety and maintenance cost (Chen & Zhao, 2015). In 2010, the explosive eruption of Eyjafjallajokull in South Iceland caused severe air traffic disruption and great economic loss (Gudmundsson et al., 2010; G. N. Petersen et al., 2012). The ash clouds of Eyjafjallajokull have been observed by multiple lidar stations in Europe (A. Ansmann et al., 2010; Bukowiecki et al., 2011; Grant et al., 2012; Wiegner et al., 2012). As one of the most active volcanic region, volcanic eruptions occur on average every three to five years (Thordarson & Larsen, 2007), thus a lidar observation that closes to the eruption will deepen the understanding of lidar measurement on volcanic ash as well as prevent the possible accident during/after an eruption.

Besides the volcanic ash, atmospheric aerosols may also reduce visibility. Iceland comprises a large sandy desert in the central plateau, covering 22,000 km2, almost one-fifth of the country (Arnalds et al., 2016). The subarctic weather in Iceland is characterized by strong wind events (Ólafsson et al., 2007) due to the frequent passing of low-pressure systems and associated weather fronts. This results in wind erosion leading to frequent dust storms, and on average there are 135 days of dust events annually (Dagsson-Waldhauserova et al., 2014).

The lidar is emitting a laser beam and receives the signals scattered by particles in the atmosphere, i.e. airborne aerosols, cloud droplets. Researchers can retrieve the scatterers' properties by analyzing the different variables from backscatter signals, depending on the type of instrument. Lidar has become a popular instrument to observe airborne aerosols around the world, since it can perform a continuous measurement in various weather conditions (e.g. Ansmann et al., 2010; Balis et al., 2000; Huang et al., 2008; Rogers et al., 2009; Shimizu, 2004). In Iceland, two Doppler lidars equipped with depolarization channel are deployed for aerosol measurement since 2014. It is the first time to explore the ability of aerosol observation by these unique lidar systems, and also the first time to perform a ground-based aerosol lidar measurement in Iceland.

1.4 Doppler lidars in Iceland

A lidar system is an active remote sensing instrument, which is becoming more and more popular in different sectors, such as auto-driven cars' sensor (Gao et al., 2018), forestry (Dubayah & Drake, 2000), civil engineering structure monitoring (Brook et al., 2010). In meteorology, lidar is usually used in wind observation (Bilbro et al., 1984; Chan, 2012; Gryning et al., 2017) and aerosol and cloud detection (Albert Ansmann & Müller, 2005; Burton et al., 2012), depending on the type of lidar. In Iceland, we are using two WindCube 200S Doppler lidar from Leosphere (Leosphere, Inc, 2013). These two models and identical to other WindCube lidars, but equipped with depolarization modules, which allow the lidar user to estimate the shape of the targets. Meanwhile, it means the measurement of these lidars need to be further evaluated, for the potential on aerosol observation of the depolarization channel, and the first time that a Doppler lidar is used for wind and aerosols measurement in Iceland.

1.5 Research tasks and outline

The main purpose of this Ph.D. project is to explore the potential of using Doppler lidar in Iceland on meteorological research and evaluating the use of lidar to enhance aviation safety. Considering the designed ability of lidar and the climate conditions and realistic needs in Iceland, two research targets are identified: 1. Using Doppler lidar to detect severe atmospheric turbulence; 2. Using Doppler lidar to detect airborne aerosols. These two tasks are demonstrated in Chapter 2 and Chapter 3 accordingly.

In Chapter 2, an algorithm has been developed to retrieve the Eddy Dissipation Rate (EDR), which is an indicator of atmospheric turbulence intensity. The results are examined in two case studies and compared with an existed method. In Chapter 3, the Doppler lidar measurement is combined and compared with measurements by other instruments for dust detection. A whole method to process, calibrate and correct lidar instruments and data has been developed. Besides, to help the less-trained lidar users reading the lidar results efficiently, a machine learning-based classification method has been developed. With this method, a near-real-time classification can be deployed and the lidar user can easily understand what they are looking at. This part is described in Chapter 4. In the last Chapter, a conclusion of the whole project is given.

The thesis explored the use of Doppler lidar in Iceland on meteorology research and evaluated its value for enhancing aviation safety in Iceland. The performance of the instrument has been assessed, the methods to achieve each particular task have been developed and well described, and suggestions were given to apply all this knowledge for operation.

1.6 References

Ansmann, A., & Müller, D. (2005). Lidar and Atmospheric Aerosol Particles. In C. Weitkamp (Ed.), Lidar: Range-Resolved Optical Remote Sensing of the Atmosphere (pp. 105–141). Springer. https://doi.org/10.1007/0-387-25101-4_4

Ansmann, A., Tesche, M., Groß, S., Freudenthaler, V., Seifert, P., Hiebsch, A., Schmidt, J., Wandinger, U., Mattis, I., Müller, D., & Wiegner, M. (2010). The 16 April 2010 major volcanic ash plume over central Europe: EARLINET lidar and AERONET photometer observations at Leipzig and Munich, Germany: EYJAFJOLL ASH PLUME OVER EUROPE. Geophysical Research Letters, 37(13), n/a-n/a. https://doi.org/10.1029/2010GL043809

Balis, D., Papayannis, A., Galani, E., Marenco, F., Santacesaria, V., Hamonou, E., Chazette, P., Ziomas, I., & Zerefos, C. (2000). Tropospheric LIDAR aerosol measurements and sun photometric observations at Thessaloniki, Greece. Atmospheric Environment, 34(6), 925–932. https://doi.org/10.1016/S1352-2310(99)00317-9

Bilbro, J., Fichtl, G., Fitzjarrald, D., Krause, M., & Lee, R. (1984). Airborne Doppler Lidar Wind Field Measurements. Bulletin of the American Meteorological Society, 65(4), 348–359. https://doi.org/10.1175/1520-0477(1984)065<0348:ADLWFM>2.0.CO;2

Brook, A., Ben-Dor, E., & Richter, R. (2010). Fusion of hyperspectral images and LiDAR data for civil engineering structure monitoring. 2010 2nd Workshop on Hyperspectral Image and Signal Processing: Evolution in Remote Sensing, 1–5. https://doi.org/10.1109/WHISPERS.2010.5594872

Bukowiecki, N., Zieger, P., Weingartner, E., Jurányi, Z., Gysel, M., Neininger, B., Schneider, B., Hueglin, C., Ulrich, A., Wichser, A., Henne, S., Brunner, D., Kaegi, R., Schwikowski, M., Tobler, L., Wienhold, F. G., Engel, I., Buchmann, B., Peter, T., & Baltensperger, U. (2011). Ground-based and airborne in-situ measurements of the Eyjafjallajokull volcanic aerosol plume in Switzerland in spring 2010. Atmospheric Chemistry and Physics, 11(19), 10011–10030. https://doi.org/10.3929/ethz-b-000160998

Burton, S. P., Ferrare, R. A., Hostetler, C. A., Hair, J. W., Rogers, R. R., Obland, M. D., Butler, C. F., Cook, A. L., Harper, D. B., & Froyd, K. D. (2012). Aerosol classification using airborne High Spectral Resolution Lidar measurements – methodology and examples. Atmospheric Measurement Techniques, 5(1), 73–98. https://doi.org/10.5194/amt-5-73-2012

Chan, P. W. (2010). LIDAR-based turbulence intensity calculation using glide-path scans of the Doppler LIght Detection And Ranging (LIDAR) systems at the Hong Kong International Airport and comparison with flight data and a turbulence alerting system. Meteorologische Zeitschrift, 19(6), 549–563. https://doi.org/10.1127/0941-2948/2010/0471

Chan, P. W. (2012). Application of LIDAR-based F-factor in windshear alerting. Meteorologische Zeitschrift, 21(2), 193–204. https://doi.org/10.1127/0941-2948/2012/0321

Chen, W. R., & Zhao, L. R. (2015). Review – Volcanic Ash and its Influence on Aircraft Engine Components. Procedia Engineering, 99, 795–803. https://doi.org/10.1016/j.proeng.2014.12.604

Dagsson-Waldhauserova, P., Arnalds, O., & Olafsson, H. (2014). Long-term variability of dust events in Iceland (1949–2011). Atmospheric Chemistry and Physics, 14(24), 13411–13422. https://doi.org/10.5194/acp-14-13411-2014

Dines, W. H. (1917). METEOROLOGY AND AVIATION. Monthly Weather Review, 45(8), 401–401. https://doi.org/10.1175/1520-0493(1917)45<401b:MAA>2.0.CO;2

Dubayah R. O., & Drake J. B. (2000). Lidar Remote Sensing for Forestry. Journal of Forestry, 98(6), 44–46. https://doi.org/10.1093/jof/98.6.44

Gao, H., Cheng, B., Wang, J., Li, K., Zhao, J., & Li, D. (2018). Object Classification Using CNN-Based Fusion of Vision and LIDAR in Autonomous Vehicle Environment. IEEE Transactions on Industrial Informatics, 14(9), 4224–4231. https://doi.org/10.1109/TII.2018.2822828

Grant, A. L. M., Dacre, H. F., Thomson, D. J., & Marenco, F. (2012). Horizontal and vertical structure of the Eyjafjallajökull ash cloud over the UK: A comparison of airborne lidar observations and simulations. Atmospheric Chemistry and Physics, 12(21), 10145–10159. https://doi.org/10.5194/acp-12-10145-2012

Gryning, S.-E., Mikkelsen, T., Baehr, C., Dabas, A., Gómez, P., O'Connor, E., Rottner, L., Sjöholm, M., Suomi, I., & Vasiljević, N. (2017). Measurement methodologies for wind energy based on ground-level remote sensing. In Renewable Energy Forecasting (Kariniotakis, George, pp. 29–56). Elsevier. https://doi.org/10.1016/B978-0-08-100504-0.00002-0

Gudmundsson, M. T., Pedersen, R., Vogfjörd, K., Thorbjarnardóttir, B., Jakobsdóttir, S., & Roberts, M. J. (2010). Eruptions of Eyjafjallajökull Volcano, Iceland. Eos, Transactions American Geophysical Union, 91(21), 190–191. https://doi.org/10.1029/2010EO210002

Gultepe, I., Sharman, R., Williams, P., Zhou, B., Ellrod, G., Minnis, P., Trier, S., Griffin, S., Yum, S. S., Gharabaghi, B., Feltz, W., Temimi, M., Pu, Z., Storer, L., Kneringer, P., Weston, M. J., Chuang, H., Thobois, L., Dimri, A. P., … Neto, F. L. A. (2019). A review of high impact weather for aviation meteorology. Pure and Applied Geophysics, 176(5), 1869–1921.

ICAO. (2019). Annual Report 2019. International Civil Aviation Organization (ICAO). https://www.icao.int/annual-report-2019/Pages/default.aspx

Jian-Ping, H., Zhong-Wei, H., Jian-Rong, B., Wu, Z., & Lei, Z. (2008). Micro-Pulse Lidar Measurements of Aerosol Vertical Structure over the Loess Plateau. Atmospheric and Oceanic Science Letters, 1(1), 8–11. https://doi.org/10.1080/16742834.2008.11446756

Leosphere, Inc. (2013). WINDCUBE 100s-200s User Manual.

Misaka, T., Ogasawara, T., Obayashi, S., Yamada, I., & Okuno, Y. (2008). Assimilation Experiment of Lidar Measurements for Wake Turbulence. Journal of Fluid Science and Technology, 3(4), 512–518. https://doi.org/10.1299/jfst.3.512

Petersen, G. N., Bjornsson, H., & Arason, P. (2012). The impact of the atmosphere on the Eyjafjallajökull 2010 eruption plume. Journal of Geophysical Research: Atmospheres, 117(D20). https://doi.org/10.1029/2011JD016762

Rogers, R. R., Hair, J. W., Hostetler, C. A., Ferrare, R. A., Obland, M. D., Cook, A. L., Harper, D. B., Burton, S. P., Shinozuka, Y., McNaughton, C. S., Clarke, A. D., Redemann, J., Russell, P. B., Livingston, J. M., & Kleinman, L. I. (2009). NASA LaRC airborne high spectral resolution lidar aerosol measurements during MILAGRO: Observations and validation. Atmospheric Chemistry and Physics, 9(14), 4811–4826. https://doi.org/10.5194/acp-9-4811-2009

Shimizu, A. (2004). Continuous observations of Asian dust and other aerosols by polarization lidars in China and Japan during ACE-Asia. Journal of Geophysical Research, 109(D19). https://doi.org/10.1029/2002JD003253

Thobois, L. P., Krishnamurthy, R., Loaec, S., Cariou, J. P., Dolfi-Bouteyre, A., & Valla, M. (2015, June 22). Wind and EDR Measurements with Scanning Doppler LIDARs for Preparing Future Weather Dependent Separation Concepts (Invited). 7th AIAA

Atmospheric and Space Environments Conference. 7th AIAA Atmospheric and Space Environments Conference, Dallas, TX. https://doi.org/10.2514/6.2015-3317

Thordarson, T., & Larsen, G. (2007). Volcanism in Iceland in historical time: Volcano types, eruption styles and eruptive history—ScienceDirect. Journal of Geodynamics, 43(1), 118–152. https://doi.org/10.1016/j.jog.2006.09.005

Tuononen, M., O'Connor, E. J., Sinclair, V. A., & Vakkari, V. (2017). Low-Level Jets over Utö, Finland, Based on Doppler Lidar Observations. Journal of Applied Meteorology and Climatology, 56(9), 2577–2594. https://doi.org/10.1175/JAMC-D-16-0411.1

Wächter, M., & Rettenmeier, A. K. (2009). Characterization of short time fluctuations in atmospheric wind speeds by LIDAR measurements. Meteorologische Zeitschrift, 277–280. https://doi.org/10.1127/0941-2948/2009/0376

Wiegner, M., Gasteiger, J., Groß, S., Schnell, F., Freudenthaler, V., & Forkel, R. (2012). Characterization of the Eyjafjallajökull ash-plume: Potential of lidar remote sensing. Physics and Chemistry of the Earth, Parts A/B/C, 45–46, 79–86. https://doi.org/10.1016/j.pce.2011.01.006

Chapter 2

Turbulence intensity measurement by Doppler lidar

2.1 Introduction

Extreme weather phenomena can have hazardous impacts on aviation safety. In particular, rapid changes in headwinds and crosswinds during aircraft take-off or landing can lead to critical situations, which may jeopardize human lives. This is due to the low airspeed and low altitude of aircraft, only allowing minor corrective measures to be made to adjust for turbulence (Hon and Chan, 2014). According to the safety report of the International Civil Aviation Authorities (ICAO), more than one-third of aircraft accidents in 2017 occurred during take-off and landing (ICAO, 2018).

Iceland, located in the North Atlantic Ocean, is well known for extreme and highly variable weather conditions with frequent strong winds and gusts exceeding 25 m/s (Ólafsson et al., 2007; Ólafsson and Ágústsson, 2007). This often raises aviation safety concerns. However, the frequency of high crosswinds has also made Keflavik International Airport an ideal location for aircraft manufacturers to test new aircrafts (Norris, 2019). Thus, weather conditions in Iceland make the detection of turbulence for enhanced aviation safety a priority.

Any small scale, irregular air motion, i.e. rapid irregular change in wind direction and/or speed can be considered atmospheric turbulence. Atmospheric turbulence can be generated by mechanical processes such as wind shear, surface roughness, friction, wind jets, and obstacles or thermal processes such as buoyancy produced by surface heating or cloud-top radiative cooling. Accordingly, turbulences are directly related to the surface roughness and atmospheric stability.

The scale of atmospheric eddies ranges from the synoptic scale (thousands of kilometers) to microscale (tens of meters). The eddies that affect aviation the most have a spatial scale between about 100 m and 1 km (Sharman and Lane, 2016). Conventional instruments, such as anemometers mounted on meteorological masts can detect local turbulence only at the location of the instrument, providing limited information about the spatial distribution of turbulences in the vicinity of airports. On the other hand, radio soundings, which measure a vertical profile through the atmosphere, may reveal the vertical distribution of turbulence but are limited to when and where the sonde is released. To detect and quantify turbulence and obtain a clear picture of the wind conditions, several international airports, e.g. Hong Kong (Chan, 2010) and Sendai (Misaka et al., 2008), have added light detection and ranging (lidar) systems to their Aviation Weather Observation Systems.

The use of commercial lidars for ground-based remote sensing of wind has become

increasingly important in the last decade (Sathe and Mann, 2013). In addition to being used in the aviation sector (Hon and Chan, 2014; Leung et al., 2018), lidars are also widely used in the wind energy sector (Wächter and Rettenmeier, 2009) as well as in wind-related meteorological research (Tuononen et al., 2017; Manninen et al., 2018). Compared to the use of in-situ methods like anemometers and radio sounding, lidars have the advantage of making continuous measurements with high temporal and spatial resolution. Lidars also allow the monitoring of wind fields within and above the boundary layer without the need for masts. Furthermore, tall masts may not be desirable in some places, e.g. at airports. Another advantage is that lidars are quite compact and mobile, therefore, can be deployed at different locations.

Previous studies focusing on turbulence detection using Doppler lidars have encompassed investigations ranging from a purely theoretical approach to practical research. Frehlich (2001), Frehlich and Cornman (2002) and Frehlich et al. (2006) reported their development of a method to estimate turbulence intensity from the Kolmogorov theory while Smalikho and his colleagues explored the turbulence detection by continuous wave and pulsed Doppler lidars (Smalikho et al., 2005; Smalikho and Banakh, 2017; Stephan et al., 2018). In Europe, several studies have been conducted on the retrieval of eddy dissipation rate (EDR) as the indicator of turbulence intensity from lidar datasets, although some use ε [m^2 s^{-3}], e.g. O'Connor et al. (2010), and some use $\varepsilon^{-1/3}$ [$m^{2/3}$ s^{-1}], e.g. Thobois et al. (2015) and Muñoz-Esparza et al. (2018). At Hong Kong International Airport, lidars have been applied to detect low-level turbulence (Chan, 2009; Hon and Chan, 2014; Leung et al., 2018). However, the use of lidars for turbulence intensity detection in high latitude regions, such as in Iceland, has received little attention. The atmospheric turbulence in Iceland is typically characterised by strong wind fields, weather fronts, accentuated wind shear and blizzards. The volcanic geology leads to additional turbulence near the numerous steep mountains and low temperatures result in a shallow mixing layer. All these factors make the application of lidar observations in Iceland relevant and urgent. However, the atmosphere is often relatively clean, which may reduce the backscatter signal of emitted light pulses and result in a reduction of the measurement range of the lidar measurement.

O'Connor et al. (2010) developed an algorithm to retrieve EDR from vertical lidar scans, hereafter called vertical stares, as the beam is kept in the vertical position. However, the horizontal wind velocity is generally an order of magnitude larger than vertical velocity and of importance for aviation due to the head- and tailwind variations (Sinclair and Kuhn, 1991) as well as high crosswinds. Accordingly, in this study we develop an algorithm to retrieve the eddy dissipation rate (EDR) as an indicator of turbulence intensity from horizontal wind measurement by lidar in Reykjavik, Iceland.

We used a Leosphere Windcube 200S Doppler lidar system (Leosphere, 2013) located at the headquarters of the Icelandic Meteorological Office (IMO) in Reykjavik, Iceland. The results are compared to vertical stares using the method of O'Connor et al. (2010). Additionally, we discuss different data filtering methods and compare two calculation approaches.

2.2 Methodology

2.2.1 Instruments

Two identical lidar systems, Leosphere Windcube 200S Doppler scanning lidars with

depolarization functionality, are currently in operation in Iceland (Table 1). One system is located at Keflavik International Airport and the other system is a mobile system, installed on a trailer. In this study, we only use data from the mobile system, which was located at IMO's headquarters in Reykjavik (64.1275° N, 21.9027° W) for the duration of this study. The site in an urban location in the centre of the capital region and the local impact on the wind climate is due to buildings and urban vegetation.

Table 2.1 The specifications of the lidars operated in Iceland (Leosphere, 2013).

	Specification
Company	LEOSPHERE – A Vaisala Company
Website:	http://www.leosphere.com
Model	Windcube 200S
Wavelength	1.54 µm
Maximum Power	5 mW
Pulse Width	200 ns
Range resolution	50 m
Pulse rate frequency	20 kHz
Maximum detection range	12 km
Minimum detection range	100 m
Azimuthal angle range	0—360°
Elevation angle range	-10—190 °

A Doppler lidar can measure radial wind speed along the beam based on the Doppler effect, often termed Doppler velocity. Utilizing the Doppler lidar system we can retrieve profiles of wind speed, wind direction, and estimate EDR, as explained in detail in Section 2.2.3.

2.2.2 Scan settings

The lidar systems can be programmed to scan the surrounding atmosphere. The scan strategy used in this study is described as follows:

- Every 15 minutes two 360° revolution conic shaped velocity-azimuth-display (VAD) scans were performed at elevation angles of 75° and 15°.
- The transverse interval (azimuthal resolution) during VAD scans was 30°, resulting in 12 beams for each scan. The accumulation time for each beam was 5 s. In total, one conic VAD scan with 12 beams took approximately 70 s (including 10 s due to change the azimuth angles).
- Between VAD scans, vertical stares were performed continually with a 1 s accumulation time per profile.

As the lidar measures the radial wind velocity, along the line of sight (LOS), both vertical

stares and VAD scans can acquire information on EDR. Firstly, we will focus on the VAD scans and an approach that has been documented extensively in the literature (see e.g. Frehlich et al., 2006; Hon and Chan, 2014; Thobois et al., 2015). The horizontal wind component, which is of importance for aviation safety and the focus of this study, can be derived from the VAD scans, while the data from vertical stares is only used as a verification reference in this study.

2.2.3 Theory on turbulence estimation

Turbulence is defined as a highly irregular movement of fluid. Given the range of length and time scales of eddies, it is challenging to describe the motion physically. One approach to measure turbulence is using the Kolmogorov theory (Kolmogorov, 1962; 1991). According to the Kolmogorov theory, the energy is injected into the turbulent medium from the larger spatial scales and forms eddies. Eddies break down into smaller eddies until the kinetic energy is dissipated to thermal energy by the viscous properties of the medium. The dissipation rate, i.e. EDR, can be used as a turbulence intensity indicator (Hocking, 1985; Cohn, 1994). There are several approaches to retrieve EDR value from lidar observations. For example, Frehlich and Cornman (2002) estimated EDR and the length scale from velocity data while Nijhuis et al. (2019) compared different methods to retrieve EDR from wind velocity, obtained from Doppler radar. Also, Smalikho and Banakh (2017) estimated EDR using azimuthal structure function and Thobois et al. (2015) explored the possibility to estimate EDR by using a Leosphere Windcube lidar in Toulouse, France. In this study, we developed an algorithm to estimate EDR by using the velocity structure function and apply the algorithm on our lidar data obtained in Reykjavik. This method is based on the Kolmogorov theory (Frehlich, 2001), which assumes that the atmosphere is isotropic and homogeneous over the observation domain. In Sect 3.1 we will discuss the homogeneity of the atmosphere.

The radial velocity V_r, as measured by a Doppler lidar, can be given by Eq. 2.1:

$$V_r = U sin\varphi cos\theta + V cos\varphi cos\theta + W sin\theta \quad \text{(Eq. 2.1)}$$

where U, V, and W are the wind components in ms^{-1} in x, y, and z-direction, φ is the azimuthal angle (with 0° pointing to the north) and θ the elevation angle (with 90° pointing vertically), see Figure 2.1. With a fixed elevation angle scan, the radial velocity V_r is a sinusoidal function of the azimuthal angle. Finding the fitting parameters of the observed values with respect to this model gives us the three-dimensional wind field. The coefficient of determination R^2 can be used as an indicator of the homogeneity of the atmosphere (Päschke et al., 2015), defined as:

$$R^2 = 1 - \sum_i (V_{ri} - \tilde{V}_{ri})^2 / \sum_i (V_{ri} - \bar{V}_r)^2 \quad \text{(Eq. 2.2)}$$

with $\tilde{V}_{ri}$ denoting the radial velocities from sine fit, or theoretical velocities, and $\bar{V}_r$ denoting the average of measured radial velocities V_{ri} of one VAD scan (i = 1, 2, ..., 12). Larger R^2 values indicate that the VAD velocity is close to the sine fit, which means the atmosphere is approximately homogeneous.

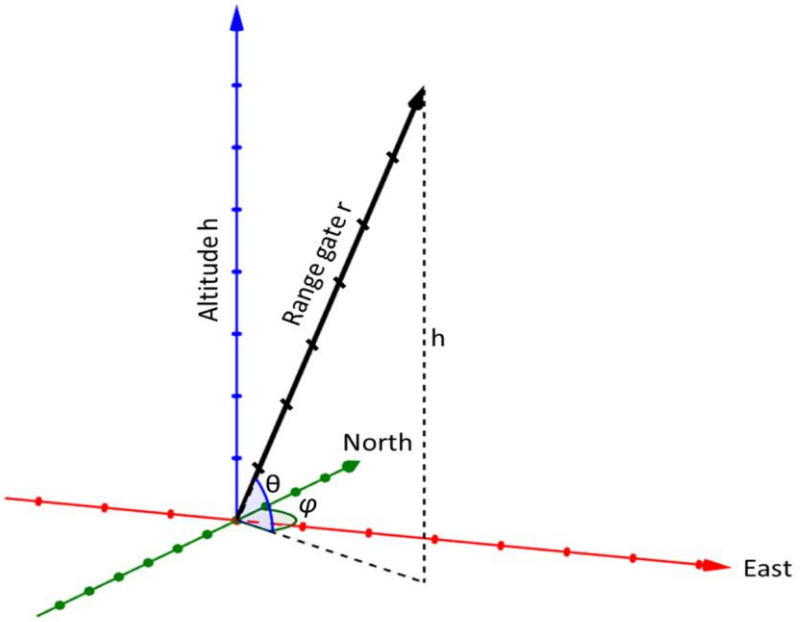

Figure 2.1 A schematic of the lidar beam vector (black). The azimuth angle, φ, is shown in green with north being 0° and the elevation angle, θ, in blue with 90° representing a vertical beam. h is the altitude of the range gate, and r is the distance along the beam.

If the atmosphere is homogeneous and isotropic, the Kolmogorov theory can be applied and the energy spectrum (power density as a function of frequency) should fit a -5/3 slope (Figure 2.2):

$$E(k) = C\varepsilon^{2/3}k^{-5/3} \quad \text{(Eq. 2.3)}$$

where C is the Kolmogorov constant, ε is EDR and k is the wavenumber, which is proportional to frequency f.

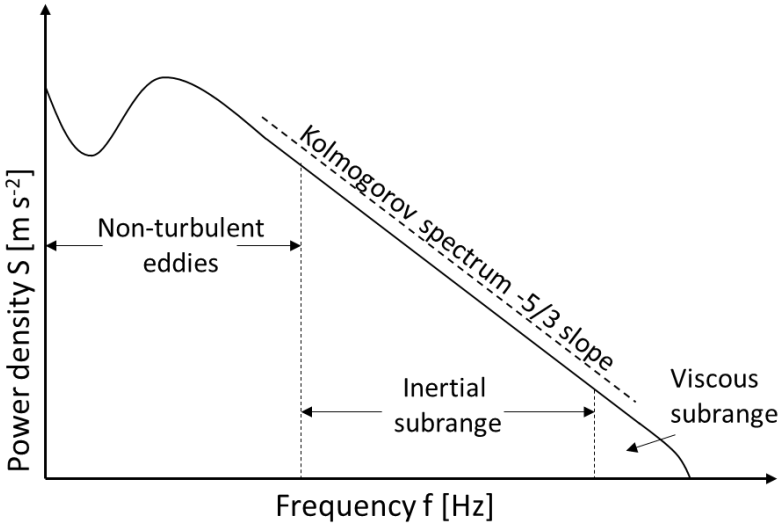

Figure 2.2 A schematic of the wind velocity power density as a function of frequency conforming to Kolmogorov's hypothesis. The inertial subrange is the part of the power spectrum where energy is transferred to smaller scales by turbulence. For three-dimensional turbulence, the power spectrum is theoretically proportional to $k^{-5/3}$, where k is the wavenumber. Redrawn from O'Connor et al. (2010) and Thobois et al. (2015).

If the atmosphere is isotropic and the slope of the power density to the frequency in a log-log figure is close to -5/3 (Figure 2.2), a direct relationship between the energy spectrum $E(K)$ and the structure-function D_v can be defined (Frehlich et al., 2006; Thobois et al., 2015). For a scanning lidar, EDR (ε, in $m^2 s^{-3}$) can be obtained by fitting the -5/3 slope to the structure-function, leading to:

$$D_v = C_v \varepsilon^{2/3} s^{2/3} \qquad \text{(Eq. 2.4)}$$

where $C_v \sim 2$ is the Kolmogorov constant.

The velocity structure-function D_v is given by Eq. 2.5:

$$D_v = < (v'(r) - v'(r+s))^2 > \qquad \text{(Eq. 2.5)}$$

where

$$v'(r) = v(r) - < v(r) > \qquad \text{(Eq. 2.6)}$$

are the fluctuations from the mean velocity $< v(r) >$ at a specific range gate r, which should follow the fitted sine curve (Frehlich et al., 2006) and s is the spatial difference. The curve fit varies for different range gates, it is typically better at lower range gates where there is less noise. The distance to range gate r can easily be converted to height h using trigonometric functions.

The structure-function can be estimated either along a transverse direction (one azimuth angle to another), which is the azimuthal approach or along the lidar beam direction (one range gate to another), which is the longitudinal approach. Accordingly, s varies based on the approach: for azimuthal approach, it is the distance between the two points at the same range gate on adjacent beams, ($s = r \cdot \sin(\Delta\varphi) \sin(0.5(\pi - \Delta\varphi))^{-1}$, $\Delta\varphi$ *is the azimuthal interval*), which varies between range gates, and for the longitudinal approach, it is equivalent to the range gate width, which is 50 m in this study. Thus, to calculate the average value, using the azimuthal approach, 12 profiles are averaged at each range gate. In contrast, for the longitudinal approach, a moving average is applied along each profile. A comparison between the two approaches is presented in Section 2.4.

Besides the VAD scans, data from the vertical stares were used in this study for verification, applying the method of O'Connor et al. (2010). This work retrieved EDR based on the same theory but utilized the Doppler velocity variances of vertical stares, combined with estimated horizontal wind speed, which gives an estimation of length scale.

2.3 Data exploitation

2.3.1 Data screening

The radial wind velocity dataset from the lidar contains scan information, time, measured radial velocity, deviation of radial velocity, carrier-to-noise ratio (CNR) and confidence index (CI). We selected two days for case studies: 24 March 2017 as the turbulent case and 31 March 2017 as the calm case.

Firstly, we investigated if the observed velocity energy spectra, derived from vertical stare data using a Fast Fourier Transform (FFT) method, agreed with the expected -5/3 slope. The

shape of the measured energy spectrum not only depends on the meteorological conditions and altitude but also the airflow directions (Pauscher et al., 2016). In general, the energy spectrum fits the idealized slope better at a lower altitude, due to the distribution of energy pulses over ranges. Figure 2.3 shows two examples of one-hour vertical stare data on 24 March 2017, at different altitudes (450 m and 1950 m). As expected, the lidar performs poorly on wind velocity with a weaker signal at higher heights (Frehlich, 2001). The lidar signal is governed by the signal backscattering from particles in the atmosphere. Thus signal quality is better at a lower altitude, where the aerosol concentration is high (Ramanathan et al., 2001). In high latitude regions like Iceland, the mixing layer is generally shallower than at continental mid-latitude sites, and the number of scatterers is relatively small (O'Connor, personal communication, April 2017). This explains the lower CNR at a high range and it may also contribute to the bias.

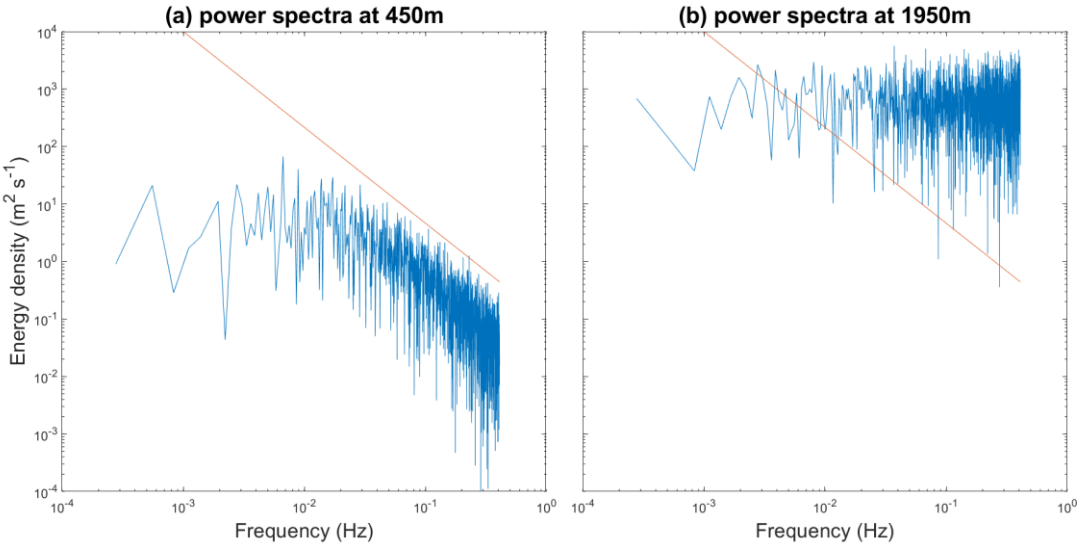

Figure 2.3 Verification of data quality: the velocity energy spectrum (blue curve, derived from the vertical velocity profile) should correspond to a -5/3 slope (red line). A good example (a) versus a bad example (b) from the same day (24 March 2017). Data from different altitudes (450 m for (a) and 1950 m for (b)). Both are averaged over one hour (16:00 to 17:00). The mean CNR value is -4.3 dB (a) and -32 dB(b).

In general, we use CNR as an indicator of the backscatter signal intensity. The CNR value depends on the backscatter and extinction coefficient of atmospheric aerosols (Boquet et al., 2016), and high CNR value is expected with the increasing aerosol load. Weather conditions, e.g. the mixing process, also impact the CNR level. In the cases shown in Figure 2.3, the mean CNR is -4.3 dB at 450 m and -32 dB at 1950 m height above ground. To exclude the impact of noise, CNR is used for data screening in many studies (Boquet *et al.*, 2016; Gryning et al., 2016, 2017). In addition to using CNR to screen noise and invalid data, the CI can also be applied. Radial wind at each time- and range-step is determined by computing the spectrum using an FFT method, and subsequently fitting this spectrum to a theoretical curve. The CI threshold depends on CNR, mean error, and spectrum broadening of this spectral fit. CI is factory calibrated individually for each lidar system and each range gate length. The calibration requires a few hours of noise measurements, where outgoing radiation is shielded from the receiver telescope. The CI threshold is then set to a value that limits the false positive rate to 0.25% (Dabas, 1999). For the scans applied here, CI is a binary quality control parameter returning the value 0 for rejected data points and 100 for valid data points.

Manninen et al. (2016) estimated the uncertainty introduced by noise when they quantified turbulence intensity from lidar data and they developed a background correction algorithm to increase data availability. We have applied this algorithm on the lidar data from vertical stare, but it is not implemented for VAD scans. The most commonly used CNR threshold for other lidar systems is -22 dB (Frehlich, 1996; Gryning et al., 2016, 2017), or -27 dB for Windcube 200S (Boquet et al., 2016). However, there are indications that those thresholds might be too high for Iceland since the atmosphere is often quite clean and, subsequently, the number of scatterers small. To determine the best data screening threshold for our lidars, we have implemented a sensitivity test of different CNR values and CI values. We have applied different thresholds to data obtained on two selected dates, then calculated the data availability ($DA = available\ data\ points/total\ data\ points \times 100\%$) and mean R^2 value (see Eq. 2.2). A larger DA value indicates more data points were kept, while a larger R^2 value indicates the kept data points have a higher quality (based on the fit to the sine curve, see Section 2.3). In general, a higher CNR threshold results in improved data quality (larger R^2 value) but fewer data points (smaller DA value). This is to be expected as there is always a trade-off between data availability and data quality when determining an optimal CNR threshold. Figure 2.4 shows results from a sensitivity test of data quality and availability, depending on CNR. We found that during a turbulent day the data quality and amount of data retrieved are higher than during a calm day, and low elevation scans have improved data quality compared to high elevation scans. This is reasonable since the atmosphere is better mixed on turbulent days and more scatterers are expected at lower altitudes since the main source of scatterers is the surface. In our study, we use a CNR threshold of -32 dB because this corresponds to a cut-off point for DA and R^2 value changes for every curve in Figure 2.4: the improvement of R^2, and the decrease of DA, is less sensitive when CNR is larger than -32 dB, compared to smaller than -32 dB.

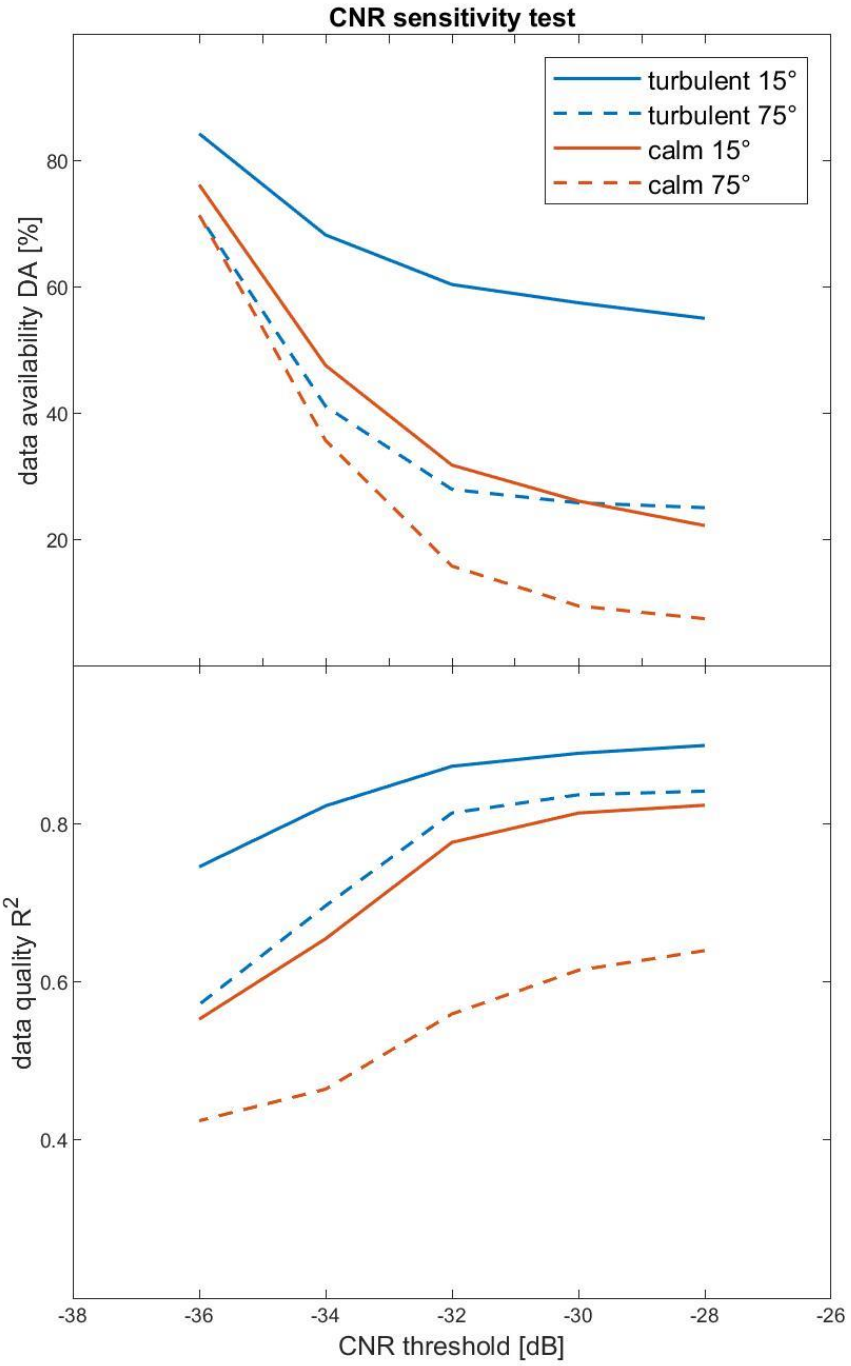

Figure 2.4 CNR sensitivity test results. Blue and red curves represent the data availability on a turbulent and calm day, 24 and 31 March 2017 respectively. The solid lines indicate VAD scans at a 15° elevation angle and the dashed lines at a 75° elevation angle.

As CI is provided by the lidar system and it depends on the factory settings, we cannot investigate its sensitivity. In Table 2 we present a comparison between CNR and CI thresholds. The CI threshold would correspond to a CNR threshold between -32 and -30 dB. In this study, we use a combination of CNR ≥ -32 dB and CI = 100. Any data points which do not meet these conditions are discarded.

Table 2.2 *Comparison of DA and R^2 for CNR and CI thresholds applied on data from a turbulent day (24 March 2017) and a calm day (31 March 2017) at two elevation angles.*

date	2017-03-24				2017-03-31			
elevation angle	15°		75°		15°		75°	
CNR	DA [%]	R^2	DA [%]	R^2	DA [%]	R^2	DA [%]	R^2
-30	57.54	0.8895	25.85	0.8370	26.13	0.8139	9.51	0.6150
-32	60.43	0.8731	27.97	0.8140	31.82	0.7768	15.82	0.5597
CI=100	58.91	0.8826	26.55	0.8303	28.73	0.8020	12.04	0.5952

Figure 2.5 displays the effect of the data screening filter. Figure 2.5(a) and 2.5(b) show CNR and CI on 24 March 2017. The calculated EDR (longitudinal approach) without any filter is shown in Figure 2.5(c), and the result of data screening applied before calculating EDR in Figure 2.5(d). The figure shows that while the filter removes noise, it retains the majority of quality measurements.

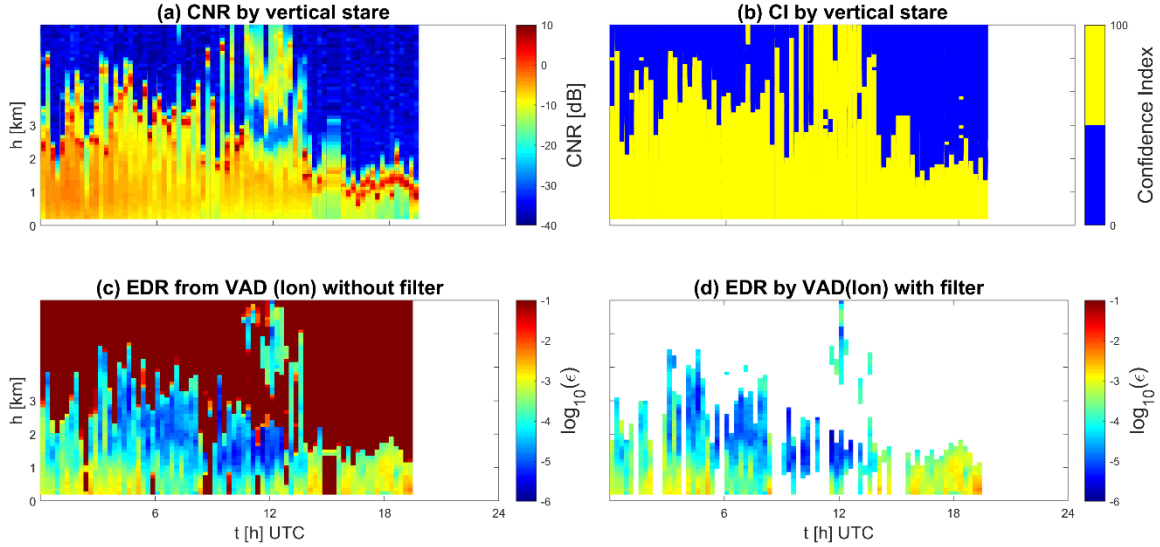

Figure 2.5 Carrier-to-noise ratio (CNR) in dB (a), the Confidence Index (CI) (b), the base-10 logarithm of EDR [m^2 s^{-3}] without filter (c) and with filter (d) on 24 March 2017. The EDR is derived from VAD scans, at a 75° elevation angle and using the longitudinal approach. Note that in this case, no data is available after 20 UTC.

2.3.2 Error analysis

For modern commercial lidars, the instrumental error is negligible (Sathe and Mann, 2013). The main error contributions are from random errors and systematic errors (Lenschow et al., 1994). Due to the lack of reference measurements/numerical models, we calculate the relative errors (Smalikho and Banakh, 2017) of derived eddy dissipation rate:

$$\mathrm{E} = \sqrt{< (\frac{\varepsilon}{<\varepsilon>} - 1)^2 >} \times 100\% \qquad \text{(Eq. 2.7)}$$

We calculate the one hour mean relative error for a general estimate, as shown in Figure 2.3(a): from 16:00 to 17:00 UTC, 24 March 2017, at an altitude of around 450 m. The relative error of EDR reaches 20.2% of the calculated EDR for a 75° elevation angle and 9.8% for a 15° elevation angle. These results are comparable to the results from Smalikho and Banakh (2017), which are 15-20%. The mean relative error at the same altitude is smaller with 15° elevation angle, which is reasonable since the 15° elevation angle has

higher R^2 value with the same CNR threshold. The poor fit to Kolmogorov's theory shown in Fig 3(b) has been filtered out by data screening (Section 2.3.1).

2.4 Results and discussion

The wind fields on March 24 and 31 are shown in figure 2.6. The wind velocity on these two days varied significantly: on March 24, the wind direction changed from westerlies exceeding 20 m s-1 to the southerly wind of 10 m s-1; on March 31 northerly winds of 5 m s-1 dominated throughout the day.

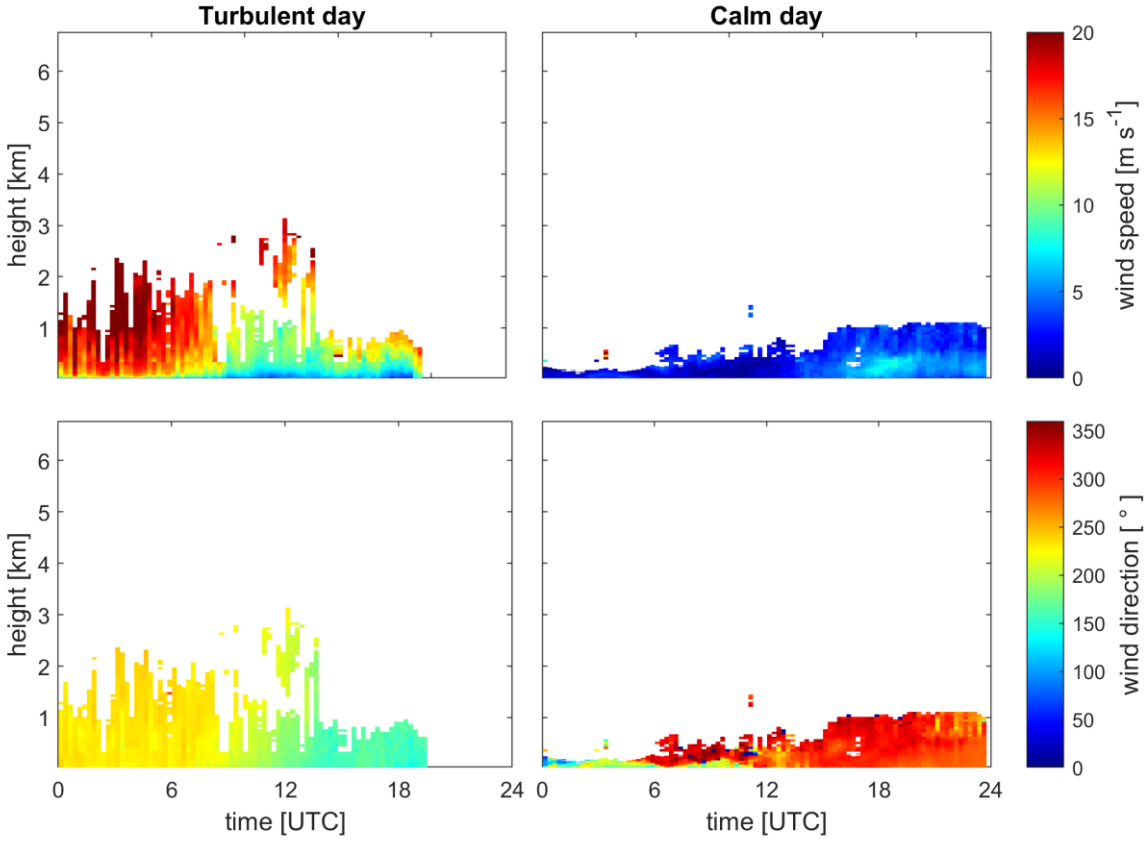

Figure 2.6 Wind speed ([m s^{-1}], top row) and wind direction ([°], bottom row) measured by the lidar on March 24 (left panel) and March 31(right panel), 2017.

The received lidar backscattered signal is directly related to the size and number of particles in the atmosphere. From Figure 2.5 and previous publications (e.g., O'Connor et al., 2010), we know that the strongest signal comes from the well-mixed boundary layer, the height of which can vary from tens of meters to a few kilometres (Stull, 1988) and consequently, the effective detection height of lidar measurement can also vary. After applying the EDR retrieval algorithm to lidar data, Figure 2.7 shows a comparison of the derived EDR on the selected dates using different scan strategies (vertical to VAD), structure functions (azimuthal to longitudinal approach), elevation angles (75° to 15°), and during different weather conditions (turbulent and calm). Note that to distinguish variations in EDR the units are shown as log10(ε). As expected, the boundary layer is more extended in turbulent conditions compared to calm conditions, due to a stronger vertical mixing process. This explains why there is a clear difference in detection height between the more turbulent day (Figure 2.7, left panel) where the maximum detection height is about 3.5 km altitude and the calm day (Figure 2.7, right panel) where it is only about 1.5 km. As mentioned above,

we use the VAD scans at two elevation angles, 15°, and 75°. From the basic geometry, a higher elevation angle results in higher maximum and minimum detection altitude, with a constant detection range. Thus, a low elevation scan provides more information at a lower altitude. Under optimal conditions, the lidar can retrieve backscattered signal up to the top of the boundary layer, and additional layers of scatterers further aloft, e.g. the cloud around 12 UTC on 24 March at an altitude between 2 to 3 km from figure 2.7(a), 2.7(e) and 2.7(i).

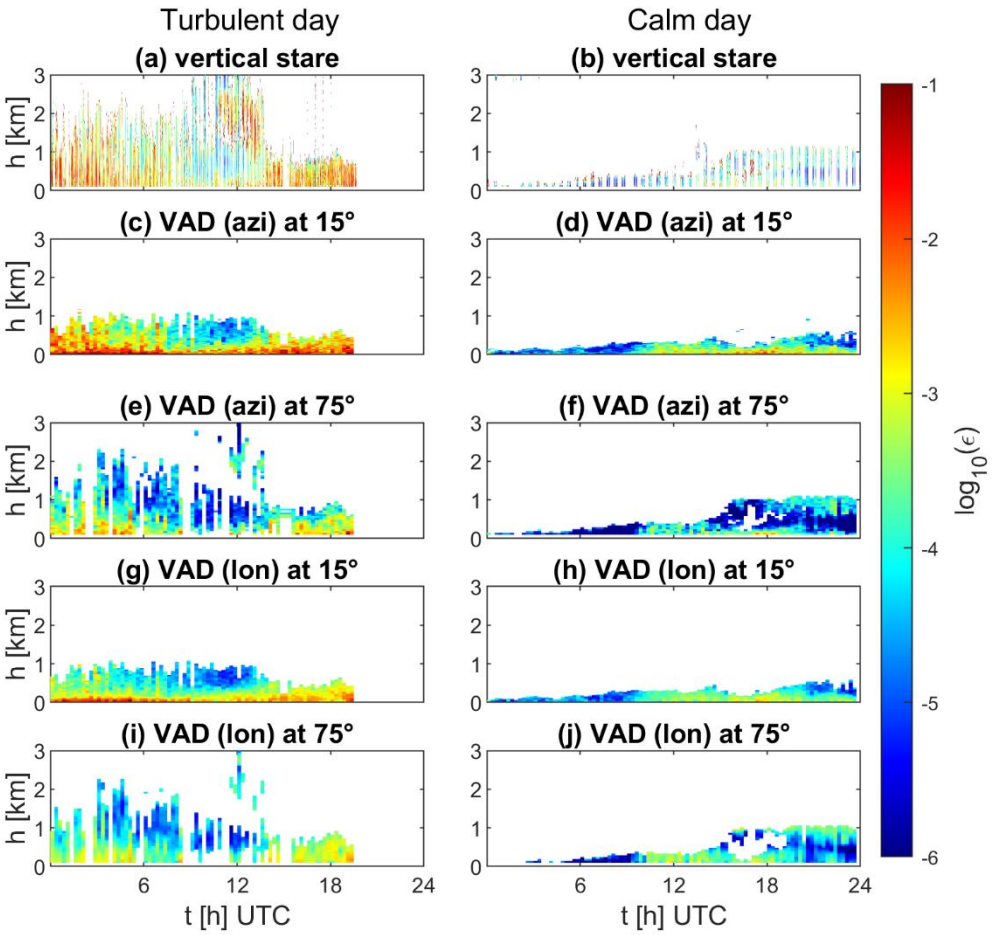

Figure 2.7 Comparison of base-10 logarithms of eddy dissipation rate (EDR [$m^2 s^{-3}$]) on a turbulent day (24 March 2017, left panel) and a calm day (31 March 2017, right panel). EDR is derived from the vertical stare (a and b), VAD scans using azimuthal approach (azi) at 15° elevation angle (c and d), azimuthal approach (azi) at 75° elevation angle (e and f), longitudinal approach (lon) at 15° elevation angle (g and h), and longitudinal approach (lon) at 75° elevation angle (i and j).

As seen in Figure 2.7, the EDR retrievals using the structure-function on VAD scans are qualitatively similar to the EDR retrievals from the vertical stare applying the method of O'Connor et al. (2010). In the early morning and afternoon of 24 March, there are high values of EDR detectable in all measurements (Figure 2.7, left panel), indicating turbulent conditions. During the calm day, 31 March, turbulence is detected after 10 UTC (Figure 2.7, right panel), and we can also see that in the afternoon, from 15 UTC, the top and bottom of the boundary layer was more turbulent than the middle of the boundary layer. The comparison between azimuthal (Figure 2.7(e) and 2.7(f)) and longitudinal (Figure 2.7(i) and 2.7(j)) approaches shows that they yield similar turbulence patterns, both in the turbulent and in the calm case. However, the longitudinal approach yields lower EDR values. In other words, some severe turbulent events have been underestimated. Similar results can be found with 15° elevation angle (Figure 2.7 (c,d) v.s. Figure 2.7(g,h)). This is more obvious in the

turbulent case (24 March), when the estimated EDR from the longitudinal approach is around 14% lower than the azimuthal approach. This results from our time series analysis as we apply one more averaging calculation on the longitudinal approach than on the azimuthal approach, averaging the EDR at each range gate, to plot the altitude-to-time figure. In this approach, some turbulence will be 'averaged out', or smoothened. As turbulence is a sudden change of airflow on a small temporal and spatial scale, more averaging means more smoothing. Even without a concrete validation, we can expect the longitudinal approach may underestimate the retrieval of EDR value, at least for this time serial analysis. In this regard, the azimuthal approach provides a superior EDR retrieval.

Regarding the comparison between different elevation angles, we do not expect a perfect match of EDR because the scans at different elevation angles do not execute simultaneously. However, the results at the 15° elevation angle (Figure 2.7(c) and (d)) show higher EDR values than at 75° (Figure 2.7(e) and (f)). One possible explanation is that, with the same range resolution, the lower elevation angle results in higher vertical resolution (12.9 m at 15° compared to 48.3 m at 75°), and we know the spatial scale of turbulence can be relatively small (dozens of meters). Thus, a low elevation angle may capture more turbulent signals, compared to the same range gate with higher elevation angle. Also, the data availability at 15° scans is higher than at 75° (Figure 2.4). However, the heterogeneity of the atmosphere should also be considered. With a low elevation angle, range gates further along the lidar beam also are further away from the zenith position, resulting in lower representativeness and higher uncertainty. For example, at 75° elevation angle, the straight-line distance between two adjacent data points (two points at the same range gates from two adjacent beams) at 1000 m range gate would be around 517 m, while at 15° elevation angle the distance is around 1931m. It is also likely that more turbulence occurs near the surface due to friction. We recommend combining both scan angles operationally: the low elevation scan for high-resolution measurements at a lower altitude, and the high elevation scan for lower resolution measurements at higher altitude.

Although the azimuthal approach reveals better results for continuous time series analysis, the longitudinal approach has a potential advantage: it can retrieve EDR values along the beam, which allows us to examine where the turbulence occurs on a horizontal scale. Currently, the lidar performs two VAD scans at different elevation angles every 15 minutes. This enables us to monitor and locate turbulences within a certain distance, depends on the scan strategy. Figure 2.8 illustrates two examples of VAD scans from 24 March 2017: Figure 2.8(a) depicts the situation at 00:44 UTC revealing an increased EDR to the north-east, at further range gates (1 to 2 km) while EDR retrieved using the azimuthal approach suggests turbulence occurred close to the lidar (Figure 2.7(g)). The second case is the situation at 11:44: the atmosphere is calm at higher altitudes, i.e. further along the beam, but increased EDR values are located at lower altitudes (Figure 2.7(g)). Accordingly, turbulences are found mainly to the south and west of the lidar (Figure 2.8(b)). This kind of horizontally spatial information of turbulence can only be delivered by a longitudinal approach. However, unlike the results from the azimuthal approach, which can be directly compared with results from the vertical stare (Figure 2.7), we are unable to compare and validate the horizontal EDR distribution for now. Nevertheless, the relative distribution of the presented EDR estimates demonstrates the potential of lidar observations to identify the location and duration of turbulence at a selected time.

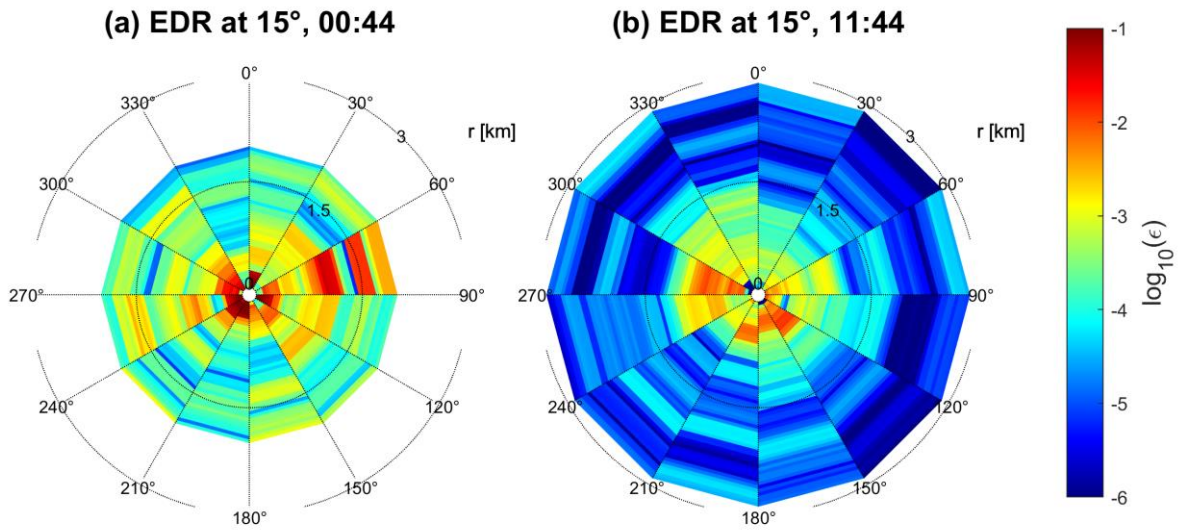

Figure 2.8 Beam-circular base-10 logarithms of EDR [m^2 s^{-3}] maps for two cases at 00:44 UTC (left) and 11:44 UTC (right) on 24 March 2017. The data is from VAD scans, at 15° elevation angle, using the longitudinal approach. The radial direction indicates the distance from the lidar. The data has been noise filtered.

Different calculation routes lead to different EDR results of azimuthal and longitudinal approach: a single profile for azimuthal and a set of conically shaped profiles for the longitudinal approach. By this means, the longitudinal approach has more potential for EDR horizontal distribution analyses, although no validation has been done so far. Regarding the temporal and vertical structure development of turbulence, the azimuthal approach performs better than the longitudinal approach, compared to vertical stare.

The VAD scan strategy can be easily modified to meet different requirements. The azimuthal interval of current scanning is 30°, which could be decreased but further research is needed to determine the effect on the EDR and the associated uncertainties. Further considerations would include setting up scans along airport runways. This has been done at some airports, such as Hong Kong airport (Hon and Chan, 2014).

The turbulence information we retrieved from lidar observations in this study, can be used for qualitative analyses, such as indicating the presence or absence of turbulence, but at this stage it is challenging to give a quantitative interpretation, such as how severe the turbulence is and how it would affect an airplane at take-off or landing. A validation dataset (in addition to lidar measurements) is needed, as well as input from lidar end-users, such as air traffic controllers and pilots. This may be the next step for the lidar application in Iceland.

2.5 Conclusions

In this work, we investigate how Leosphere Windcube 200S Doppler lidars can be used to

detect and quantify atmospheric turbulence in Iceland where the climate and weather conditions are characterized by strong winds and intense turbulence. However, the clean air (with low aerosol concentration) in Iceland leads to reduced backscatter signals from lidar systems, may require a different CNR threshold than previous studies in other locations, to screen the lidar data. Nevertheless, the presented results demonstrate that our algorithm can successfully map EDR over scales of several kilometres and accordingly help to monitor and identify turbulence.

Our results demonstrate that it is possible to apply VAD scans and a structure-function to derive near-real-time estimates of EDR. The results are comparable to EDR retrievals using vertical stares. The algorithm was able to successfully retrieve EDR for two case studies representing different typical weather conditions in Iceland, revealing the robustness of our method.

The low backscatter signal during conditions with low aerosol concentrations can lead to misinterpretations. Under these conditions (which frequently occur in Iceland), we recommend using a lower CNR threshold (-32 dB), compared to other studies, and combining it with the CI value from the Windcube lidar.

The two approaches to calculate the structure-function from the VAD scan reveal different performances: the azimuthal approach performs better in time series analysis and indicates when and at what altitude the turbulence occurs, since the longitudinal approach naturally has lower EDR values. On the other hand, the longitudinal approach shows the potential to determine the location of the turbulence relative to the lidar on a horizontal scale at a selected time, which makes it a valuable source of information near airport runways.

The EDR values vary with different VAD elevation angle. A low angle measurement has the advantage of higher data availability and quality near the surface, while a high angle measurement provides an overview at a higher altitude, thus a combination of both angles is recommended.

In general, the retrieval of EDR from lidar data to estimate the turbulence intensity is quite promising and it may be applied to improve the weather information available to the air traffic controllers in Iceland. Currently, there is ongoing work to make this algorithm operational for the lidar at Keflavik International airport. This work has significant potential for improved aviation safety in Iceland, considering the extreme and highly variable wind conditions.

2.6 References

Boquet M., Royer P., Cariou J-P., Machta M., Valla M. 2016. Simulation of Doppler Lidar Measurement Range and Data Availability. J. Atmospheric Ocean. Technol. 33:977–987.

Chan P W. 2009. Atmospheric turbulence in complex terrain: Verifying numerical model results with observations by remote-sensing instruments. Meteorol. Atmospheric Phys. 103:145–157.

Chan PW. 2010. LIDAR-based turbulence intensity calculation using glide-path scans of the Doppler LIght Detection And Ranging (LIDAR) systems at the Hong Kong

International Airport and comparison with flight data and a turbulence alerting system. Meteorol. Z. 19:549–563.

Cohn SA. 1994. Radar Measurements of Turbulent Eddy Dissipation Rate in the Troposphere: A Comparison of Techniques. J. Atmospheric Ocean. Technol. 12:85–95.

Dabas A. 1999. Semiempirical Model for the Reliability of a Matched Filter Frequency Estimator for Doppler Lidar. J. Atmospheric Ocean. Technol. 16:19–28.

Frehlich R. 1996. Simulation of Coherent Doppler Lidar Performance in the Weak-Signal Regime. J. Atmospheric Ocean. Technol. 13:646–658.

Frehlich R. 2001. Errors for Space-Based Doppler Lidar Wind Measurements: Definition, Performance, and Verification. J. Atmospheric Ocean. Technol. 18:1749–1772.

Frehlich R., Cornman L. 2002. Estimating Spatial Velocity Statistics with Coherent Doppler Lidar. J. Atmospheric Ocean. Technol. 19:355–366.

Frehlich R., Meillier Y., Jensen ML., Balsley B., Sharman R. 2006. Measurements of Boundary Layer Profiles in an Urban Environment. J. Appl. Meteorol. Climatol. 45:821–837.

Gryning S-E., Floors R., Peña A., Batchvarova E., Brümmer B. 2016. Weibull Wind-Speed Distribution Parameters Derived from a Combination of Wind-Lidar and Tall-Mast Measurements Over Land, Coastal and Marine Sites. Bound.-Layer Meteorol. 159:329–348.

Gryning S-E., Mikkelsen T., Baehr C., Dabas A., Gómez P., O'Connor E., Rottner L., Sjöholm M., Suomi I., Vasiljević N. 2017. Measurement methodologies for wind energy based on ground-level remote sensing. In: Renewable Energy Forecasting. Elsevier, 29–56.

Hocking WK. 1985. Measurement of turbulent energy dissipation rates in the middle atmosphere by radar techniques: A review. Radio Sci. 20:1403–1422.

Hon KK., Chan PW. 2014. Application of LIDAR-derived eddy dissipation rate profiles in low-level wind shear and turbulence alerts at Hong Kong International Airport. Meteorol. Appl. 21:74–85.

ICAO. 2018: ICAO Annual Safety Report 2018, [online] Available from: https://www.icao.int/safety/Documents/ICAO_SR_2018_30082018.pdf, Montreal, Canada.

Kolmogorov AN. 1962. A refinement of previous hypotheses concerning the local structure of turbulence in a viscous incompressible fluid at high Reynolds number. J. Fluid Mech. 13:82–85.

Kolmogorov AN. 1991. The Local Structure of Turbulence in Incompressible Viscous Fluid for Very Large Reynolds Numbers. Proc. Math. Phys. Sci. 434:9–13.

Lenschow DH., Mann J., Kristensen L. 1994. How Long Is Long Enough When Measuring Fluxes and Other Turbulence Statistics? J. Atmospheric Ocean. Technol. 11:661–673.

Leosphere, Inc. 2013: WINDCUBE 100s-200s User Manual, Orsay, France.

Leung MYT., Zhou W., Shun C-M., Chan P-W. 2018. Large-scale Circulation Control of the Occurrence of Low-level Turbulence at Hong Kong International Airport. Adv. Atmospheric Sci. 35:435–444.

Manninen AJ., Marke T., Tuononen M., O'Connor EJ. 2018. Atmospheric Boundary Layer Classification With Doppler Lidar. J. Geophys. Res. Atmospheres 123:8172–8189.

Manninen AJ., O'Connor EJ., Vakkari V., Petäjä T. 2016. A generalised background correction algorithm for a Halo Doppler lidar and its application to data from Finland. Atmospheric Meas. Tech. 9:817–827.

Misaka T., Ogasawara T., Obayashi S., Yamada I., Okuno Y. 2008. Assimilation Experiment of Lidar Measurements for Wake Turbulence. J. Fluid Sci. Technol. 3:512–518.

Muñoz-Esparza D., Sharman RD., Lundquist JK. 2018. Turbulence Dissipation Rate in the Atmospheric Boundary Layer: Observations and WRF Mesoscale Modeling during the XPIA Field Campaign. Mon. Weather Rev. 146:351–371.

Nijhuis ACPO., Unal CMH., Krasnov OA., Russchenberg HWJ., Yarovoy AG. 2019. Velocity-Based EDR Retrieval Techniques Applied to Doppler Radar Measurements from Rain: Two Case Studies. J. Atmospheric Ocean. Technol. 36:1693–1711.

Norris, Guy. 2019. Iceland's Keflavik airport reopens for restricted flight tests. Available at https://atwonline.com/airports-routes/iceland-s-keflavik-airport-reopens-restricted-flight-tests (accessed July 1, 2019).

O'Connor EJ., Illingworth AJ., Brooks IM., Westbrook CD., Hogan RJ., Davies F., Brooks BJ. 2010. A Method for Estimating the Turbulent Kinetic Energy Dissipation Rate from a Vertically Pointing Doppler Lidar, and Independent Evaluation from Balloon-Borne In Situ Measurements. J. Atmospheric Ocean. Technol. 27:1652–1664.

O'Connor, Ewan. Research Scientist. (Personal communication, April 2017).

Ólafsson H., Ágústsson H. 2007. The Freysnes downslope windstorm. Meteorol. Z. 16:123–130.

Ólafsson H., Furger M., Brümmer B. 2007. The weather and climate of Iceland. Meteorol. Z. 16:5–8.

Pauscher L., Vasiljevic N., Callies D., Lea G., Mann J., Klaas T., Hieronimus J., Gottschall J., Schwesig A., Kühn M., Courtney M. 2016. An Inter-Comparison Study of Multi- and DBS Lidar Measurements in Complex Terrain. Remote Sens. 8:782.

Päschke E., Leinweber R., Lehmann V. 2015. An assessment of the performance of a 1.5 μm Doppler lidar for operational vertical wind profiling based on a 1-year trial. Atmospheric Meas. Tech. 8:2251–2266.

Ramanathan V., Crutzen PJ., Kiehl JT., Rosenfeld D. 2001. Aerosols, Climate, and the Hydrological Cycle. Science 294:2119–2124.

Sathe A., Mann J. 2013. A review of turbulence measurements using ground-based wind lidars. Atmospheric Meas. Tech. 6:3147–3167.

Sharman, R. 2016: Nature of Aviation Turbulence, in: Aviation Turbulence, edited by: Sharman, R. and Lane, T., Springer International Publishing, Cham, Switzerland, 3-30, 2016.

Sinclair PC., Kuhn PM. 1991. Aircraft Low Altitude Wind Shear Detection and Warning System. J. Appl. Meteorol. 30:3–16.

Smalikho IN., Banakh VA. 2017. Measurements of wind turbulence parameters by a conically scanning coherent Doppler lidar in the atmospheric boundary layer. Atmospheric Meas. Tech. 10:4191–4208.

Smalikho I., Köpp F., Rahm S. 2005. Measurement of Atmospheric Turbulence by 2-μm Doppler Lidar. J. ATMOSPHERIC Ocean. Technol. 22:15.

Stephan A., Wildmann N., Smalikho IN. 2018. Spatiotemporal visualization of wind turbulence from measurements by a Windcube 200s lidar in the atmospheric boundary layer | Request PDF. In: 24th International Symposium on Atmospheric and

Ocean Optics: Atmospheric Physics. Tomsk, Russian Federation: International Society for Optics and Photonics, 1083357).

Stull, R. B.1988: An Introduction to Boundary Layer Meteorology, Springer Science & Business Media., Doetinchem, Netherlands.

Thobois LP., Krishnamurthy R., Loaec S., Cariou JP., Dolfi-Bouteyre A., Valla M. 2015. Wind and EDR Measurements with Scanning Doppler LIDARs for Preparing Future Weather Dependent Separation Concepts (Invited). In: 7th AIAA Atmospheric and Space Environments Conference. Dallas, TX: American Institute of Aeronautics and Astronautics.

Tuononen M., O'Connor EJ., Sinclair VA., Vakkari V. 2017. Low-Level Jets over Utö, Finland, Based on Doppler Lidar Observations. J. Appl. Meteorol. Climatol. 56:2577–2594.

Wächter M., Rettenmeier AK. 2009. Characterization of short time fluctuations in atmospheric wind speeds by LIDAR measurements. Meteorol. Z.:277–280.

Chapter 3

Dust monitoring by Doppler lidar

3.1 Introduction

A lidar (light detection and ranging) system is an active remote sensing technology, which is used in different sectors, from auto-driven cars' sensor (Gao et al., 2018) to civil engineering structure monitoring (Brook et al., 2010). It is also used in meteorology, mainly focussed on wind detection (Bilbro et al., 1984; Chan, 2012; Gryning et al., 2017, Yang et al., 2020) and aerosol and cloud detection (Ansmann and Müller, 2005; Burton et al., 2012), depending on the type of lidar.

The lidar is emitting a laser beam and receives the backscattered signals, which could be airborne aerosols, cloud droplets, or other particles in the atmosphere. In principle, we can retrieve the properties of the scatterers from the lidar backscatter signals. The most commonly used variable is the backscatter coefficient, which is available for elastic-backscatter lidars. With Raman lidars or high spectral resolution lidars (HSRL), the extinction coefficient profiles, which are related to the absorbed lidar signals, can be measured directly, and the lidar ratio can be calculated based on the backscatter and extinction coefficient (Ansmann and Müller, 2005). With a depolarization channel, lidars can measure the depolarization ratio and estimate the particles' shape (Sassen, 2005). A combination of the lidar ratio and the depolarization ratio is commonly used for aerosol classification and volcanic ash discrimination (Burton et al., 2012; Groß et al., 2012).

A Doppler wind lidar is mainly used for wind measurements, including wind field/profiles retrieval (Bilbro et al., 1984), low-level jet detection (Tuononen et al., 2017), and atmospheric turbulence detection (Banakh et al., 1999). Lidar systems have been used widely for enhancing aviation safety around the world (Chan & Lee, 2013; Gultepe et al., 2019; Thobois et al., 2019). In Iceland, two Doppler wind lidars have been deployed for volcanic ash detection.

Besides Doppler lidar, another remote sensing instrument used in Iceland for aerosol detection is the ceilometer, i.e. eye-safe single-wavelength backscatter lidar. The ceilometer is designed for cloud base detection but also used for aerosol observations, such as dust layer (Münkel et al., 2007) and volcanic ash detection (Wiegner et al., 2014). A significant advantage of ceilometers is that they can run unattended and continuously, resulting in unique data to monitor aerosol distributions. Moreover, as they are inexpensive compared to other lidars, networks can be installed.

Iceland comprises a large sandy desert in the central plateau, covering 22,000 km2, almost 20% of the country (Arnalds et al., 2016). The subarctic weather in Iceland is characterized by strong wind events (Ólafsson et al., 2007) due to the frequent passing of low-pressure systems and associated weather fronts. This results in wind erosion leading to frequent dust storms. Furthermore, volcanic eruptions occur on average every three to five years (Thordarson and Larsen, 2007). Dust from a desert as well as volcanic ash from eruptions

could have a significant impact locally and globally on radiation balance, economics, and human health (Budd et al., 2011; Carlsen et al., 2015; Goudie, 2014; Gústafsson and Steinecke, 1995; Saidou Chaibou et al., 2020; Wittmann et al., 2017). According to observations at 30 Icelandic weather stations between 1949 and 2010, on average, there are 34 days of dust events annually. If the re-suspension of volcanic materials is considered as well, the number increases to 135 days (Dagsson-Waldhauserova et al., 2014). In 2010, the explosive eruption of Eyjafjallajokull, and the subsequent ash disrupted air traffic generated great economic loss (Gudmundsson et al., 2010; Petersen et al., 2012). Accordingly, an adequate method to monitor the ash dispersion continuously could improve aviation safety significantly.

The volcanic ash can be transported all over Europe and has been studied with satellite (Rix et al., 2012), airborne (Chazette et al., 2012), and ground-based remote sensing technologies(Ansmann et al., 2010; Sicard et al., 2012; Wiegner et al., 2012), including lidar, in different countries other than Iceland. However, aerosol monitoring in Iceland has only been investigated in a few studies. Prospero et al. (2012) assessed Icelandic dust over the North Atlantic using aerosol concentration measurements in South Iceland. Dagsson-Waldhauserova et al. (2019) measured the vertical profiles of aerosols in Iceland using airborne measurements. But the ground-based remote sensing measurements of aerosols in Iceland, close to the source of Icelandic dust and volcanoes, is still needed.

In Iceland, there are two WindCube Scan 200S Doppler wind lidars (Leosphere, Inc.) with depolarization modules. One is installed at Keflavik International Airport and one on a mobile trailer. The WindCube is a commercial lidar widely used in the wind energy sector and for meteorological research (Liao et al., 2020; Stephan et al., 2019). It is the first time a depolarization module has been installed in a WindCube lidar for aerosol observation. In conjunction with the mobile lidar a ceilometer (CL31, Vaisala) and a sun-photometer (CE318-T, Cimel) were installed in Reykjavik. With these instruments, we now have the possibility of using ground-based remote sensing technologies to monitor aerosols in Iceland. We investigated two dust events that occurred in Southwest-Iceland in the summer of 2019. These measurements are supplemented by observations from webcams and PM concentration measurements, which are described in detail in section 3.2. The results of these two events are presented in section 3.3. The difference between instruments and events are discussed in section 3.4, and the study concludes in section 3.5. Details of the data processing procedure and data availability can be found in the Appendix.

3.2 Research sites, and data processing

South Iceland is not only the region with most observed dust events (Dagsson-Waldhauserova et al., 2014), but it is also the most populated area of the country. The capital city Reykjavik, the largest city in the country, is located in the region with two-thirds of the total population, i.e. more than 230,000 (Statistics Iceland, 2020). We selected two dust episodes observed in Reykjavik in the summer of 2019. This summer was very dry and occasionally strong winds were observed (IMO, 2019). To demonstrate how lidar and ceilometer measurements can be used to characterize and monitor aerosols, various instruments are used at two observation sites. In this section, we will describe the observation sites, the instruments, and the processing methodology.

3.2.1 Observation sites and dust events

Two observation sites are used in this study: Reykjavik (RVK) and Keflavik (KEF). The locations of these sites are displayed in Figure 3.1. RVK (Figure 3.1, location A) has the most varied instrumentation. KEF (Figure 3.1, location B) is the Keflavik International Airport, the main international airport in Iceland. RVK site is 52 m above sea level (asl) and KEF is 51 m asl.

The first selected dust event was observed on June 14 and 15 at RVK, and the second was observed on July 31 and August 1, at both RVK and KEF. The two dust episodes are named as the June case and the July case accordingly throughout the text. The coordinates and the instruments installed at both sites can be found in Table 3.1.

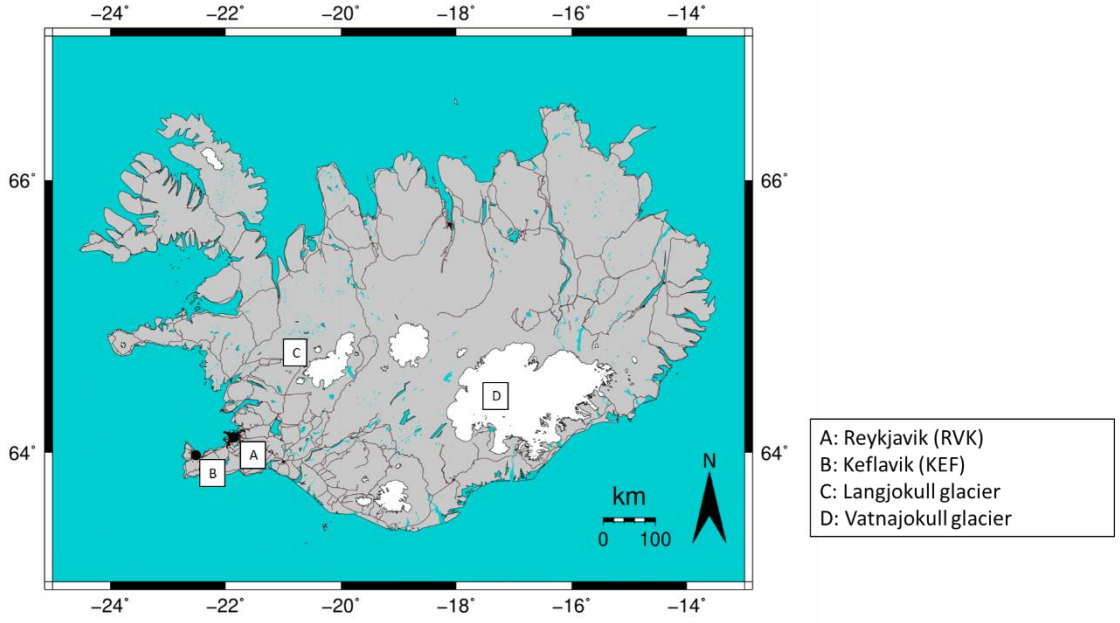

Figure 3.1 Observation sites (A and B) used in this study. Detailed coordinates and instruments can be found in Table 3.1. C and D indicate the location of Langjokull and Vatnajokull glaciers.

Table 3.1 The dates, locations and instrumentation available during the two events described in this study.

Start date	End date	Location	Latitude [°N]	Longitude [°W]	lidar	ceilometer	Other measurements
2019-06-14	2019-06-15	RVK	64.1275	21.9027	WindCube	CL31	PM 10, sun-photometer,
2019-07-31	2019-08-01	RVK	64.1275	21.9027	WindCube	CL31	PM 10, sun-photometer
		KEF	63.9829	22.6005	WindCube	CL51	Radio sounding

3.2.2 Instruments

The two Leosphere WindCube Scan 200S Doppler lidars used in this study are both equipped with a depolarization module. The emitted wavelength is 1.54 μm, and the selected spatial resolution is 100 m. The lidar can be operated in various modes, according to the observation purpose: it can measure vertical profiles of the horizontal wind components and

vertical velocity with conically shaped Velocity-Azimuth-Display (VAD) scans (Thobois et al., 2019). Furthermore, the lidars are equipped with a depolarization module for aerosol measurements. In this study, we use the vertical stare for the backscatter coefficient and depolarization ratio measurements and VAD scans for calibration and wind measurements. One system is located at KEF, and the other is installed on a mobile trailer located at RVK. The mobile lidar offers the capability to move the instrument in case of a special event, e.g. a volcanic eruption. During this study, the lidar trailer was stationary at RVK, next to the headquarters of the Icelandic Meteorological Office (IMO).

IMO operates a ceilometer network in Iceland, including seven Vaisala CL31 and two CL51 ceilometers. In addition, two CL51 ceilometers are located at KEF, as part of the Automated Weather Observing System (AWOS) and operated by the airport. Here, we use one CL31 ceilometer that is installed in the mobile trailer, along with the lidar, and one CL51 ceilometer at KEF. Table 3.2 summarizes the basic specifications of the lidars and the ceilometers. The main difference between the CL31 and CL51 ceilometers is the different laser pulse energy resulting in a maximum detection range of 7.6 and 15 km, respectively.

Table 3.2 The main specifications of the lidars and ceilometers operated in Iceland.

	lidar	ceilometer	
model	Windcube 200S	CL31	CL51
manufacturer	Leosphere	Vaisala	Vaisala
wavelength [μm]	1.54	0.91	0.91
maximum detection range [km]	14	7.6	15
range resolution [m]	100	10	10
elevation angle [°]	-10—90	90	90
azimuth angle [°]	0—360	N/A	N/A

Lidars and ceilometers are the main instruments utilized in this study, and the data processing of each will be described in sections 2.3 and 2.4. The wind retrieval of lidar data is described by Yang et al. (2020).

In addition to the data from the Doppler lidars and ceilometers, several complementary datasets are applied in this study, depending on the availability at the locations. A Cimel CE-318 sun-photometer, provided by Ludwig Maximilian University of Munich (LMU), Germany, was deployed from July 2018 to September 2019 at IMO headquarters at Reykjavik. From the measured data aerosol optical properties, primarily the aerosol optical depth (AOD) and the Angstrom exponent, can be retrieved.

The Environment Agency of Iceland measures air quality indicators around the country, mostly in urban areas. Here we use the ground-level PM 10 (particle matter with a diameter of less than10 μm) and PM 2.5 (particle matter with a diameter of 2.5 μm or less, also known as fine particles) mass concentrations. They are commonly used as an indicator of air quality around the world. We use the hourly data collected in Njorvasund, Reykjavik, which is about 3.5 km from IMO. The instrument used at this station is a BAM 1020 Continuous Particulate Monitor.

There are several webcams mounted on the IMO headquarters' building, taking pictures automatically on an hourly basis. These webcams are used for visibility examination.

The mobile lidar trailer was placed close to IMO's measurement field which has an

automatic weather station (AWS). An AWS is also located at KEF. From both AWS we use the 10 minutes relative humidity measurements. These measurements have an up to ±5% uncertainty, the highest when relative humidity above 95%, which means that the recorded relative humidity may exceed 100%.

At KEF, IMO operates a radio sounding station where a radiosonde is launched twice per day, at noon and midnight.

NOAA's HYSPLIT (Stein et al., 2015) model is used to calculate the backward trajectory of the dust events to estimate its possible origin.

The availability of the dataset for online download can be found in Appendix AP7.

3.2.3 Lidar and ceilometer data processing

The primary output of Leosphere WindCube lidar is the carrier to noise ratio (CNR), which is directly related to the received backscatter signal (Boquet et al., 2016). Besides CNR, the output also includes radial wind speed, relative backscatter coefficient (β), and depolarization ratio (δ). To obtain the relative backscatter, an automatic calibration can be applied. However, this automatic calibration is not always reliable due to the change of calibration parameters with atmospheric conditions. In addition, the automatic retrieval of the depolarization ratio sometimes has large gaps, due to the mechanical problems of the polarizer. This can cause issues in the retrieval. Thus, we calculate the backscatter coefficient and the depolarization ratio from the raw output CNR. Here an overview of the processing is given. For the ceilometer, we followed a relatively mature path to calibrate the data, with some correction made by us. We also used Klett inversion to retrieve particle backscatter coefficient profiles. In the Appendix, we present the calculation and lidar data screening in detail.

3.2.3.1 Lidar data processing: backscatter coefficient

Leosphere WindCube scanning lidars usually focus the emitted beam at a specific range to maximize the detection distance. This has little impact on wind measurements, but it will cause an artificial peak in the attenuated backscatter coefficient profiles – this is referred to as the focal effect. With a known telescope function, the focal effect can be corrected. The telescope function varies little for the solid-state WindCube scanning lidars. However, strong atmospheric turbulence or moving a lidar can change the focus distance. The lidar can be scheduled to calibrate the backscatter profile automatically. This works under the assumption of homogeneous aerosol load during the calibration scan, along with time and range. Typically, low elevation scans over a homogeneous surface are programmed to calculate the telescope function. Fit parameters of this function are then stored in the lidar database and used to calibrate any subsequent backscatter profile. However, the automatic calibration is not always accurate, especially if the homogeneity criterium is not met during a pre-scheduled calibration scan.

Here we used a manual approach (Leosphere, 2020) to calibrate lidar data and retrieve the relative backscatter coefficient from CNR. The advantage is, that the scan used to calculate the telescope function is verified for homogeneity. The CNR value is a direct lidar output, which depends on the concentration of aerosols in the atmosphere which backscatter the

emitted laser light. The retrieval of the relative backscatter coefficient is described in detail in Appendix AP2.

The uncertainties of CNR measurements have been estimated by calculating the power spectrum density (PSD) for each range. The calculated uncertainties are within 1 dB in the June case and 0.5 dB in the July case. More detailed information can be found in the Appendix.

3.2.3.2 Lidar data processing: depolarization ratio

The detection of depolarization ratio is widely used by advanced lidar systems to classify aerosol types. Typically, linearly polarized radiation is emitted and two detection channels are implemented: one perpendicular to the plane of the laser, and one parallel or one total (parallel and perpendicular). With calibrated two channel observations (Freudenthaler et al., 2009) the particle linear depolarization ratio δ_p can be determined and used. Together with the lidar ratio and/or the color ratio, one can distinguish different aerosol types, e.g. Saharan dust, marine aerosols, biomass burning aerosol, and volcanic ash (Ansmann et al., 2012; Burton et al., 2012; Groß et al., 2011, 2012).

While the ceilometers do not provide depolarization information, a depolarization ratio is measured by the Doppler lidar. Using the co-polar and cross-polar CNR signals, the depolarization ratio profiles (Royer et al., 2016) can be computed from lidar measurements. However, as the main application of the WindCube lidar is the monitoring of the wind field (see Thobois et al., 2019), the depolarization ratio provided has not undergone extensive validation, so that the obtained numbers can only be treated as a qualitative approximation: discrimination between spherical and non-spherical particles is feasible but discrimination between different types of non-spherical particles is not possible. The detailed procedure of depolarization ratio retrieval is presented in Appendix AP3.

Without a correct calibration of the depolarization channel, it is difficult to provide a quantitative measurement of aerosols. Instead, the measured δ can be treated as a reference: higher δ value means the scatterers are more likely to be non-spherical particles. The background value within the boundary layer and cloud layer is predominantly below 0.2 on a relatively clear day. An example is displayed on data acquired on July 28, 2019 (Figure A2). The wavelength of lidar also needs to be taken into account. The wavelength of the Doppler wind lidars we use in Iceland is 1.54 µm, while most other aerosol studies use lidars measuring in the wavelength range from 355 nm to 1064 nm (Burton et al., 2012; Groß et al., 2012). The strength of the polarization process partly depends on the particle size relative to the wavelength, as well as the particles' deviation from the spherically symmetrical shape (Sassen, 2005). The measured depolarization ratio is mostly wavelength-independent, but a few studies (e.g. Freudenthaler et al., 2009; Groß et al., 2012) found a dependency in the boundary layer.

Although there are a lot of studies using lidar to classify aerosols with depolarization ratio measurements (some combined with lidar ratio and/or colour ratio), other studies (e.g. Haarig et al., 2017; Sakai et al., 2000) suggest that the relative humidity (RH) could have a large impact on the depolarization ratio and analyzing results without considering the relative humidity could introduce uncertainties. The reason for this is that hygroscopic, non-spherical particles can absorb water vapour when relative humidity increases and changes to more spherical shape. In addition, the size of the particle may also increase, resulting in

a higher backscatter coefficient and also altering the lidar ratio. The visibility, or the extinction term of lidar measurements, may also be highly sensitive to the change in relative humidity (Gultepe et al., 2016, 2019; Thobois et al., 2019). These studies suggest that relative humidity can have a significant impact on lidar backscatter and depolarization measurements.

In this study, we occasionally identify vertical stripes from the cross-section plot of retrieved lidar backscatter coefficients and depolarization ratios, which are caused by missing profiles. These can be fixed by filtering the data and averaging. Detailed information can be found in Appendix AP4.

3.2.3.3 Ceilometer data processing

According to the manual (Vaisala, 2004) of CL31, the output of the ceilometer is attenuated backscatter coefficient β^*. Considering the lidar constant in lidar equation is unknown, it would make sense to treat the attenuated backscatter output as "reported range corrected signal (RCS)" ($P(r)r^2$). The CL31 ceilometer data processing procedure has been studied and here we mainly follow the method of Kotthaus et al. (2016). A dark measurement has been applied to remove the instrument related background signals $P^{bgi}(r)$. The details of dark measurements can be found in the Appendix AP5. The corrected profile $\hat{P}r^2$ is found to be negative in certain ranges, which is unrealistic. We observed this in several cases, e.g. the June case. According to the communication with the manufacturer, this is instrument-related and can be corrected by adding a constant. Here we use a cosmetic shift constant F^{CS}:

$$RCS_{corrected} = \hat{P}r^2 + F^{CS} \quad \text{(eq 3.1)}$$

Without an elevated aerosol layer, the atmosphere above the boundary layer is considered to be nearly aerosol free. We can estimate F^{CS} based on this assumption. In this study, we use $F^{CS} = 1 \times 10^{-3}\ km^{-1}\ sr^{-1}$ for the data in the June case, but $F^{CS} = 0\ km^{-1}\ sr^{-1}$ in the July case, while the signal at altitudes in the aerosol-free atmosphere is close to zero as expected. We also compare the ceilometer data with data of a sun-photometer, which is co-located to the ceilometer/lidar trailer and calibrated and validated by AERONET. The sun-photometer provides the aerosol optical depth (AOD) at wavelength 1020 nm which can be used to calibrate the ceilometer measurement. AOD is the integration of the particle extinction coefficient α_p, as the molecular backscatter coefficient β_m and the extinction coefficient α_m are time-independent. With a fixed lidar ratio S_p, we can assume the integration of β^* is proportional to AOD, and AOD retrieved from the ceilometer should agree with sun-photometer measurements. Here we use a factor C to scale ceilometer and sun-photometer measurement:

$$AOD_{sun-photometer\ 1020\ nm} = \frac{S_p}{C}\int \beta^*(r) \quad \text{(eq 3.2)}$$

When there are no clouds, factor C is quite stable (Figure A4A4). Excluding points when there are clouds, averaging the results we have factor C=1.09.

In summary, here we correct the ceilometer data from the original RCS using:

$$RCS_{corrected} = \frac{1}{C}\left(P(r) - P^{bgi}(r)\right)r^2 + F^{CS} \qquad \text{(eq 3.3)}$$

The whole correction procedure is demonstrated in Figure 3.2. With the corrected RCS profile, we can use the Klett inversion method (Klett, 1985) to retrieve β_p profile and the result should agree with sun-photometer (Figure 3.2, right). We use the backward Klett inversion method, with the aerosol-free reference height, where $\beta_p = 0$ and determined by Rayleigh calibration (Wiegner & Geiß, 2012). Figure 3.2 is an example where the reference height is determined at around 3.7 km. The green line in Figure 3.2 shows the molecular signal, which is generated by calculating the molecular extinction coefficient α_m based on the radiosonde measurement made at Keflavik, which is 45 km southwest of Reykjavik. The corrected RCS profile (orange line) agrees well with the molecular contribution at high altitudes, i.e. aerosol free conditions.

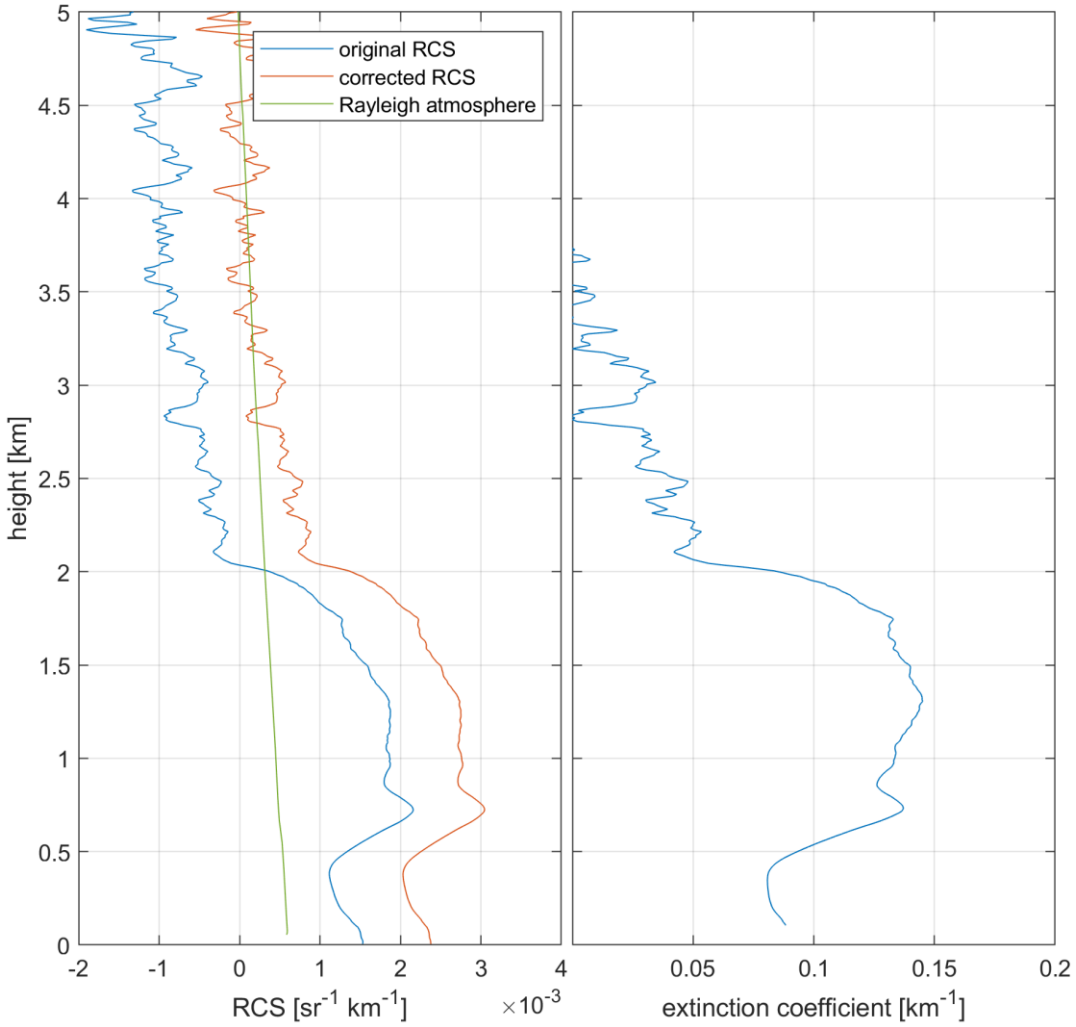

Figure 3.2 ***Left****: Original ceilometer RCS profile (blue) at 21:20, June 14, an average of 30 minutes measurements. The profile was vertically smoothed by a moving average filter of 100 m. This profile was further corrected by the dark measurement, factor C, and cosmetic shift FCS, and the corrected profile is the orange curve. The green line demonstrates the Rayleigh atmosphere.* ***Right****: Particle extinction coefficient derived from ceilometer observations, with a calculated AOD of 0.269, which agrees with sun-photometer measurement. The detailed calculation can be*

found in Appendix AP8.

3.3 Results

Several dust events were observed in the summer of 2019, and they can be identified from the PM concentration measurements (Figure 3.3). We selected two events observed in the middle of June and at the end of July 2019. On June 14, a dust storm was observed in the Reykjavik area. The weather observations recorded low visibility and hazy weather. We compared the backscatter coefficients and depolarization ratios from the ceilometer and wind lidar at RVK. On July 31, another dust storm was observed in Reykjavik, as well as in Keflavik. In this case, we studied both the ceilometer and lidar observations at RVK and KEF.

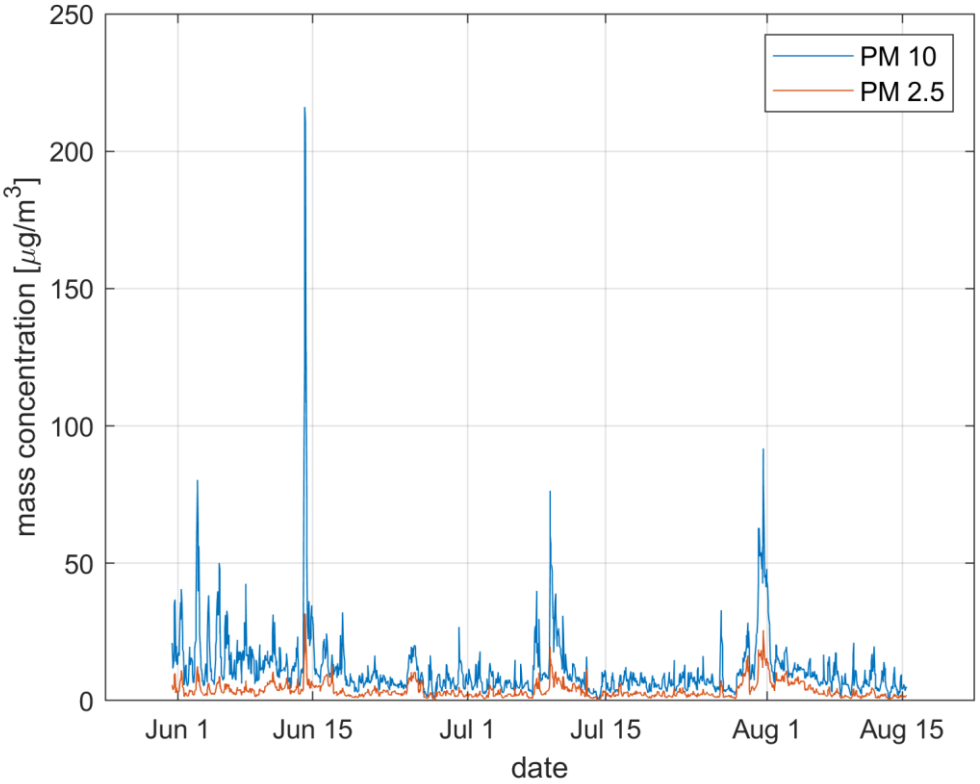

Figure 3.3 Hourly PM 10 (blue) and PM 2.5 (orange) concentration ([μm m^{-3}]) measured at Njorvasund, Reykjavik, by the Environment Agency of Iceland, from June 1 to August 15, 2019.

3.3.1 The June case (June 14 and June 15)

On 14 June 2019, the weather in Reykjavik was dry with winds from the north-east. Figure 3.4 shows the 1-hour forecast made at 12:00 UTC by IMO, which illustrates the weather conditions. A dust storm passed through Reykjavik in the afternoon, moving from the northeast. According to the HYSPLIT trajectory simulation and weather conditions, the origin of the dust is considered to be at Lake Hagavatn, a dry lake on the south of Langjokull glacier (Figure 3.1, location C). The dust storm could be seen clearly via the web cameras at IMO. From the camera at IMO pointing north (Figure 3.5), Mt. Esja, in ~10 km distance was visible in the morning. During the dust event, the visibility decreased and Mt. Esja disappeared. Weather observations showed dust from 15:00 UTC to 21:00 UTC (one report

every three hours). The air quality dropped at the same time. PM 10 and PM 2.5 concentration (Figure 3.6(e)) started to increase at 14:00 UTC and reached a peak value at 17:00 UTC. The surface wind direction changed from easterly to northerly and finally to westerly in the afternoon of the next day, June 15. At around 12:00 UTC, June 14, the dry air from northeast arrived in Reykjavik and PM concentration increased sharply, as well as the AOD and particle size measured from the sun-photometer (Figure 3.6(f)). Sun-photometer needs to track the sunlight, which is probably the reason why when the visibility dropped considerably the sun-photometer only acquired two measurements during the dust episode (high PM concentration period) at around 21:20 UTC, 14 June. The atmosphere stayed dry during the whole dust event, from 12:00 UTC on June 14 to 12:00 UTC on June 15, but was then cleaned by a shower in the afternoon of June 15.

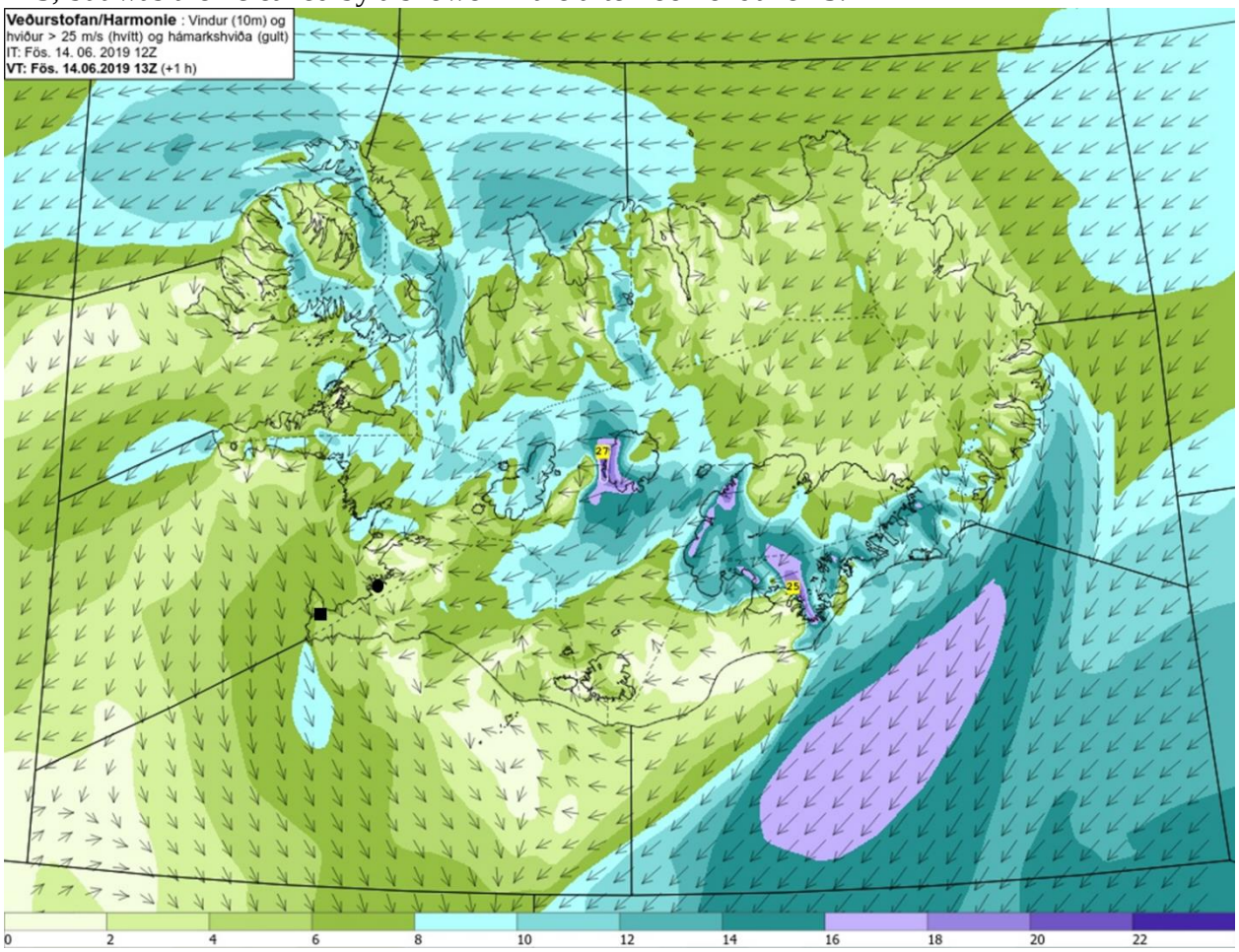

Figure 3.4 Wind conditions during the June case. This is a HARMONIE-AROME model forecast of 10 m wind at 13 UTC, June 14, 2019. The arrows indicate the wind direction while the colours indicate the wind speed [m s^{-1}]. The black dot and square indicate the locations of RVK and KEF, respectively.

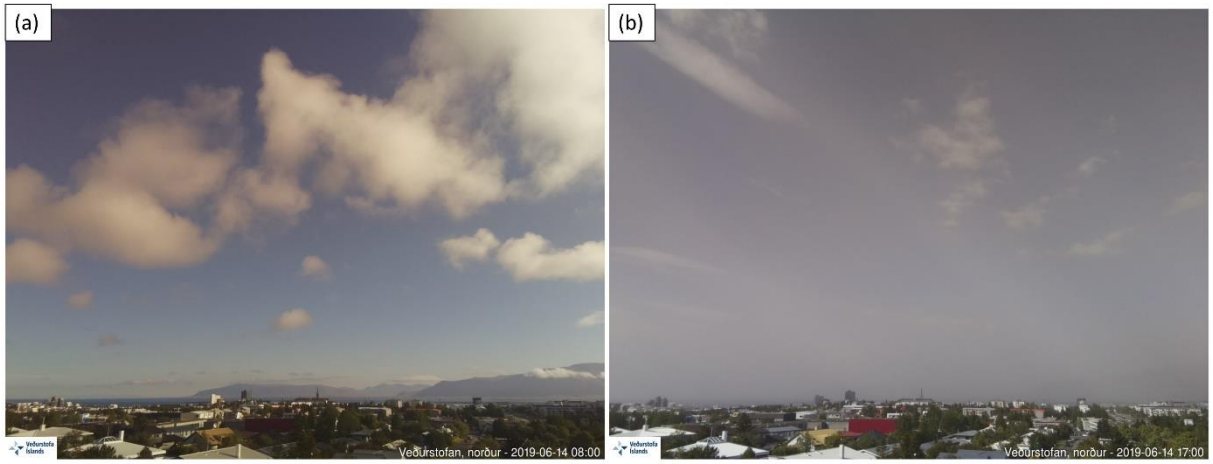

Figure 3.5 Photos taken by the web camera at IMO at 08:00 UTC (a) and 17:00 UTC (b), June 14, 2019, looking northward. The distant mountain on the right-hand side is Mt. Esja.

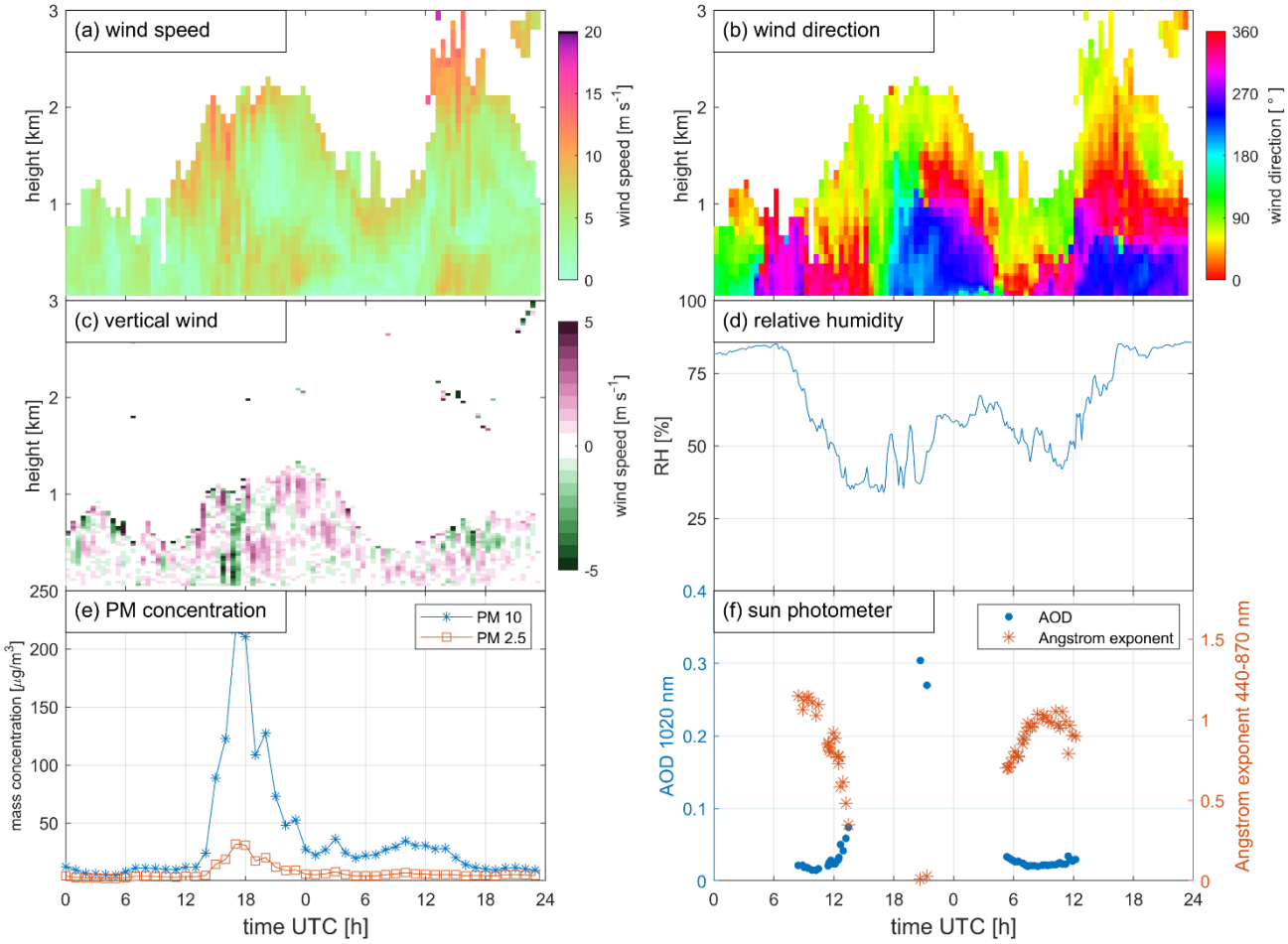

Figure 3.6 Wind speed (a, [m s^{-1}]), wind direction (b, [°]), vertical wind velocity (c, [m s^{-1}]) , relative humidity (d, [%]) , PM 10 (e, blue) and PM 2.5 (e, orange) concentration ([μm m^{-3}]), and sun-photometer observations (f) on June 14 and 15, 2019. The wind speeds were retrieved from lidar VAD scans. PM concentrations are measured at Njorvasund, Reykjavik. The relative humidity was measured at the weather station at IMO headquarters. The blue dots in (e) are AOD at 1020 nm, and

the orange asterisk markers are the Angstrom exponent (440-870 nm). The time axis starts from 00:00 UTC, June 14, 2019, covering two days.

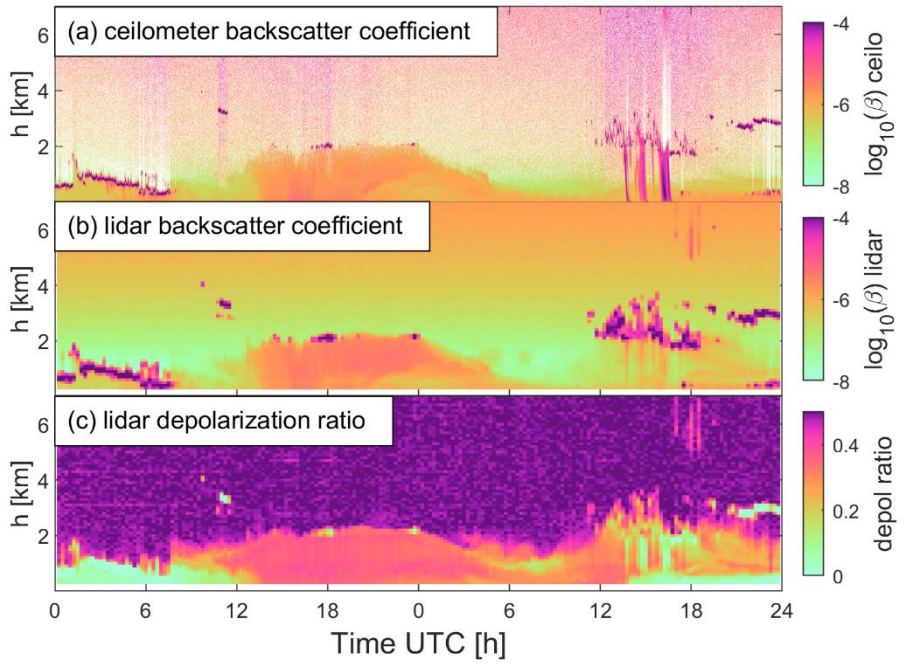

Figure 3.7 Time height cross-section of the backscatter coefficient from the ceilometer (a) and the Doppler lidar (b) as well as the lidar depolarization ratio (c) in Reykjavík, for 48 hours, from 00:00 UTC, June 14 to 24:00 UTC, June 15, 2019. The lidar data is an average of 15 minutes, and the ceilometer data is not averaged. Note that the lidar measurements start at 200 m above the surface.

Figure 3.7 shows the backscatter coefficient measured by the ceilometer (a) and the lidar (b) as well as the lidar depolarization ratio (c). The lidar data were averaged over 15 minutes. A strong backscatter signal corresponds to more scatterers in the atmosphere. The regions of very high backscatter coefficient shown in dark purple in figure 3.7 (a) and (b), found on the morning of June 14 (00:00 to 07:00 UTC) and the evening of June 15 (12:00 to 24:00 UTC) are considered to represent low clouds. The low depolarization ratio in these regions indicates spherical scatterers, such as liquid cloud droplets. Both the lidar and the ceilometer detected an aerosol layer starting from around 12:00 UTC on June 14. In the evening of June 14, around 22:00 UTC, the aerosol layer was elevated to around 1 km above the surface and it persists until June 15 around 05:00 UTC, when it subsided again. This aerosol layer represents a layer of suspended dust. In the afternoon of June 15, showers were observed from 13:00 UTC onwards. The ceilometer is more sensitive to precipitation than the lidar, which is the reason that the showers are not as easily seen in Figure 3.7 (b). The washout effect of precipitation is significant, both the backscatter coefficient and the depolarization ratio decreased rapidly after the shower.

Figure 3.8 shows the 30 minutes averaged backscatter coefficient (β) and depolarization ratio (δ) during the dust event on June 14, around 21:20 UTC, when there is sun-photometer measurement available. The shaded areas show the standard deviation. The blue curve shows the βp from the ceilometer, which is also retrieved from 30-minutes-average and 100 m smoothed measurements. The lidar data were validated using the CNR filter, and the signal above 2 km were considered as noise. The β profiles from both instruments show a

similar vertical structure, with an elevated layer from 0.7 to 2 km, and the peak value at around 1.4 km. The absolute β value is different between lidar and ceilometer, one reason is the wavelength difference of these two instruments, and more importantly, βp from ceilometer is the retrieved particle backscatter coefficient while β from lidar is the relative backscatter coefficient, which was not calibrated using AOD. The mean depolarization ratio value for the aerosol layer was around 0.35 in this case, and it was nearly height independent, which means the particle type is constant throughout the profile, and the depolarization ratio is independent of the backscatter coefficient or aerosol concentration. There are two small peaks at around 0.6 km and 1.8 km, which can also be found in the cross-section figure 3.6. The peaks can be attributed to the focal effect caused by profile-to-profile changes in the lidar focus.

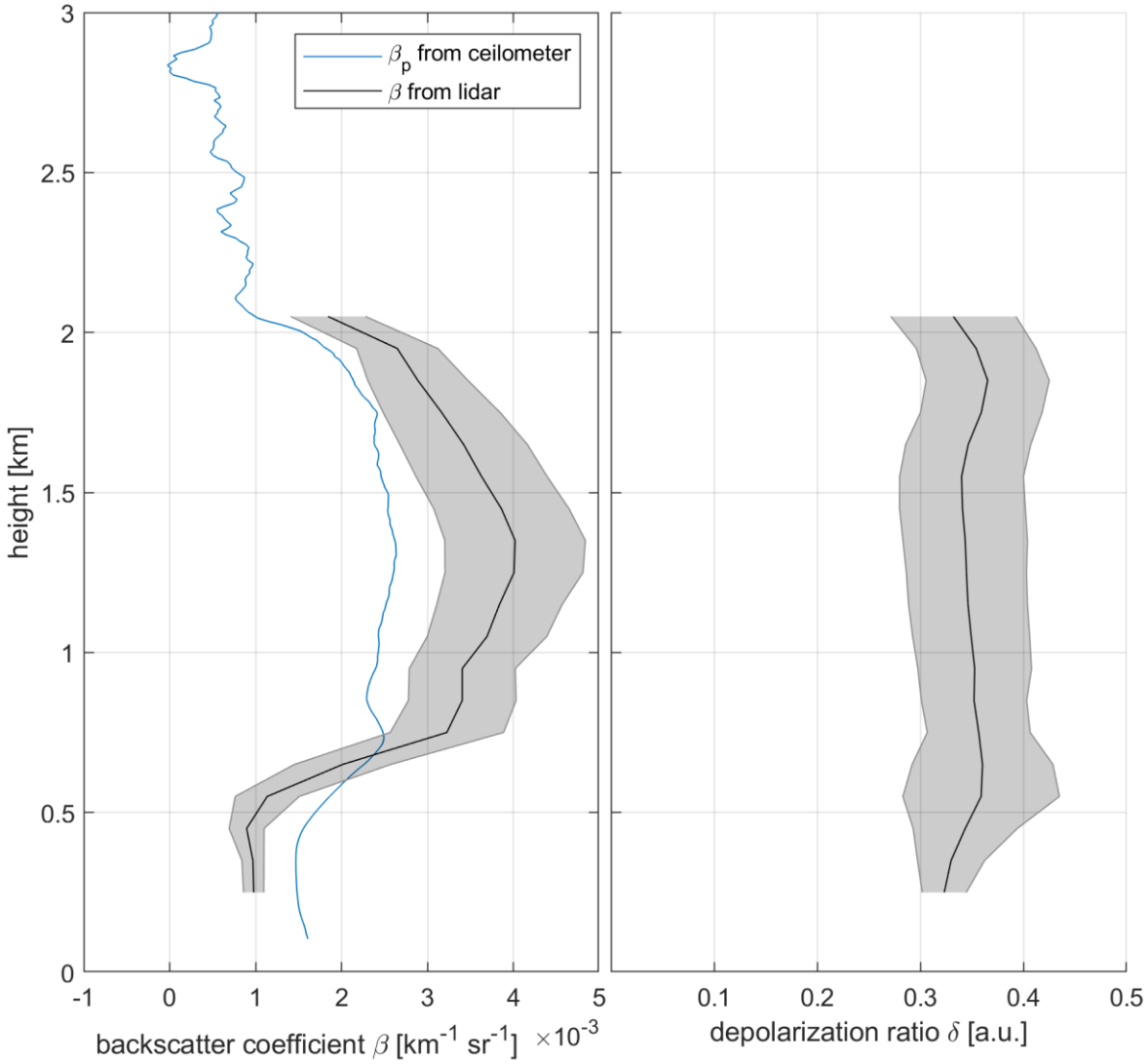

Figure 3.8 Left panel: 30-minutes-average (solid black line) of lidar β [km^{-1} sr^{-1}] and ceilometer (blue line) retrieved β_p [km^{-1} sr^{-1}] at 21:20 on June 14, 2019, Reykjavik. The shaded area shows the standard deviation. Right panel: lidar δ from the same period. The lidar data is filtered by CNR.

3.3.2 The July case (July 31 and August 1)

On July 31, 2019, a dust storm reached both Reykjavik and Keflavik airport. The data

processing method is the same as in the June case, described in section 2, but the main difference is that the ceilometer at Keflavik airport was not calibrated. The weather observation registered decreased visibility at 06:00 UTC, July 31. From 15:00 UTC July 31 to 12:00 UTC August 1, the 3 hourly weather observation reported haze. The visibility change due to the dust event can be seen in Figure 3.9, which shows the photos taken by the north-looking webcam installed at IMO headquarters, on July 31 and August 1, at 05:50 UTC. As in the June case, Mt. Esja was obscured during this episode. Unlike the June case, the wind in the morning of July 31 was easterly, and combining the HYSPLIT and weather conditions, the origin of the dust is considered to be from the west of the Icelandic highlands, on the west of Vatnajokull glacier, the largest ice cap in Iceland (Figure 3.1, location D). The western highlands are also a common source of Icelandic dust (Dagsson-Waldhauserova et al., 2014; Arnalds et al., 2016; Butwin et al., 2020). PM 10 and PM 2.5 concentration in Reykjavik were high from the afternoon of July 31. They stayed at an elevated level in the afternoon of July 31 (see Figure 3.11(e)) and peaked around 05:00 UTC on August 1. However, compared to the June case, the PM 10 concentration is lower. The wind field (Figure 3.11(a) and (b)) changed around 13:00 UTC, July 31, when the wind direction at low levels (below 700 m) turned from easterly to southerly, and the wind speed decreased as well. At the same time, relative humidity (Figure 3.11 (d)) increased from below 50% to around 70%. There was no sun-photometer measurement during the peak pollution period, possibly the sun light was blocked by clouds or an aerosol layer (07:00 UTC July 31 to 06:00 UTC August 1). However, both AOD and Angstrom exponent was relatively high, which means the particle size was smaller than during the June case. This was in agreement with the PM measurement, as the PM 2.5 concentration was similar, but the PM 10 concentration was considerably lower in the July case. The weather at Keflavik (Figure 3.12) was similar to Reykjavik, except for the wind direction which kept stable on August 1 at KEF, and the relative humidity was higher.

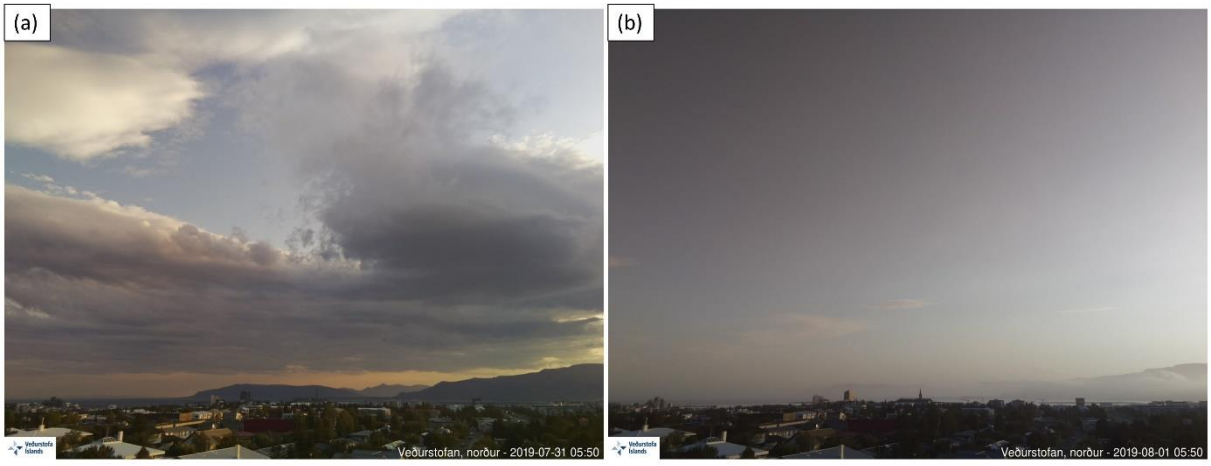

Figure 3.9 Photos taken by a web camera at IMO on July 31 (a) and August 1 (b), 2019, both dates at 05:00 UTC. The camera is looking northward and the view is the same as in Figure 3.5.

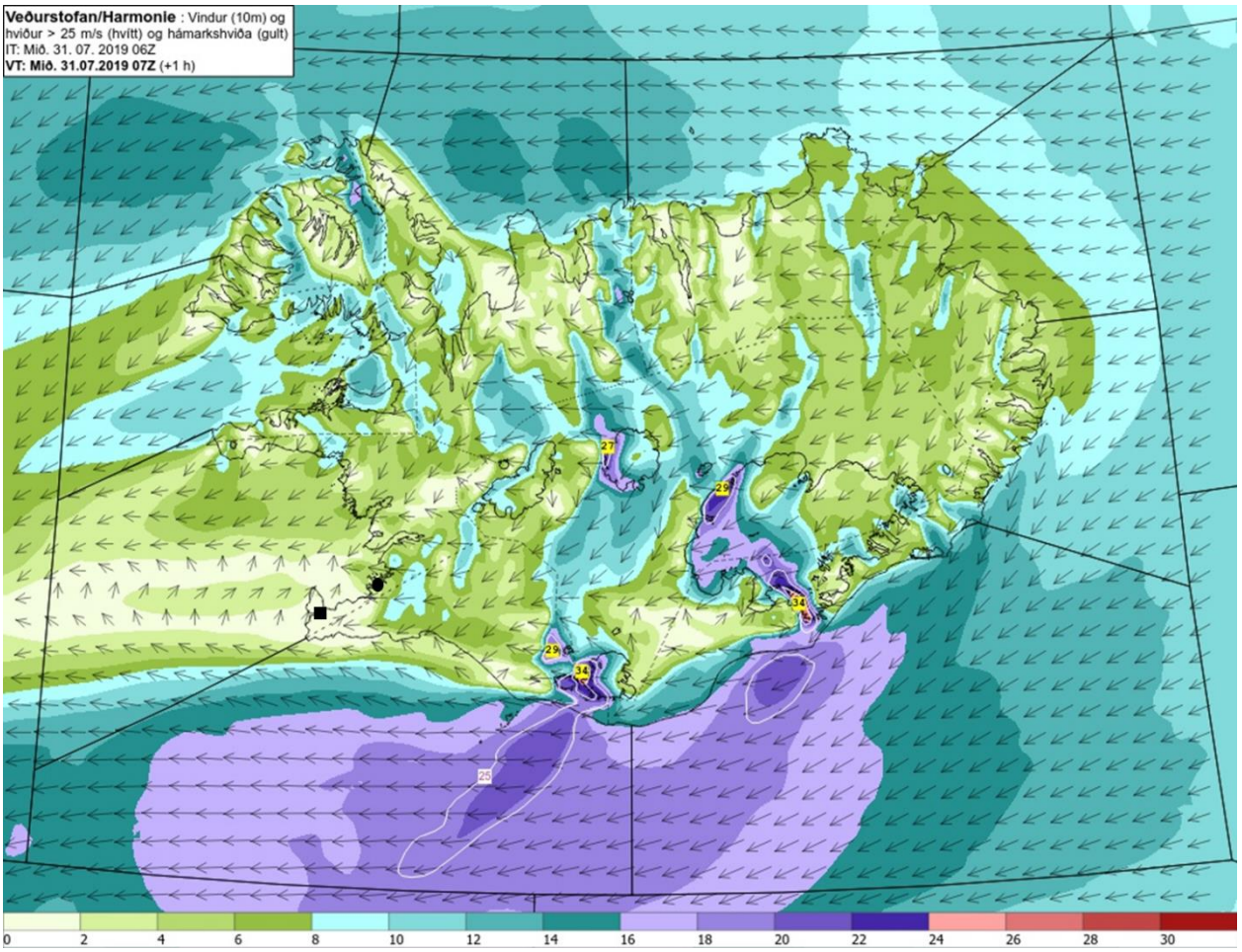

Figure 3.10 Wind conditions of the July case. The HARMONIE-AROME model forecast of 10 m wind at 07:00 UTC, July 31, 2019. The arrows indicate the wind direction while the colours indicate wind speed [m s^{-1}]. The black dot and square indicate the locations of RVK and KEF, respectively.

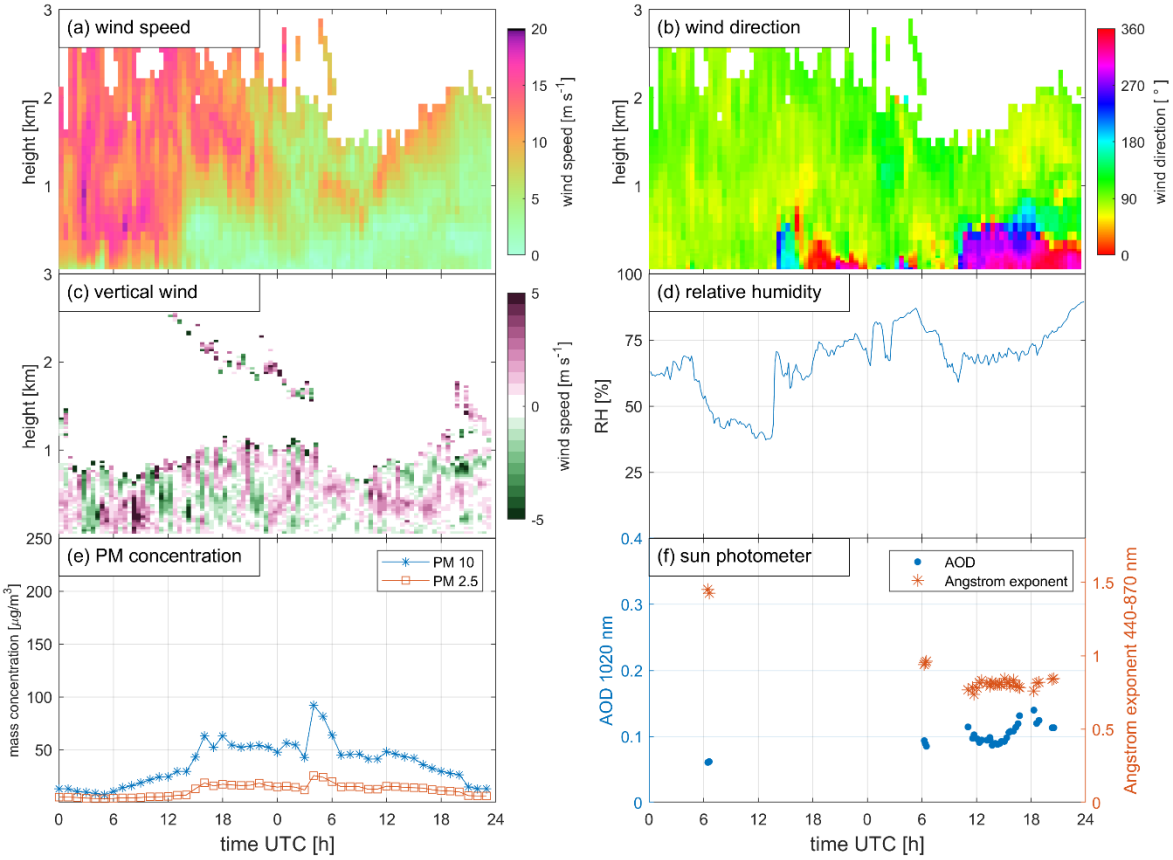

Figure 3.11 Wind speed (a, [m s^{-1}]), wind direction (b, [°]), vertical wind velocity (c, [m s^{-1}]), relative humidity (d, [%]), PM 10 (e, blue) and PM 2.5 (e, orange) concentration ([μm m^{-3}]), and sun-photometer observations (e) on July 31 and August 1, 2019, at RVK. The wind velocities are retrieved from lidar VAD scan. PM concentrations are measured at Njorvasund, Reykjavik. The relative humidity is measured at the weather station at IMO headquarters. The blue dots in (f) are AOD at 1020 nm, and the orange asterisk markers are Angstrom exponent (440-870 nm). The time axis starts from 00:00 UTC, July 31, 2019.

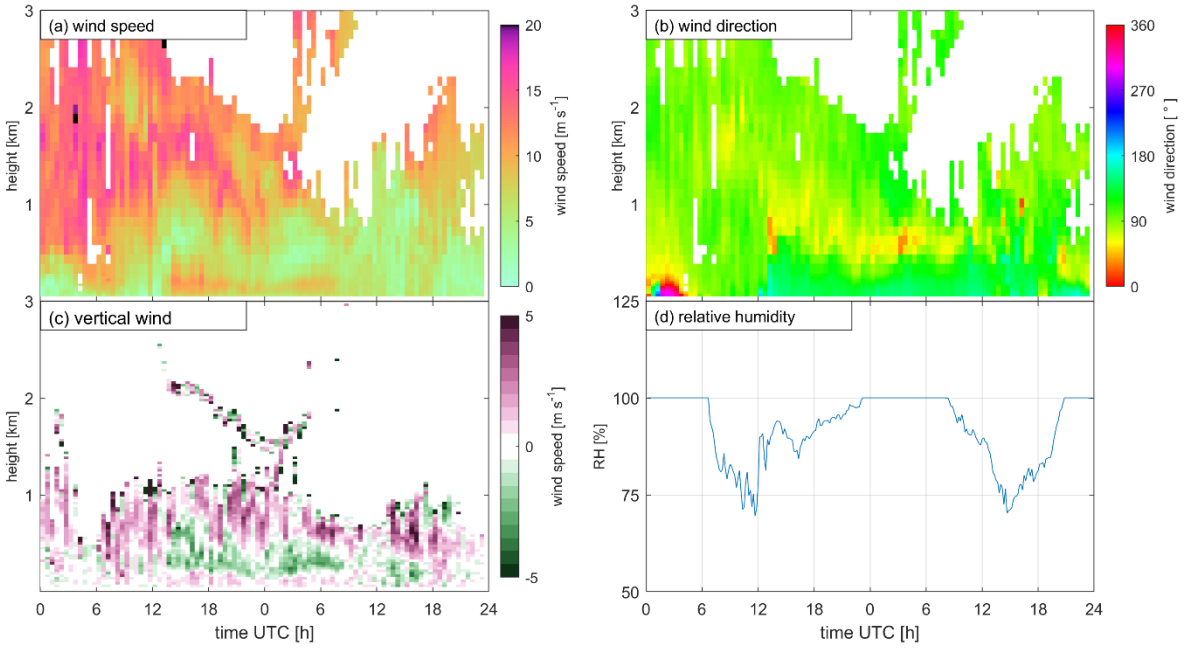

Figure 3.12 Wind speed (a, [m s^{-1}]), wind direction (b, [°]), vertical wind velocity (c, [m s^{-1}]), relative humidity (d, [%]) on July 31 and August 1, 2019, at KEF. The wind velocities are retrieved from lidar VAD scan. The relative humidity is measured at the weather station at Keflavik International airport. The time axis starts from 00:00 UTC, July 31, 2019.

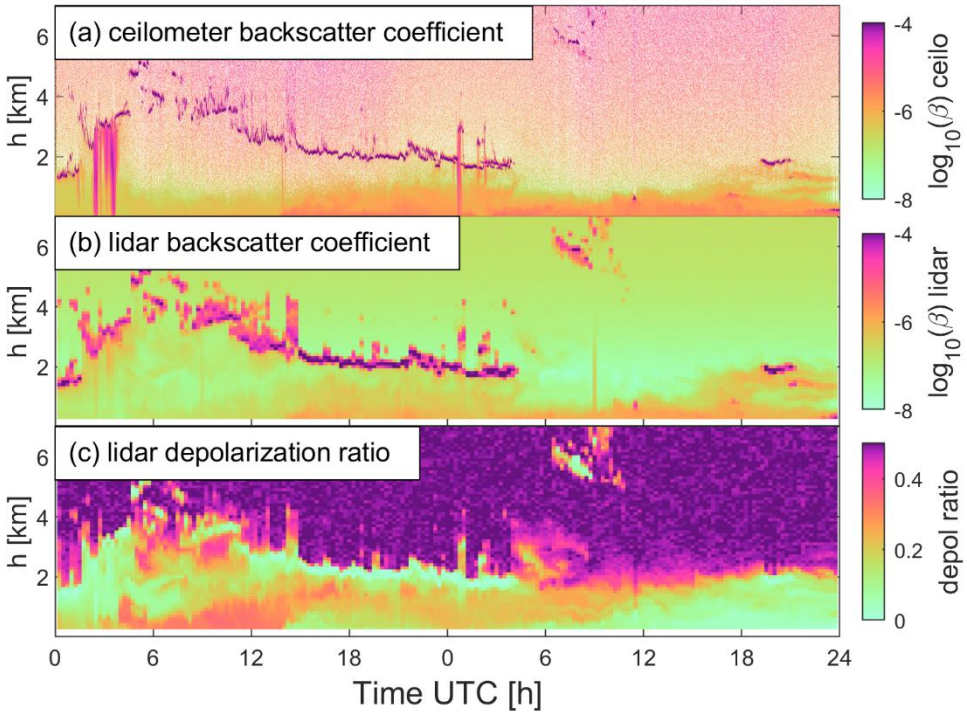

Figure 3.13 Time height cross-section of the backscatter coefficient from the ceilometer (a) and the Doppler lidar (b) as well as the lidar depolarization ratio (c) in Reykjavik, for 48 hours, from 00:00 UTC, July 31 to 24:00 UTC, August 1, 2019.

The lidar data is an average of 15 minutes. Note that the lidar measurements start at 200 m above the surface.

Figure 3.13 and Figure 3.14 show the measurements of the ceilometer and lidar backscatter coefficient as well as the lidar depolarization ratio at Reykjavik and Keflavik airport, respectively. The PM concentration increased slightly at around 05:00 UTC on July 31 and then increased more in the afternoon, not decreasing until the end of August 1. Both ceilometer and lidar backscatter coefficients revealed similar trends; close to the ground, a strong backscatter signal was detected after 13:00 UTC July 31 until the end of August 1. Precipitation was observed by ceilometer measurements at both sites around 03:00 UTC, July 31, while the lidar depolarization ratio was low. A layer with a high depolarization ratio was elevated untill 17:00 UTC, and decreased slightly after that. Similar observations can be found in Keflavik, where the depolarization ratio was higher in the morning of August 1, but the backscatter coefficient was low. The horizontal stripes in Figure 3.14(a) are instrument related (Kotthaus et al., 2016), and this ceilometer was not calibrated.

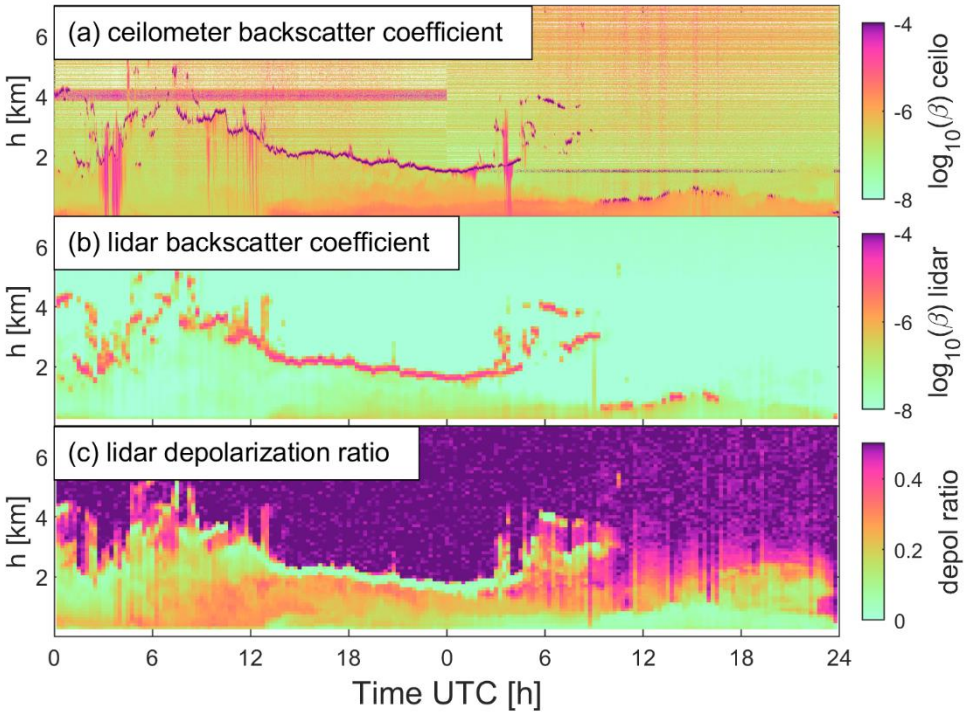

Figure 3.14 Time height cross-section of the backscatter coefficient from the ceilometer (a) and the Doppler lidar (b) as well as the lidar depolarization ratio (c) in Keflavik, for 48 hours, from 00:00 UTC, July 31 to 24:00 UTC, August 1, 2019. The lidar data is an average of 15 minutes. Note that the lidar measurements start at 200 m above the surface.

There is no sun-photometer measurement when PM concentration reaches a peak value, so we choose the measurement at around 06:20 August 1, when the AOD is around 0.1, still higher than in clean air (around 0.02), and present the backscatter coefficients and depolarization ratio profiles at the same time (Figure 3.13). Similar to the June case, lidar β and ceilometer β_p did not fully agree with each other, but here β_p was higher than β at the assumed depolarizing aerosol layer height (<1 km). It can be explained by different particle sizes: as noted, the origin of the two events varies, and the Angstrom exponent, in this case, was much higher than during the June case. The Angstrom exponent value was similar to

the one at no-dust level in the June case, which means the size of the particles, in this case, is much smaller. The wavelength of the ceilometer is shorter than lidar, which means the ceilometer is more sensitive to smaller particles than lidar. What should also be noted is that the depolarization ratio profile has a different shape than the backscatter coefficient, which will be discussed in section 3.4.

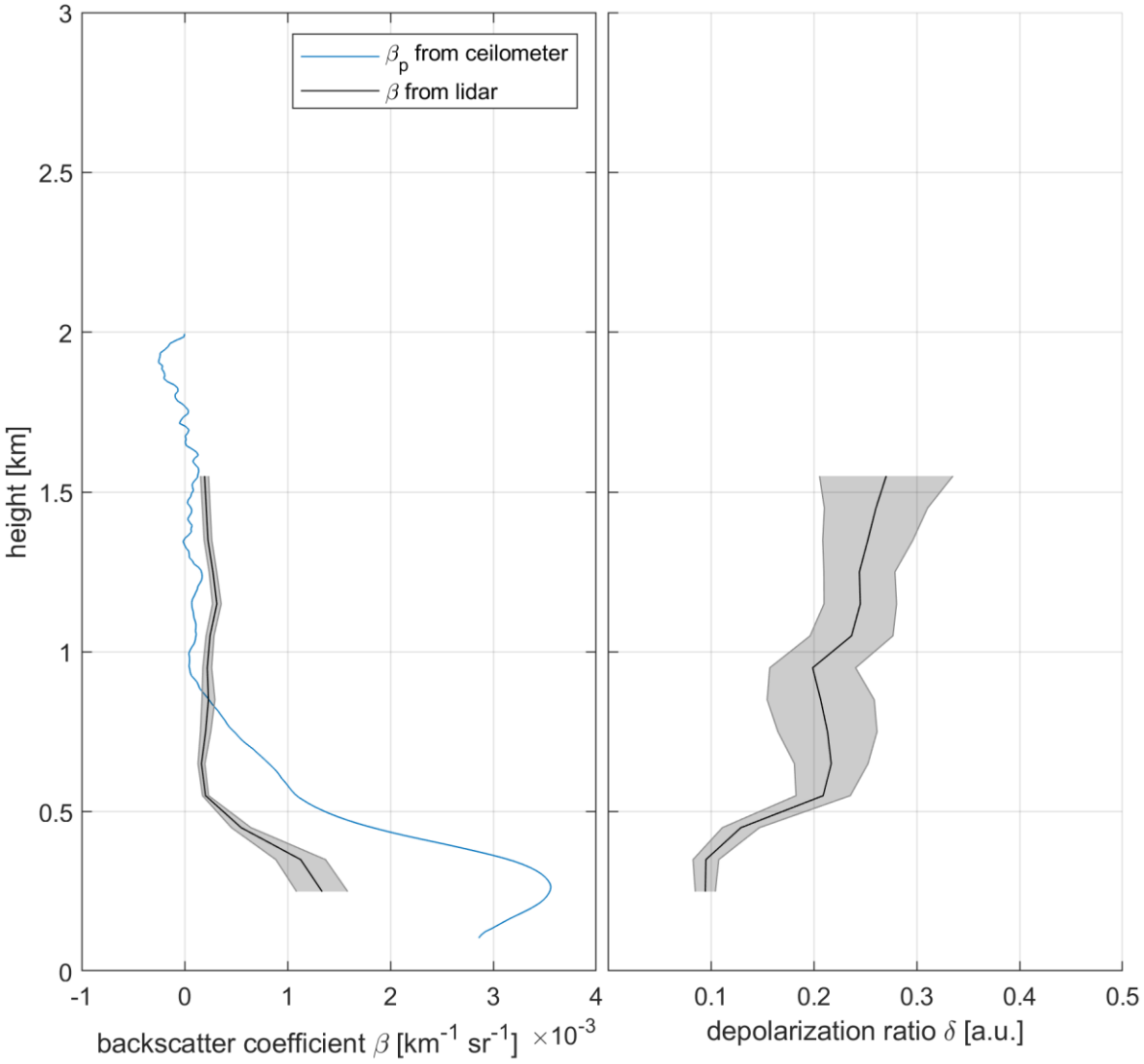

Figure 3.15 30-minutes-average (solid black line) of lidar β [km^{-1} sr^{-1}] and ceilometer (blue line) retrieved β_p [km^{-1} sr^{-1}] at 6:20 on August 1, 2019, Reykjavik. The shaded area shows the standard deviation. Right panel: lidar δ for the same period. The lidar data is filtered by CNR.

3.4 Discussion

From the results section, two main topics are discussed: (1) The different results obtained from the June and July case; (2) The differences between the lidar and ceilometer measurements.

3.4.1 The difference between June and July case

In both cases, dust events occurred during the summertime, but the lidar and ceilometer measurements differ. Firstly, in the June case, the ceilometer β_p value is lower than the lidar β value, at the level of the dust layer (Figure 3.8), while in the July case (Figure 3.15) it is the opposite. Secondly, in the June case, β and δ observations show a similar vertical distribution and temporal evolution (Figure 3.7), while in the July case they are more varied (Figure 3.13 and 3.14). There are several possible explanations: the different dust origins, which may lead to the different physical properties of dust particles, such as shapes and particle size distribution. The origins of both dust event, Lake Hagavatn (June case) and the Western Highlands (July case) are severe erosional areas and common source locations for dust in Iceland (Arnalds et al., 2016). Lake Hagavatn is a dry glacial lake, characterized by more crystalline materials than the volcanic glass that makes up most other Icelandic dust, while the Western Highlands area is covered with silty sediments as well as volcanic materials, and the particles are more spherical than other volcanic ash (Arnalds et al., 2016; Butwin et al., 2020). Figure 3.16 shows the size distribution measured by the sun-photometer. We used a different sky scenario based on data availability. The particle size in the June case (blue curve) was larger than in the July case (orange curve), and PM concentration measurements gave similar results. As mentioned above, the wavelength of the ceilometer is shorter than that of the lidar, thus the ceilometer is more sensitive to smaller particles, and accordingly, the ceilometer β_p value in July case is larger.

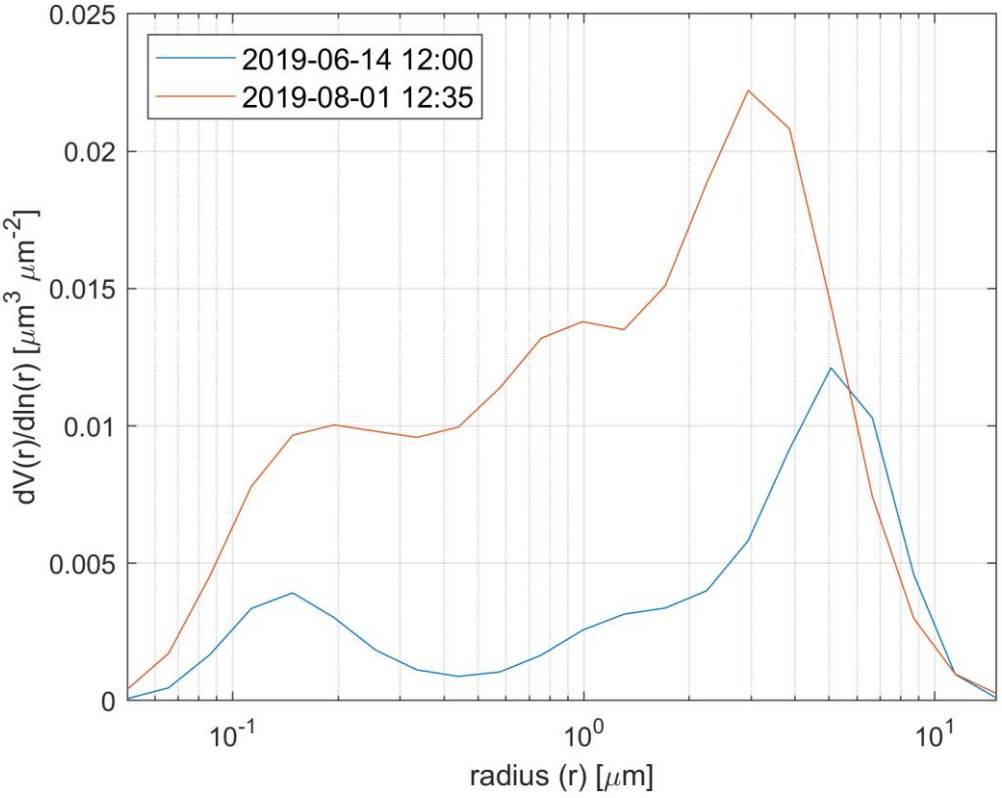

Figure 3.16 Particle volume size distribution for June 14 12:00 UTC (blue) and August 1, 12:35 UTC (red), measured by the sun-photometer. The observation is retrieved from AERONET level 1.5 production, with Almucantar (June, blue) and Hybrid (red, July) sky scenario accordingly, which is available online (see AP7).

The different weather conditions should also be considered. With the help of the HYSPLIT model, the dust origins of two cases remained unchanged during the episode accordingly, but in the July case, there was a clear advection of another air mass around 14:00 July 31, when wind field changes and relative humidity increased sharply, and again around 10:00 August 1, while relative humidity in the June case remained low. Figure 3.17 shows β and

δ versus relative humidity in June and July case. The relative humidity is recorded at the weather station next to the lidar trailer every 10 minutes, 2 m above the surface; β and δ only use the first range gate (200 m) measurements, averaged every 10 minutes. The colour indicates the PM 10 concentration. If we assume PM 10 concentration is high during the dust event, dust and non-dust observations in the June case can be easily distinguished in Figure 3.17(c). In general, there is a clear negative correlation between δ and RH, but high PM 10 measurements associated with high δ (>0.25) have a different pattern, compared to low PM 10 observations. The low PM10 dots are considered as a non-dust group and have a similar trend with Haarig et al. (2017) observation. In the July case, the measurements can be divided into three groups: 1) low PM group, which is similar to the non-dust group in the June case, also shows a negative correlation between δ and RH; 2) the relative high RH (>60%) high δ (>0.25) group, which is similar to the dust group in the June case, but the PM10 concentration is lower, corresponding to the high δ, low β measurement in the morning of July 31 (Figure 3.13); 3) the relative high RH, mid δ (0.1 - 0.2) group, which has no significant correlation between RH and δ, could represent the particles that absorbed water vapour. The AOD measurements are around 0.07, which is still higher than the background value (i.e. 0.02), but much lower than the peak value during the June case (0.3). The PM concentration increased in the morning when weather observation reported decreased visibility and the high depolarization ratio suggested a layer of non-spherical particles. A possible explanation is that the depolarization ratio measurements are only sensitive to the shape but not the concentration of aerosols. Thus, in some cases, if the particles are non-spherical with a low concentration, it will be easier to detect them by depolarization ratio than backscatter coefficient. In the morning of July 31, the aerosol concentration was relatively low, compared to the peak value, so the dust aerosols can easily be observed by the depolarization ratio but not by backscatter coefficient. In the afternoon of July 31, with increased relative humidity, the particles absorbed water vapour and became more spherical, so the depolarization ratio decreased. However PM concentration increased, which could be a result of transported aerosols accumulation, and naturally, the observed backscatter coefficient increased. To examine the specific relation between RH and lidar measurement, a more advanced lidar can be used which also measures humidity profiles (Haarig et al., 2017; Navas-Guzmán et al., 2019).

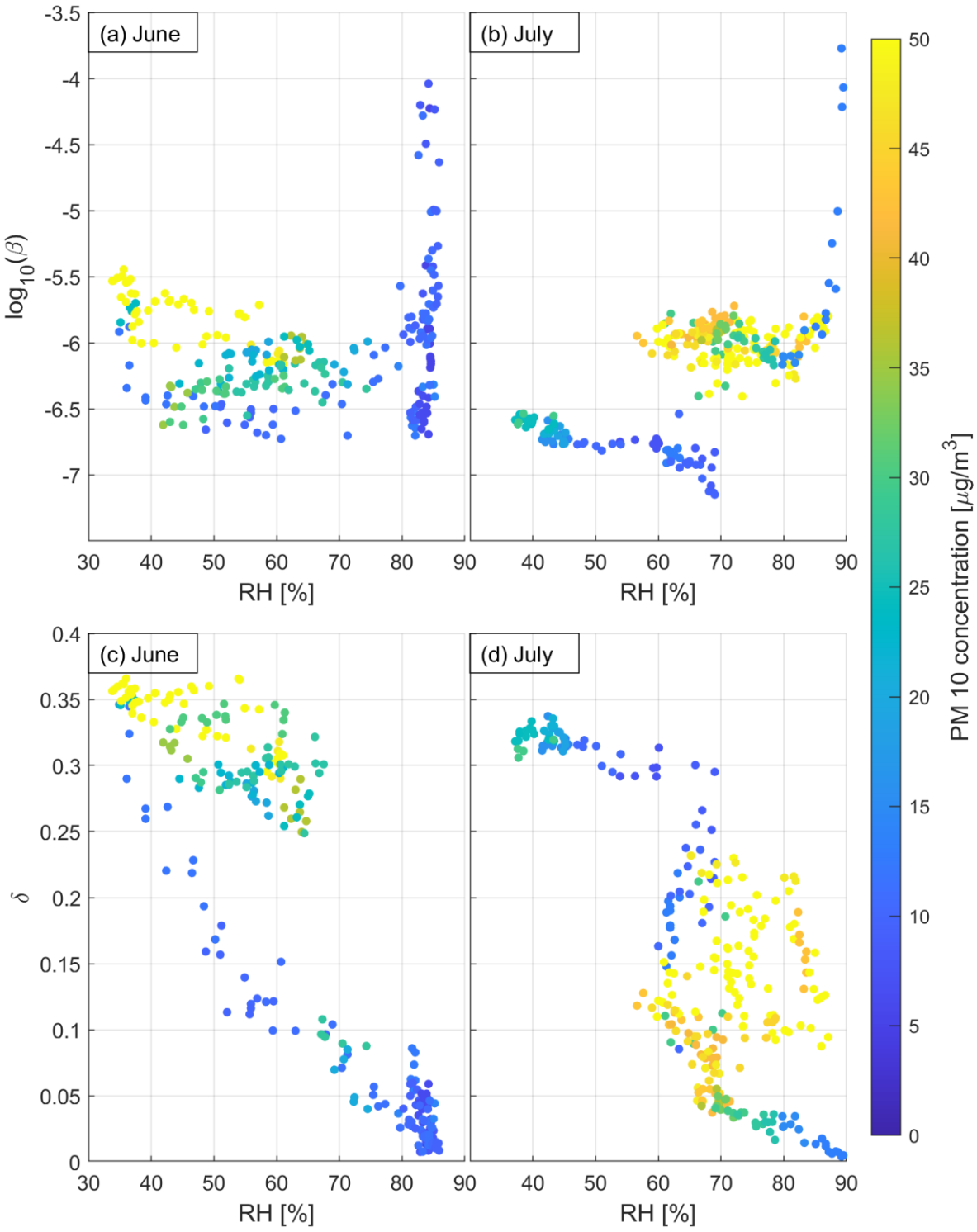

Figure 3.17 Backscatter coefficient (β) and depolarization ratio (δ) from lidar v.s. relative humidity (RH). RH is measured by the weather station every 10 minutes, and lidar data is averaged with the same temporal resolution. RH is measured 2 m above the surface, lidar data only use the first range gate (200 m). The colour indicates the PM 10 concentration.

3.4.2 The difference between lidar and ceilometer measurements

As is shown in Figure 3.8 and 3.15, the ceilometer β_p and lidar β profiles do not fully agree

with each other but were similar in trend. First, there are two facts we need to keep in mind: 1) the lidars and ceilometers have different wavelengths (1540 nm v.s. 910 nm), therefore the results of measuring scatterers with different size distributions are expected to be different; 2) The ceilometer profile is calibrated by Rayleigh curve and retrieved by Klett inversion. In other words, it has removed the effect of Rayleigh scattering from atmospheric molecular and extinction. While the lidar, on the other hand, was calibrated by the focus function, which neglects the impact of extinction. In short, β_p (for the ceilometer) and β (for the lidar) are different physical variables, with different measuring wavelengths, and accordingly, only their relative distribution can be compared.

Furthermore, an unexpected cosmetic shift of ceilometer profiles occurs in some cases. The $CNR_{\perp}$ profiles may occasionally not perform as expected. It is difficult to have a quantitative comparison between these two instruments, but they both detected the aerosol layer similarly and showed similar patterns in the cross-sections and vertical profiles.

3.5 Conclusions

In this study, two types of active remote sensing systems were used to detect atmospheric aerosols in Iceland. Two Doppler wind lidars (WindCube 200S, Leosphere) with depolarization channels and ceilometers (CL31 and CL51, Vaisala) were deployed in southwest Iceland. The data were supplemented by a sun-photometer (CE318-T, Cimel), webcams, radiosonde measurements, and weather observations, as well as PM concentration measurements, to allow calibration and validation of the remotely sensed aerosols monitoring. The study explores the procedures to process lidar and ceilometer data, which is the first to explore the use of WindCube 200S with depolarization module for aerosol detection and demonstrates the application of the procedure to two dust events that occurred during the summer of 2019. The data are analyzed and compared with observations from the sun-photometer and the PM measurements.

The results reveal that both lidar and ceilometer observations can detect airborne dust particles. The main findings from this study can be summarized as follows:

1. The two instruments consistently reveal similar vertical distributions of aerosols during both dust events. However, the absolute backscatter coefficient profiles are challenging to derive and compare, due to the different nature of the two instruments. Nevertheless, spatial and temporal distributions observed in lidar and ceilometer data are confirmed by observations from other measurements like PM concentration.

2. During the processing of lidar and ceilometer data, unrealistic signals have been identified. The F^{CS} factor as an empirical constant has been introduced to correct the unrealistic ceilometer data, which could also be a key source of uncertainty. With the backward Klett inversion method, the particle backscatter coefficients can be retrieved from ceilometer measurements. The lidar data has been calibrated for the focal effect to retrieve the correct relative backscatter coefficient profiles. The difference between lidar and ceilometer can be explained as i) differences in calibration and data processing procedure, and ii) different laser wavelengths.

3. Distinct differences between two dust events have been identified: during the June case, the lidar backscatter coefficient was larger while the ceilometer derived backscatter coefficient was larger during the July case. Particle size distribution

retrieved from the sun-photometer revealed that the particle size was larger in the June case, which explains why lidar backscatter coefficients were larger than ceilometers' in the June case, since the wavelength of Doppler lidar is longer.

4. Dust particles are expected to be non-spherical, with the detection of high depolarization ratio and high backscatter coefficients during a dust event. The depolarization ratio observed in this study is distinctively different during the two dust events. In the June case, the depolarization ratio revealed a similar temporal and vertical distribution as the backscatter coefficient, as expected. In the July case, depolarization ratio was high in the morning of July 31 while the backscatter coefficients were relatively low. The backscatter coefficients increased from the afternoon of July 31 but the depolarization ratio was, on the contrary, relatively low. The backscatter coefficients are directly related to the aerosols concentration while the depolarization ratio is less dependent on aerosol concentration. It is determined by the shape of the scatterers, which can be affected by relative humidity. The air remained dry in the June case and both backscatter coefficient and depolarization ratio measurements show a similar pattern. In the July case, relative humidity varied a lot during the two-day observation period. Consequently, we can conclude that when the air is dry and the particle concentration relatively high, the dust can be observed from both backscatter coefficient and depolarization ratio measurements; when the air is dry but particle concentration is low, the aerosols layer may be observed by depolarization ratio but not backscatter coefficients; when air is humid and the particles condense, the aerosols are more obvious from backscatter coefficient compared to depolarization ratio measurements. In general, the relative humidity may have a significant impact on lidar measurements, including backscatter coefficients, depolarization ratio, and also extinction coefficients, which is critical to aviation meteorology (Gultepe et al., 2019).

Finally, based on our results we conclude that Doppler wind lidars and ceilometers can provide accurate monitoring of the vertical distribution and temporal evolution of aerosols in Iceland. By installing the instruments on a mobile trailer, the presented data processing approach can be used to alert the local population of severe wind erosions events or ash clouds during volcanic eruptions. Such monitoring of volcanic and sedimentary aerosols can provide important information to decision makers, including an increase in aviation safety in Iceland.

3.6 Appendix

AP1. Lidar CNR uncertainties calculation

In the calculation of the CNR uncertainties, we use the power spectrum, as recommended by ISO for radial wind speed assessment (ISO, 2017). Instead of using the power spectrum of radial wind speed, however, we use the power spectrum of CNR. Along the time axis, we calculate the power spectral density (PSD) for each range. An example is shown in Figure A1 to illustrate the method. From this spectrum, we calculate the uncertainty of CNR. At high frequencies, the power spectrum is dominated by a flat level due to noise (green line in Figure A1). The uncertainty σ is given by

$$\sigma = \sqrt{\Delta f * \varphi} \qquad \text{(eq. A1)}$$

where bandwidth Δf corresponds to the frequency region of the flat level (about 0.5 Hz in the example in Figure A1), and the average PSD value at the flat level is φ (0.1 dB2/Hz in the example). Hence, in the example in Figure A1, CNR uncertainty σ_{CNR}at range, 2040 m was approximately 0.22 dB. Analyzing data from the two IMO lidars from two case studies, we found CNR uncertainties within aerosol layers of less than 1 dB in June 2019, and less than 0.5 dB in July/August 2019, respectively.

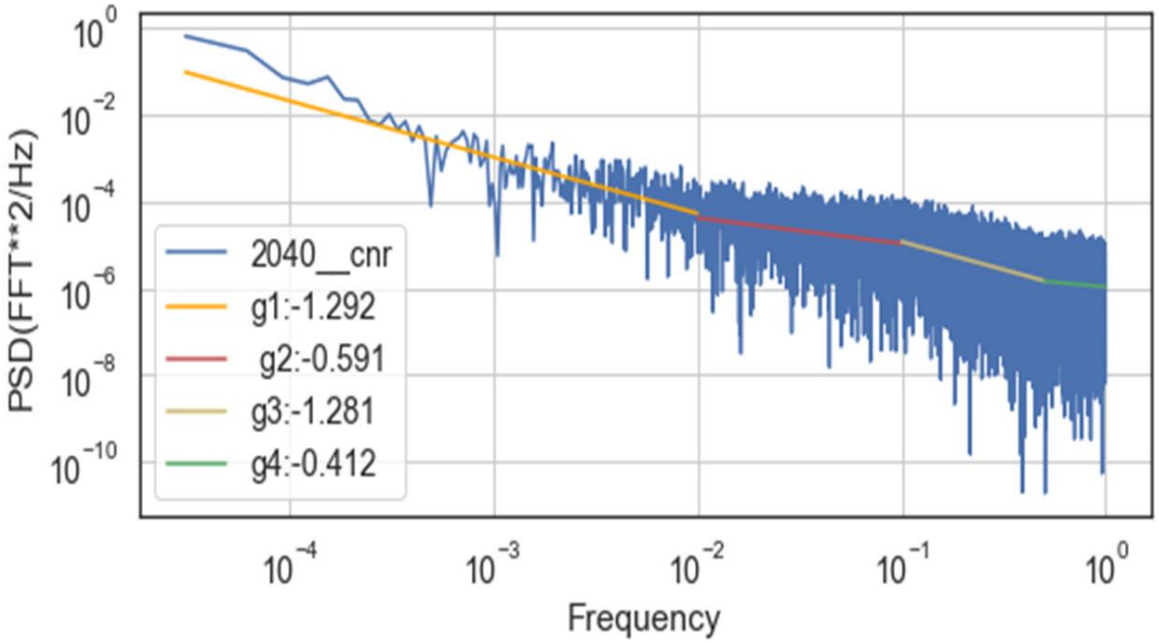

Figure A1 Log-log plot of CNR power spectrum along time within 24 h, at range 2040 m of a WindCube Scan 400S, using test data from Leosphere facilities. Coloured lines g1 to g4 mark the gradients of linear regression lines of different sections of the spectrum.

AP2. Lidar data processing: relative backscatter coefficients retrieval

The relative attenuated backscatter coefficient at a certain range gate x can be expressed as:

$$\beta_{relative}(x) = \beta_{calibration}(x) \times 10^{\left(\frac{CNR(x)-f_{dB}(x)}{10}\right)} \quad \text{(eq A2)}$$

where $\beta_{calibration}(x)$ is the calibrated backscatter coefficient, $CNR(x)$ is the CNR in dB at range x, and $f_{dB}(x)$ is the telescope function in the logarithmic scale (in dB). $\beta_{calibration}$ is a calibration value determined by several parameters:

$$\beta_{calibration}(x) = \beta_{ref} \times 10^{\left(\frac{f_{max}+\Delta CNR-CNR_{ref}}{10}\right)} \quad \text{(eq A3)}$$

CNR_{ref} and β_{ref} are reference values that were determined by the manufacturer during a calibration field campaign and directly link the CNR values to the relative backscatter coefficient. ΔCNR is an offset CNR value, depending on the pulse length or vertical resolution of lidar. In our case, we use 100 m resolution, corresponding to -3 dB. f_{max} is the maximum value of f_{dB}, which is the peak value at the focus point. The telescope function f(x), also called the Lorentzian curve fit function, is determined using data obtained during a calibration scan under homogeneous conditions. The fitting function is:

$$y(x) = y_0 + \left(\frac{2A}{\pi}\right)\left(\frac{w_0}{4(x-x_0)^2+{w_0}^2}\right) \quad \text{(eq A4)}$$

where y(x) is the CNR at range x in linear scale, x_0 is the focal length, y_0 is the noise floor, A is the amplitude above the noise floor, and w_0 is the full width at half maximum. Four

fitting parameters (x_0, y_0, A, w_0) were calculated for each valid profile during the calibration scan, and the mean value of all fitting results are the parameters we used for the Lorentzian curve fit function:

$$f(x) = y_0 + \left(\frac{2A}{\pi}\right)\left(\frac{w_0}{4(x-x_0)^2+{w_0}^2}\right) \qquad \text{(eq A5)}$$

With this function, we are able to retrieve the relative backscatter coefficient $\beta_{relative}$ from CNR, using equation A2. This $\beta_{relative}$ is not only range corrected but also focus corrected, backscattered signal received by lidar. This calibration should be done whenever the lidar was moved or reset. The transmission term of the lidar equation is considered negligible, at least for near-field range gates. The focal correction is applied for all lidar backscatter coefficients (β) presented in this work.

AP3. Lidar data processing: depolarization ratio retrieval

The scanning WindCube detects a total backscattered signal and the fraction of the signal that is perpendicularly polarized, relative to the polarization of the emitted beam. The lidars do not store received signals directly, but CNR in dB, which is the signal intensity on a logarithmic scale. In depolarization mode, the lidar will store $CNR_{\perp}$ (perpendicular) and CNR_{total}, which is the combination of $CNR_{\perp}$ and $CNR_{\parallel}$ (parallel), separately. Then depolarization ratio (δ) is defined by eq. A6 and eq. A7:

$$\delta = \frac{1}{1+\mathrm{P}} \qquad \text{(eq A6)}$$

where P indicates the power received by lidar parallel to the plane of polarization direction:

$$P = 10^{(CNR_{total}-CNR_{\perp})/10} \qquad \text{(eq A7)}$$

The depolarization ratio ranges from 0 to 1: the value close to 0 means particles can be assumed to be spherical, which is the case for liquid droplets, such as cloud droplets. On the contrary, a larger value indicates the particles are non-spherical, which means they are more likely to be solid particles, such as ice, dust, or ash particles.

AP4. Lidar data processing: data screening

The lidar output is expected as one CNR_{total} profile followed by one $CNR_{\perp}$ profile when depolarization mode is turned on. However, due to the instrumental instability, sometimes there will be $CNR_{\perp}$ profiles missing. Figure A2 shows the time height cross-section of CNR (top panel) and δ (bottom panel) on July 28, 2019. The left panels (a and c) show the original data and the right panels (b and d) show the data screened by the lag time between profiles. Figure A2(a) shows the original CNR data on July 28, 2019, and vertical stripes reflect missing $CNR_{\perp}$ profiles. Consequently, we screen the data by checking the time difference between two consecutive CNR_{total} profiles. The time difference depends on the scan strategy, and in our case, it is around 2.7 seconds. We exclude all the profiles with corresponding time reference longer than 3 seconds, and the results are shown in Figure A2(b). In this way, most stripes are removed. Lidar calculate δ only when both $CNR_{\perp}$ and CNR_{total} profiles are available, thus the stripes removed from δ profiles. We will use the same data screening strategy for all lidar data for consistency, including the backscatter coefficient and depolarization ratio.

In some other cases, such as June 14 (Figure A3(c)), there are stripes when δ is high. This is observed in several cases and is caused by the change of the focal function parameter from one profile to another. Normally, the focus behaviour along the profile cancels out when

calculating the depolarization ratio. However, as $CNR_{\perp}$ and CNR_{total} are measured subsequently and not simultaneously, profile-to-profile changes in the telescope function can cause the artifact is shown in Figure A3 (c). The vertical stripes change colour around the focal length of about 700 m. This happens when the assumption of a constant telescope function from one profile to the next is not met. Then, δ can be underestimated below the focal point and overestimated above, or vice versa. With 15 minutes averaging, most stripes can be smoothed, and a qualitative analysis of δ is possible. In the same case, β is increasing with altitude in the noise regime. To remove the noise, we filtered the lidar data when the CNR reaches a threshold. Boquet *et al.* (2016) measured the CNR threshold for a WindCube 200s with 100 m resolution as -28.6 dB. Considering the atmosphere in Iceland is clean, we use -28 dB in this study. Figure A3(d) shows the temporally smoothed and CNR filtered results.

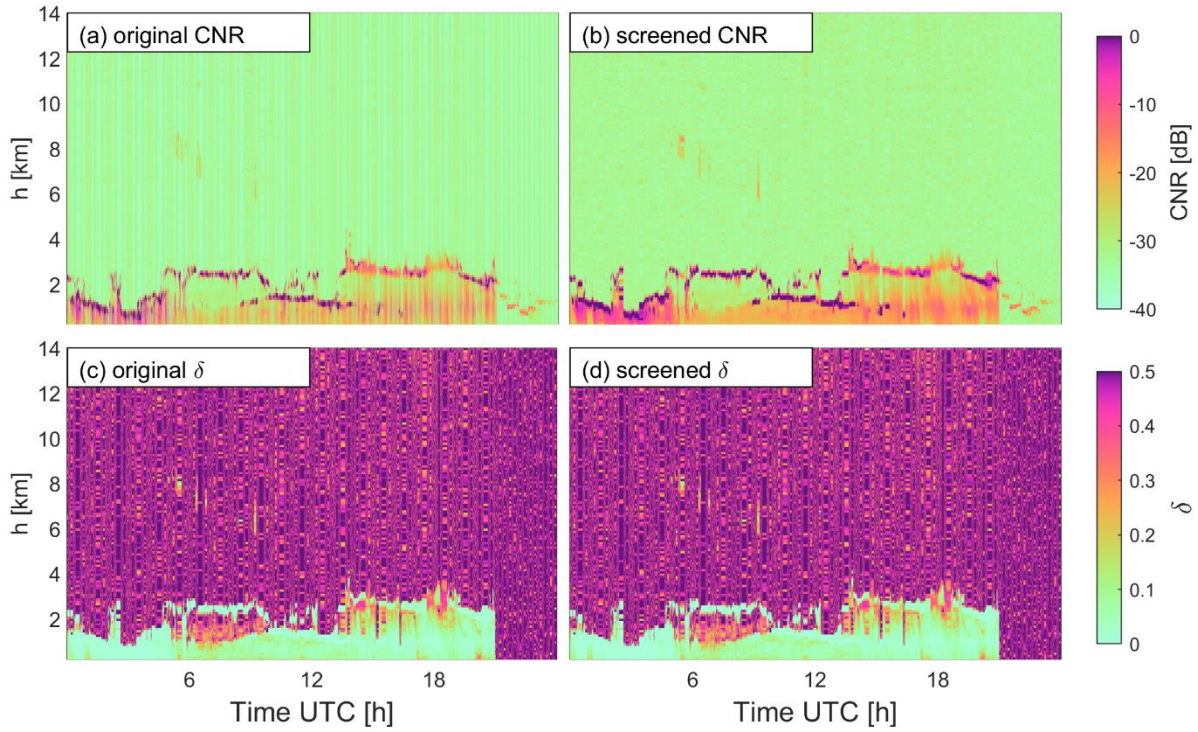

Figure A2 Time height cross-section of CNR (top panel) and δ (bottom panel) on 2019 June 28. The left panels (a and c) show the original data and the right panels (b and d) show the data screened by the lag time between profiles.

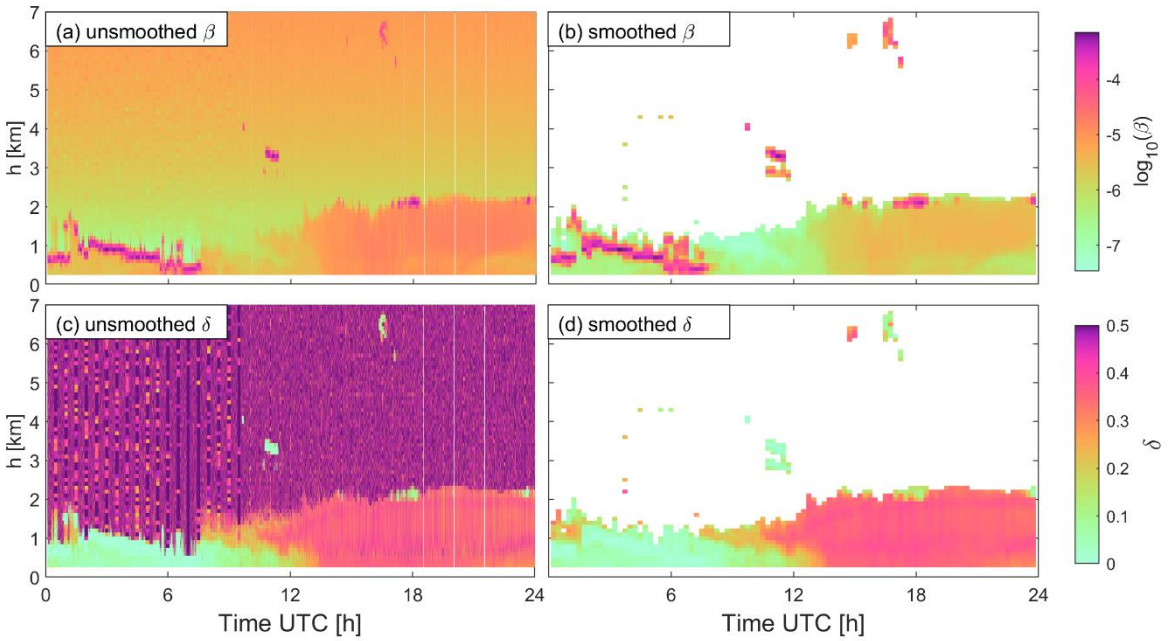

Figure A3 Time height cross-section of β (top panel) and δ (bottom panel) on 2019 June 14. The left panels (a and c) show the unsmoothed data and the right panel (b and d) shows the smoothed data with a 15 minutes average, and data points lower than -28 dB were removed.

AP5. Ceilometer dark measurement

The dark measurement, or termination hood measurement, can be done by covering the window of ceilometer using a termination hood. In this way, the entire emitted signal is attenuated, and the received signal can be attributed entirely to the background signal. In this study, we have performed two dark measurements with the ceilometer on the trailer (CL31): one is on December 3rd, 2018 and the other is on June 6th, 2019. Both measurements lasted around one day (~22 hours and 26 hours). In our study, we checked the signal at the 5th range gate (50 to 60 m) and use the profile when it reaches a stable characteristic value as the beginning of the dark measurement.

AP6. Factor C and cloud base height

The factor C used for ceilometer data correction is calculated as the mean value of factor C when there is no cloud and factor C is relatively stable, see the Figure A4 below.

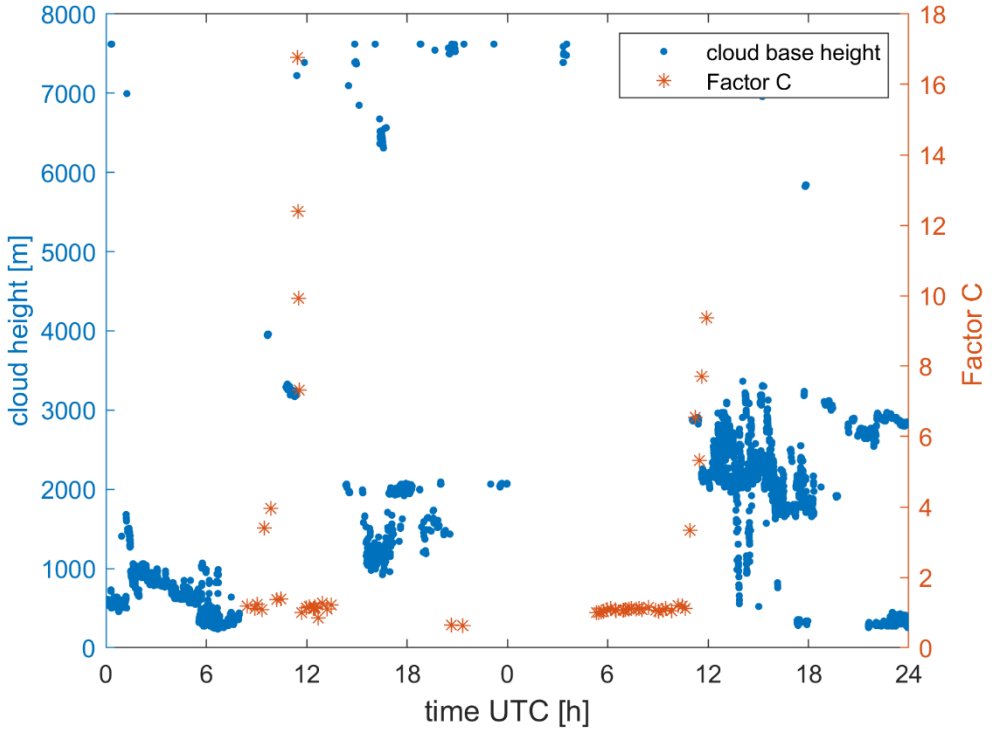

Figure A4 Cloud base height (blue) measured by ceilometer and factor C (orange) calculated based on ceilometer and sun-photometer measurements on June 14 and 15, 2019, at Reykjavik. The time axis starts from 00:00 UTC, June 14, 2019, covering two days.

AP7. Datasets available online

Some datasets are available online on the following websites.

Sun-photometer data from AERONET: https://aeronet.gsfc.nasa.gov/. Last accessed in September 2020.

PM10 and PM2.5 concentration measurements from the Environment Agency of Iceland: https://loftgaedi.is. Last accessed in December 2019. The instrument used for this study was BAM 1020 Continuous Particulate Monitor, the specifications can be found at https://metone.com/products/bam-1020/. Last accessed in November 2020.

Radio sounding measurements from at the University of Wyoming's website: http://weather.uwyo.edu/upperair/sounding.html. Last accessed in March 2020.

HYSPLIT backward trajectory simulation: https://www.ready.noaa.gov/HYSPLIT.php. Last accessed in August 2020.

AP8. Retrieval of ceilometer extinction coefficient profile

The backscatter signal measured by lidar/ceilometer at a certain range P(r) is expressed as:

$$P(r) = \frac{C_L}{r^2}\beta \mathrm{T}^2$$

where C_L is the lidar constant, assumed as 1 in this study; r is the range gate, β is the total backscatter coefficient and T^2 is the transmission term. The scattering of light in the atmosphere differs with the size of scatterers relative to the wavelength: if the scatterers are significantly smaller than the wavelength, the Rayleigh theory can be applied. If this is not the case the Mie theory has to be applied. In this study we treat the scatterers from aerosol particles (p) and molecules (m) separately:

$$\beta = \beta_p + \beta_m$$
$$\alpha = \alpha_p + \alpha_m$$

The particle lidar ratio $S_p = \frac{\alpha_p}{\beta_p}$ is assumed as a height independent value, in this case we use $S_p = 55\ sr$ (Ansmann et al., 2011).

After the correction of ceilometer RCS profiles (see example in Figure 2.2, left), we can apply the backward Klett inversion algorithm on the corrected RCS profile to retrieve the particle backscatter coefficient profile $\beta_p(r)$, and the extinction coefficient profile $\alpha_p(r) = \beta_p(r)S_p$. It also follows the conditions that the integrated extinction coefficient from ceilometer data agrees with AOD measured from sun-photometer (Wiegner & Geiß, 2012).

3.7 References

Ansmann, A. and Müller, D.: Lidar and Atmospheric Aerosol Particles, in Lidar: Range-Resolved Optical Remote Sensing of the Atmosphere, edited by C. Weitkamp, pp. 105–141, Springer, New York, NY., 2005.

Ansmann, A., Tesche, M., Groß, S., Freudenthaler, V., Seifert, P., Hiebsch, A., Schmidt, J., Wandinger, U., Mattis, I., Müller, D. and Wiegner, M.: The 16 April 2010 major volcanic ash plume over central Europe: EARLINET lidar and AERONET photometer observations at Leipzig and Munich, Germany: EYJAFJOLL ASH PLUME OVER EUROPE, Geophys. Res. Lett., 37(13), n/a-n/a, doi:10.1029/2010GL043809, 2010.

Arnalds, O., Dagsson-Waldhauserova, P. and Olafsson, H.: The Icelandic volcanic aeolian environment: Processes and impacts — A review, Aeolian Res., 20, 176–195, doi:10.1016/j.aeolia.2016.01.004, 2016.

Banakh, V. A., Smalikho, I., Köpp, F. and Werner, C.: Measurements of Turbulent Energy Dissipation Rate with a CW Doppler Lidar in the Atmospheric Boundary Layer, J. Atmospheric Ocean. Technol., 16(8), 1044–1061, doi:10.1175/1520-0426(1999)016<1044:MOTEDR>2.0.CO;2, 1999.

Bilbro, J., Fichtl, G., Fitzjarrald, D., Krause, M. and Lee, R.: Airborne Doppler Lidar Wind Field Measurements, Bull. Am. Meteorol. Soc., 65(4), 348–359, doi:10.1175/1520-0477(1984)065<0348:ADLWFM>2.0.CO;2, 1984.

Boquet, M., Royer, P., Cariou, J.-P., Machta, M. and Valla, M.: Simulation of Doppler Lidar Measurement Range and Data Availability, J. Atmospheric Ocean. Technol., 33(5), 977–987, doi:10.1175/JTECH-D-15-0057.1, 2016.

Brook, A., Ben-Dor, E. and Richter, R.: Fusion of hyperspectral images and LiDAR data for civil engineering structure monitoring, in 2010 2nd Workshop on Hyperspectral Image and Signal Processing: Evolution in Remote Sensing, pp. 1–5., 2010.

Budd, L., Griggs, S., Howarth, D. and Ison, S.: A Fiasco of Volcanic Proportions? Eyjafjallajökull and the Closure of European Airspace, Mobilities, 6(1), 31–40, doi:10.1080/17450101.2011.532650, 2011.

Burton, S. P., Ferrare, R. A., Hostetler, C. A., Hair, J. W., Rogers, R. R., Obland, M. D., Butler, C. F., Cook, A. L., Harper, D. B. and Froyd, K. D.: Aerosol classification using airborne High Spectral Resolution Lidar measurements – methodology and examples, Atmospheric Meas. Tech., 5(1), 73–98, doi:https://doi.org/10.5194/amt-5-73-2012, 2012.

Butwin, M. K., Pfeffer, M. A., Löwis, S. von, Støren, E. W. N., Bali, E. and Thorsteinsson, T.: Properties of dust source material and volcanic ash in Iceland, Sedimentology, 67(6), 3067–3087, doi:10.1111/sed.12734, 2020.

Carlsen, H. K., Gislason, T., Forsberg, B., Meister, K., Thorsteinsson, T., Jóhannsson, T., Finnbjornsdottir, R. and Oudin, A.: Emergency Hospital Visits in Association with Volcanic Ash, Dust Storms and Other Sources of Ambient Particles: A Time-Series Study in Reykjavík, Iceland, Int. J. Environ. Res. Public. Health, 12(4), 4047–4059, doi:10.3390/ijerph120404047, 2015.

Chan, P. W.: Application of LIDAR-based F-factor in windshear alerting, Meteorol. Z., 21(2), 193–204, doi:10.1127/0941-2948/2012/0321, 2012.

Chan, P. W. and Lee, Y. F.: Performance of LIDAR- and radar-based turbulence intensity measurement in comparison with anemometer-based turbulence intensity estimation based on aircraft data for a typical case of terrain-induced turbulence in association with a typhoon, J. Zhejiang Univ. Sci. A, 14(7), 469–481, doi:10.1631/jzus.A1200236, 2013.

Chazette, P., Dabas, A., Sanak, J., Lardier, M. and Royer, P.: French airborne lidar measurements for Eyjafjallajökull ash plume survey, Atmospheric Chem. Phys., 12(15), 7059–7072, doi:10.5194/acp-12-7059-2012, 2012.

Dagsson-Waldhauserova, P., Arnalds, O. and Olafsson, H.: Long-term variability of dust events in Iceland (1949–2011), Atmospheric Chem. Phys., 14(24), 13411–13422, doi:https://doi.org/10.5194/acp-14-13411-2014, 2014.

Dagsson-Waldhauserova, P., Renard, J.-B., Olafsson, H., Vignelles, D., Berthet, G., Verdier, N. and Duverger: Vertical distribution of aerosols in dust storms during the Arctic winter | Scientific Reports, Sci. Rep., 9(1), 1–11, doi:https://doi.org/10.1038/s41598-019-51764-y, 2019.

Gao, H., Cheng, B., Wang, J., Li, K., Zhao, J. and Li, D.: Object Classification Using CNN-Based Fusion of Vision and LIDAR in Autonomous Vehicle Environment, IEEE Trans. Ind. Inform., 14(9), 4224–4231, doi:10.1109/TII.2018.2822828, 2018.

Goudie, A. S.: Desert dust and human health disorders, Environ. Int., 63, 101–113, doi:10.1016/j.envint.2013.10.011, 2014.

Gryning, S.-E., Mikkelsen, T., Baehr, C., Dabas, A., Gómez, P., O'Connor, E., Rottner, L., Sjöholm, M., Suomi, I. and Vasiljević, N.: Measurement methodologies for wind energy based on ground-level remote sensing, in Renewable Energy Forecasting, pp. 29–56, Elsevier, Sawston, Cambridge., 2017.

Gústafsson, L. E. and Steinecke, K.: Airborne contaminants and their impact on the city of Reykjavi´k, Iceland, Sci. Total Environ., 160–161, 363–372, doi:10.1016/0048-9697(95)04369-C, 1995.

Gudmundsson, M. T., Pedersen, R., Vogfjörd, K., Thorbjarnardóttir, B., Jakobsdóttir, S. and Roberts, M. J.: Eruptions of Eyjafjallajökull Volcano, Iceland, Eos Trans. Am. Geophys. Union, 91(21), 190–191, doi:10.1029/2010EO210002, 2010.

Gultepe, I., Fernando, H. J. S., Pardyjak, E. R., Hoch, S. W., Silver, Z., Creegan, E., Leo, L. S., Pu, Z., De Wekker, S. F. J. and Hang, C.: An Overview of the MATERHORN

Fog Project: Observations and Predictability, Pure Appl. Geophys., 173(9), 2983–3010, doi:10.1007/s00024-016-1374-0, 2016.

Gultepe, I., Sharman, R., Williams, P., Zhou, B., Ellrod, G., Minnis, P., Trier, S., Griffin, S., Yum, S. S., Gharabaghi, B., Feltz, W., Temimi, M., Pu, Z., Storer, L., Kneringer, P., Weston, M. J., Chuang, H., Thobois, L., Dimri, A. P., Dietz, S. J., França, G. B., Almeida, M. V. and Neto, F. L. A.: A review of high impact weather for aviation meteorology, Pure Appl. Geophys., 176(5), 1869–1921, 2019.

Haarig, M., Ansmann, A., Gasteiger, J., Kandler, K., Althausen, D., Baars, H., Radenz, M. and Farrell, D. A.: Dry versus wet marine particle optical properties: RH dependence of depolarization ratio, backscatter, and extinction from multiwavelength lidar measurements during SALTRACE, Atmospheric Chem. Phys., 17(23), 14199–14217, doi:https://doi.org/10.5194/acp-17-14199-2017, 2017.

IMO: Tíðarfar í (Monthly report of) September 2019, Veðurstofa Íslands [online] Available from: https://www.vedur.is/um-vi/frettir/tidarfar-i-september-2019#sumar (Accessed 1 October 2020), 2019.

ISO: Air quality — Environmental meteorology, Part 2: Ground-based remote sensing of wind by heterodyne pulsed Doppler lidar. [online] Available from: https://www.iso.org/cms/render/live/en/sites/isoorg/contents/data/standard/05/92/59210.html (Accessed 29 September 2020), 2017.

Klett, J. D.: Lidar inversion with variable backscatter/extinction ratios, Appl. Opt., 24(11), 1638–1643, doi:10.1364/AO.24.001638, 1985.

Kotthaus, S., O'Connor, E., Münkel, C., Charlton-Perez, C., Haeffelin, M., Gabey, A. M. and Grimmond, C. S. B.: Recommendations for processing atmospheric attenuated backscatter profiles from Vaisala CL31 ceilometers, Atmospheric Meas. Tech., 9(8), 3769–3791, doi:https://doi.org/10.5194/amt-9-3769-2016, 2016.

Leosphere: Personal communication, 2020.

Liao, H., Jing, H., Ma, C., Tao, Q. and Li, Z.: Field measurement study on turbulence field by wind tower and Windcube Lidar in mountain valley, J. Wind Eng. Ind. Aerodyn., 197, 104090, doi:10.1016/j.jweia.2019.104090, 2020.

Münkel, C., Eresmaa, N., Räsänen, J. and Karppinen, A.: Retrieval of mixing height and dust concentration with lidar ceilometer, Bound.-Layer Meteorol., 124(1), 117–128, doi:10.1007/s10546-006-9103-3, 2007.

Navas-Guzmán, F., Martucci, G., Collaud Coen, M., Granados-Muñoz, M. J., Hervo, M., Sicard, M. and Haefele, A.: Characterization of aerosol hygroscopicity using Raman lidar measurements at the EARLINET station of Payerne, Atmospheric Chem. Phys., 19(18), 11651–11668, doi:https://doi.org/10.5194/acp-19-11651-2019, 2019.

Petersen, G. N., Bjornsson, H. and Arason, P.: The impact of the atmosphere on the Eyjafjallajökull 2010 eruption plume, J. Geophys. Res. Atmospheres, 117(D20), doi:10.1029/2011JD016762, 2012.

Prospero, J. M., Bullard, J. E. and Hodgkins, R.: High-Latitude Dust Over the North Atlantic: Inputs from Icelandic Proglacial Dust Storms, Science, 335(6072), 1078–1082, doi:10.1126/science.1217447, 2012.

Rix, M., Valks, P., Hao, N., Loyola, D., Schlager, H., Huntrieser, H., Flemming, J., Koehler, U., Schumann, U. and Inness, A.: Volcanic SO2, BrO and plume height estimations using GOME-2 satellite measurements during the eruption of Eyjafjallajökull in May 2010, J. Geophys. Res. Atmospheres, 117(D20), doi:10.1029/2011JD016718, 2012.

Saidou Chaibou, A. A., Ma, X. and Sha, T.: Dust radiative forcing and its impact on surface energy budget over West Africa, Sci. Rep., 10(1), 12236, doi:10.1038/s41598-020-69223-4, 2020.

Sicard, M., Guerrero-Rascado, J. L., Navas-Guzmán, F., Preißler, J., Molero, F., Tomás, S., Bravo-Aranda, J. A., Comerón, A., Rocadenbosch, F., Wagner, F., Pujadas, M. and Alados-Arboledas, L.: Monitoring of the Eyjafjallajökull volcanic aerosol plume over the Iberian Peninsula by means of four EARLINET lidar stations, Atmospheric Chem. Phys., 12(6), 3115–3130, doi:https://doi.org/10.5194/acp-12-3115-2012, 2012.

Statistics Iceland: Population by municipality, sex, citizenship and quarters 2010-2020, Popul. Munic. Sex Citizsh. Quart. 2010-2020 [online] Available from: http://px.hagstofa.is/pxis/pxweb/is/Ibuar/Ibuar__mannfjoldi__1_yfirlit__arsfjordungstolur/MAN10001.px/table/tableViewLayout1/?rxid=c9d9c074-79f2-40c2-8a30-5479757324ba (Accessed 5 October 2020), 2020.

Stein, A. F., Draxler, R. R., Rolph, G. D., Stunder, B. J. B., Cohen, M. D. and Ngan, F.: NOAA's HYSPLIT Atmospheric Transport and Dispersion Modeling System, Bull. Am. Meteorol. Soc., 96(12), 2059–2077, doi:10.1175/BAMS-D-14-00110.1, 2015.

Stephan, A., Wildmann, N. and Smalikho, I. N.: Effectiveness of the MFAS Method for Determining the Wind Velocity Vector from Windcube 200s Lidar Measurements, Atmospheric Ocean. Opt., 32(5), 555–563, doi:10.1134/S1024856019050166, 2019.

Thobois, L., Cariou, J. P. and Gultepe, I.: Review of Lidar-Based Applications for Aviation Weather, Pure Appl. Geophys., 176(5), 1959–1976, doi:10.1007/s00024-018-2058-8, 2019.

Tuononen, M., O'Connor, E. J., Sinclair, V. A. and Vakkari, V.: Low-Level Jets over Utö, Finland, Based on Doppler Lidar Observations, J. Appl. Meteorol. Climatol., 56(9), 2577–2594, doi:10.1175/JAMC-D-16-0411.1, 2017.

Thorsteinsson, T., Jóhannsson, T., Stohl, A. and Kristiansen, N. I.: High levels of particulate matter in Iceland due to direct ash emissions by the Eyjafjallajökull eruption and resuspension of deposited ash, J. Geophys. Res. Solid Earth, 117(B9), doi:https://doi.org/10.1029/2011JB008756, 2012.

Vaisala: Vaisala Ceilometer CL31 user's guide, 2004.

Wiegner, M. and Geiß, A.: Aerosol profiling with the Jenoptik ceilometer CHM15kx, Atmospheric Meas. Tech., 5(8), 1953–1964, doi:10.5194/amt-5-1953-2012, 2012.

Wiegner, M., Gasteiger, J., Groß, S., Schnell, F., Freudenthaler, V. and Forkel, R.: Characterization of the Eyjafjallajökull ash-plume: Potential of lidar remote sensing, Phys. Chem. Earth Parts ABC, 45–46, 79–86, doi:10.1016/j.pce.2011.01.006, 2012.

Wiegner, M., Madonna, F., Binietoglou, I., Forkel, R., Gasteiger, J., Geiß, A., Pappalardo, G., Schäfer, K. and Thomas, W.: What is the benefit of ceilometers for aerosol remote sensing? An answer from EARLINET, Atmospheric Meas. Tech., 7(7), 1979–1997, doi:10.5194/amt-7-1979-2014, 2014.

Wittmann, M., Groot Zwaaftink, C. D., Steffensen Schmidt, L., Guðmundsson, S., Pálsson, F., Arnalds, O., Björnsson, H., Thorsteinsson, T. and Stohl, A.: Impact of dust deposition on the albedo of Vatnajökull ice cap, Iceland, The Cryosphere, 11(2), 741–754, doi:https://doi.org/10.5194/tc-11-741-2017, 2017.

Yang, S., Petersen, G. N., Löwis, S. von, Preißler, J. and Finger, D. C.: Determination of eddy dissipation rate by Doppler lidar in Reykjavik, Iceland, Meteorol. Appl., 27(5), e1951, doi:10.1002/met.1951, 2020.

Chapter 4

Apply machine learning on Doppler lidar measurement

4.1 Introduction

The light detection and ranging system (lidar) is an active remote sensing instrument that is widely used for various purposes: from automatic-driving (Gao et al., 2018) and forestry (Dubayah and Drake, 2000) to aviation safety (Thobois et al., 2019; Yang et al., 2020a). In the meteorological sector, it is mainly used for wind measurements (Bilbro et al., 1984; Thobois et al., 2019) and aerosol detection (Ansmann and Müller, 2005). While conventional meteorological measurements are either continuous in time but at a single height, e.g. measurements in meteorological masts, or give a profile at a certain time only a few times a day, e.g. radiosondes, a lidar provides a continuous profile measurement with a high temporal and spatial resolution at the same time.

A lidar emits laser beams and receives the backscattered signal with the detected scatterers being e.g. aerosols, cloud droplets, and ice particles. A Doppler lidar can also retrieve the radial wind speed based on the Doppler effect by assessing the frequency change of the received signal (Thobois et al., 2019). The lidar signals can be weakened by high noise levels. The lidar signal gets attenuated by molecular absorption, which weakens the signal and subsequently, the noise backscatter signal becomes increasingly dominant with longer distances from the lidar system. A commonly used method to identify noise is to define a threshold of the carrier to noise ratio (CNR) for filtering the data, in some cases the signal to noise ratio (SNR) is used instead (Boquet et al., 2016; Gryning et al., 2016, 2017). However, in the daily use of lidars we found this method to be too coarse. We found that the distortion of the lidar signal can be large and the noise exceeded the threshold in some cases, or non-noise signals could not reach the thresholds, especially in the free troposphere, where the concentration of scatterers is in general low. Therefore, the lidar needs to be calibrated, which is complex and time-consuming. Foremost, the CNR threshold needs to be optimized and validated to identify the noise. Thus, it is ideal to find a way to identify and filter the background noise observed by a lidar, other than the conventional CNR filtering approach, which could perform better especially when the intensity of the scatterers is low.

After the background noise has been identified, lidar observations of different target classes, such as aerosols and clouds need to be interpreted. Frequently, lookup tables (LUT) are used to classify lidar measurements (Di Noia and Hasekamp, 2018). LUTs typically contain a combination of variables measured by the lidar, e.g. the lidar ratio, the backscatter coefficients, the colour ratio, the temperature and the relative humidity, as well as their respective thresholds (Ansmann and Müller, 2005; Groß et al., 2011; Chouza et al., 2015; Haarig et al., 2017). Some lidar manufactures, i.e. Leosphere Inc (Vaisala Group), can

provide a built-in automatic algorithm to classify the lidar signals (Leosphere, Inc, 2013). However, based on our experience the accuracy of this classification is rather low. Considering the environmental conditions are varied at different locations, validating this built-in algorithm is also time-consuming and requires high-skill. However, an automatic algorithm that classifies the lidar measurements in real-time, and is applicable to data from different instruments, is valuable to lidar end users.

Machine learning is a widely used method to classify data (Kotsiantis et al., 2006), and has been used on lidar measurements. Zeng et al. (Zeng et al., 2019) applied a k-means clustering method to classify cloud and aerosols from CALIPSO satellite-based lidar. Brakhasi et al. (Brakhasi et al., 2019) used the Random Forest (RF) and Support Vector Machine (SVM) algorithm to discriminate CALIPSO measured aerosols from clouds. Farhani et al (Farhani et al., 2020) applied both supervised and unsupervised machine learning methods to classify lidar measurements over the UK and identify the anomalies, which were considered as biomass burning aerosols, from other measurements. The machine learning method is considered capable to handle high-dimensional data and map classes with complex characteristics (Maxwell et al., 2018). Although machine learning has been used widely on remote sensing research, including lidar data analyses, it has not been applied on the lidar systems in Iceland, partly because this is a rather new approach, and also the performance of Doppler lidars in Iceland have not been studied until recently (Yang et al., 2020a, b). Whether the machine learning method can perform well on the unique lidar systems in Iceland under the subpolar and volcanic environment is still unknown.

Here we use machine learning algorithms to classify lidar backscatter signals from two Leosphere Doppler wind lidars, with the purpose of aerosols monitoring in Iceland. The sub-polar conditions in Iceland imply several challenges, such as a relatively clean atmosphere with low aerosol concentrations compare to the mid-latitude region, which leads to high noise levels, but also events of intense dust due to wind erosion, volcanic ash clouds, frequent ice clouds, and heavy precipitation events (Ólafsson et al., 2007; Yang et al., 2020a). This would be the first time that artificial intelligence is applied on the lidars in Iceland and provides an automatic measurement classification. In this study, we propose two separate steps to solve these problems. In the first step, we use the density-based spatial clustering of applications with noise (DBSCAN) clustering algorithm, combined with a conventional method, to identify the noise data. In the second step we use the Random Forest (RF) method, a well-established machine learning model, to classify the lidar data. Based on our extended experiments in the summer of 2019 (June to August), we show that our method achieves high accuracy and can classify the lidar backscatter in real-time. We will describe the data and methods used in section 4.2, present the results in section 4.3, discuss the results and give suggestions for future work in section 4.4 and summarize the conclusion in section 4.5.

4.2 Methodology

4.2.1 Instrument and data description

Two Leosphere WindCube 200S Doppler lidars are in use in Iceland, both were equipped with a depolarization module during this study period. One is located at Keflavik International airport while the other is on a mobile trailer, ready for rapid deployment during volcanic eruptions. During this study, the mobile lidar was located in Reykjavik, the capital city of Iceland. The basic specifications can be found in Table 4.1. The lidars were scheduled

with two scan strategies: Velocity-Azimuth-Display (VAD) scans, conic scans with a fixed elevation angle, for calibration and wind monitoring, and vertical stare for aerosol monitoring. In this study, we only use vertical stare measurements (Yang et al., 2020b). Here data from the lidar located in Reykjavik is used to train and test the models, and subsequently, data from the lidar located at Keflavik airport for testing the trained models. In the following section, if not specified otherwise, the lidar observations were collected by the mobile lidar in Reykjavik.

Table 4.1 The main specifications of the lidars in Iceland.

model	Windcube 200S
manufacturer	Leosphere Inc.
wavelength [μm]	1.54
detection range [m]	50 - 14000
range resolution [m]	25, 50, 75, 100
elevation angle [°]	-10—90
azimuth angle [°]	0—360

The primary output of the lidar is the two dimensional CNR. The relative backscatter coefficients (β) and depolarization ratio (δ) can be retrieved from CNR. The detailed methods to retrieve β and δ is described in (Yang et al., 2020b).

The data we use to train the models were collected from four days in 2019: June 14, June 15, July 31 and August 1. During these days, two dust storms were observed by weather observers, as well as other weather conditions, including low clouds, high clouds and rainfall. A detailed description of these two dust events and the lidar measurements can be found in Yang et al. (Yang et al., 2020b).

A complete lidar profile contains 139 range gates with a resolution of 100 m each. The time difference between the two profiles varied, from around 1.6 to 6 seconds. To shorten the processing time, 10% of the data were randomly selected for models training.

4.2.2 Machine learning algorithms

Machine learning is a popular method used to achieve some tasks which are relatively easy to do subjectively for a small data set but are difficult to achieve by conventional algorithms for large data sets, such as the classification of a large number of images. A number of algorithms have been developed based on Artificial Intelligence and Statistics (Kotsiantis et al., 2006). In general, there are two approaches, supervised and unsupervised learning. The main difference is that for the supervised learning the data needs to be labeled.

Random Forest (RF) classifier is a supervised ensemble classifier that uses a combination of decision trees to classify the target data set (Breiman, 2001). It is also called the bagged tree method since the data is split into the samples used for training the trees (in-bag samples) and the samples used for internal cross-validation (out-bag samples). The final prediction is made by a majority vote of the trees. Belgiu & Drăguţ (Belgiu and Drăguţ, 2016) reviewed the use of RF in remote sensing and revealed that RF classifier can successfully handle high dimensional data, and at the same time be fast and insensitive to over-fitting. RF has also been used for lidar measurements specifically. Brakhasi et al. (Brakhasi et al., 2019) used two algorithms including RF to discriminate aerosols from

clouds in satellite-based lidar measurements, and they found the method had higher accuracy compared to probability distribution functions based algorithms. Liu et al. (Liu et al., 2020) compared several machine learning algorithms on air pollution (SO2 and NO2) classification and found that RF can give a good result. RF is well-known for its competence in solving data imbalance problems and robustness to data noises (Mellor et al., 2015). In this study, we use RF classifier to classify the lidar measurements.

Unlike RF, DBSCAN clustering is an unsupervised algorithm used for unlabeled clustering. It is a popular density-based data clustering algorithm proposed by Ester et al. (Ester et al., 1996). The algorithm uses a simple minimum density level estimation, and the objects with a density exceeding a threshold for a number of neighbored data (minPts), within a radius ε, will be considered as a core point of a group (Schubert et al., 2017). The algorithm can be used to find areas that satisfy the minimum density and separate areas of different densities. (Farhani et al., 2020, p.1) used the DBSCAN method successfully to identify the anomalies of a lidar data set, which in their case were bio-mass burning aerosols. We use the DBSCAN with a conventional CNR filter to identify and label the lidar noise data.

We divide this study into two tasks, two steps and two models. Task 1: to identify noise; Task 2: to classify non-noise measurements. The two steps are: step 1: label the training dataset, using DNSCAN algorithm, conventional CNR threshold and conventional LUT method with some manual corrections on obvious odd values; step 2: train two models, noise discrimination model and classification model, with the prepared dataset using RF algorithm. These two models can fulfill the tasks raised above accordingly, and with two of them we can classify the lidar data. Besides different labelling methods, another reason for classify the lidar data with two models is the fact that the amount of noise data points is normally much larger than non-noise data points. That results in a decreased performance of the lidar signal classification model because the noise would dominate the classification. The details of the two models are explained in the following sub-sections.

a. Noise discrimination model

The noise of the lidar data is normally identified by CNR thresholds (Boquet et al., 2016; Gryning et al., 2016, 2017). In Iceland, the data quality within the boundary layer is mostly good, and the noise dominates the measurements above the boundary layer, except for the measurements of clouds and precipitation. However, in operation we found the method of CNR filtering not optimal (Yang et al., 2020a) as the data quality and CNR value are not strictly linear correlated. In some cases, the CNR value increases with height in the troposphere, which is unrealistic since fewer aerosols are expected at higher altitudes. Also, there are cases when the noise signals ‘sparks’ an unexpected high CNR value, which will be kept even after the CNR filtering. The CNR value of the cloud measurements, especially high clouds, are normally lower than the signal within the boundary layer, which makes it difficult to find the ´boundary´ between clouds and noises. Here we introduce a new method to optimize noise identification.

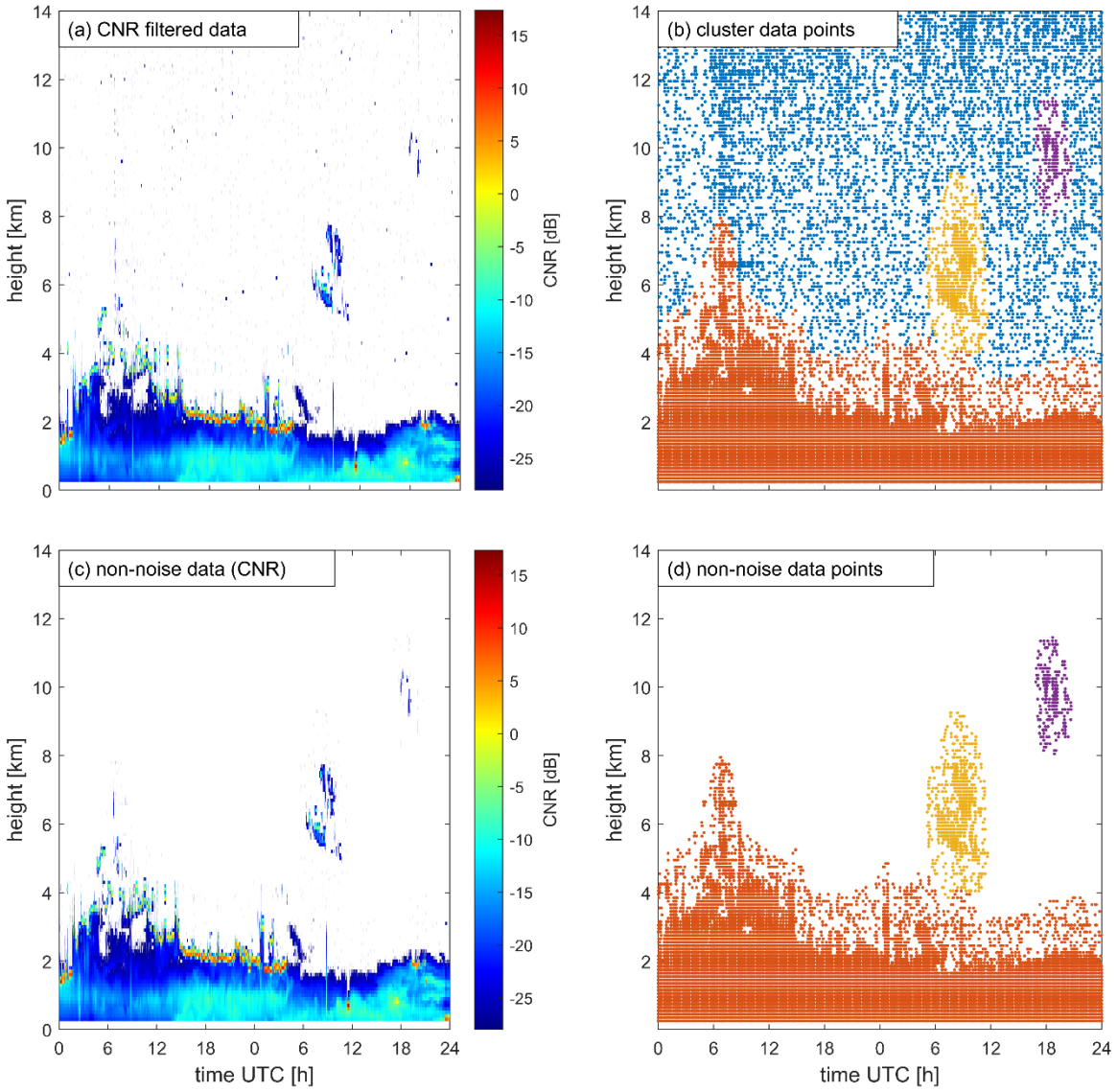

Figure 4.1 Preparing data for training the noise discrimination model with the DBSCAN clustering algorithm. The left panel (a, c) is the CNR data while the right panel (b, d) is the clustered data points. All data are collected on July 31 and August 1, 2019. (a) CNR > -28 dB; (b) same data as in (a), but the colours indicate the data groups clustered by DBSCAN algorithm. Omitting the considered noise data (blue dots in (b)), the filtered data are shown in (c) and (d). The yellow and purple groups are considered as clouds far above the boundary layer, labeled as high clouds for training the classification model; the orange group is clustered as the same group and considered as the non-noise measurements, which will be further classified later. The x-axis shows the time of July 31 and August 1, 2019.

Figure 4.1 illustrates an example of labelling the noise and non-noise data on July 31 and August 1, 2019. We first apply a CNR filter with a threshold of -28 dB, see Figure 4.1(a). The background is not clean which means the filtered data still contains many data points which should be classified as noise. Subsequently, we apply the DBSCAN method to cluster the remaining data (Figure 4.1(b)). The algorithm divides the data points into groups based on their density. Since most of the noise is filtered already, the noise data has a significantly lower density, compared to non-noise data. In this way, we can remove the noise (blue dots in Figure 4.1(b)) from the data. The two separate groups (yellow and purple in Figure 4.1(b)

and (c)) are considered as clouds that are far apart from most non-noise data points within and close to the boundary layer (the orange group Figure 4.1(b) and (c)). By removing all noise data (blue dots), the resulting filtered data has a quite clean background (Figure 4.1(c)). The separated cloud groups (yellow and purple) are labelled as high clouds. Here the definition of 'high clouds' is different from the traditional meteorological definition, that is clouds that are significantly apart from the clouds within and right above the boundary layer. In this case, there are some clouds at 7 UTC July 31, with an altitude of 6 to 8 km, but they can not distinctly be separated from the low clouds within or at the top of the boundary layer (e.g. the clouds at around 2 km in the afternoon of July 31) and not separated by the DBSCAN cluster, we will not treat them as 'high clouds' in this study. These orange data points will be further labeled in the next section and be used as classes to train the classification model. All the data points are now labeled as noise and non-noise. Since the noise is mainly relevant to CNR, we use CNR as the only feature and the noise/non-noise data as the classes to train an RF model. In this way, a noise discrimination model is trained, and the results are shown together with the classification model in section 3.

b. Classification model

In the frame of a supervised machine learning algorithm, RF needs a labeled data set for training. The four-days data used here contains more than 7.8 million data points, which makes it impossible to label all the data points manually. Based on the weather conditions of these four days (Yang et al., 2020b), we divide the lidar data into eight groups: low clouds (group 1); high clouds (group 2); rain (group 3); aerosol type I (group 4); aerosol type II (group 5); aerosol type III (group 6); others (non-noise, group 7); noise (group 8). The noise is determined by CNR and DBSCAN cluster, as described above, and the high clouds are separated as well during the DBSCAN clustering. Low clouds are the easiest to distinguish. The training dates were all collected during summer 2019. The low clouds are all water clouds, with strong backscatter signals and low depolarization ratio, usually found at the top of the boundary layer or close to the surface. They are separated by β and δ thresholds from the red dots in Figure 4.1 (d). We simply label the clouds that are discriminated from noise by DBSCAN methods above the boundary layer as high clouds (Figure 4.1 (d), purple dots). According to (Yang et al., 2020b), three types of aerosols were detected during these four days. All three types are considered to be dust aerosols. Type I was observed on June 14 and June 15, 2019, when the atmosphere was relatively dry, lidar measurements showed high β and high δ values. In the morning of July 31, the atmosphere was dry, and the δ values were high but β values were relatively low. This is probably because the aerosol load was not heavy at the beginning of the dust event, and the particle size was smaller than type I, and we classify this kind of aerosol as type II. In the afternoon of July 31, the relative humidity increased, resulting in lower δ value as the particles absorbed water vapour, and β values were high because of the high aerosol concentration, and we label this kind of aerosol as type III. The type I aerosols are relatively easy to discriminate since both β and δ values are larger than the background, while the type II and III are not, thus there could be some mislabeled type II and type III aerosols.

Rain is the most difficult group to label. Because of its wavelength, the Doppler lidar used here is not sensitive to rain. We classify the rain data based on the low depolarization ratio and a descending movement. If the background depolarization ratio is high, such as in the afternoon of June 15 (see Figure 4.7), it is easier to identify rain, but more difficult when the background depolarization is low as well, such as in the morning of July 31. Even in the afternoon of June 15, there were low clouds after 18 UTC, and it is difficult to distinguish between the low clouds and precipitation. The remaining data points were labeled as others. Some mislabeled data, e.g. the data points that have been labeled as rain without descending

movement or weather observation reports no precipitation, were corrected manually. All these eight classes, the labeling method and the physical explanations can be found in Table 2, and the time-height cross-section of the labeled data is shown in Figure 4.2.

Table 4.2 The eight classes used in this study, and their labeling methods and physical explanation.

Group	Class name	Labeling method*	Physical explanation
1	Low clouds	Highest backscatter coefficient; low depolarization ratio	Clouds within or close to the boundary layer; mostly water clouds in the training data set
2	High clouds	CNR threshold; DBSCAN clustering	Clouds in the free troposphere and at higher altitudes; separated from other non-noise data; mostly ice clouds, but could be water clouds
3	Rain	Descending movement; low depolarization ratio	Rain
4	Aerosol type I	High backscatter coefficient; high depolarization ratio**	Dust particles in dry atmosphere; relative large size, high concentration with a non-spherical shape
5	Aerosol type II	Medium-high backscatter coefficient; high depolarization ratio	Dust particles in dry atmosphere; relative small size, low concentration, with a non-spherical shape
6	Aerosol type III	High backscatter coefficient; medium to high depolarization ratio	Dust particles in a humid atmosphere; relative high concentration, the shape is more spherical
7	Others	Unclassified data points	Other data points except for noise data
8	Noise	CNR threshold; DBSCAN clustering	Noise signals

* In addition, some data points are manually corrected.
** High/medium/low values used for labeling are relative values with manual correction, which could be varied from case to case.

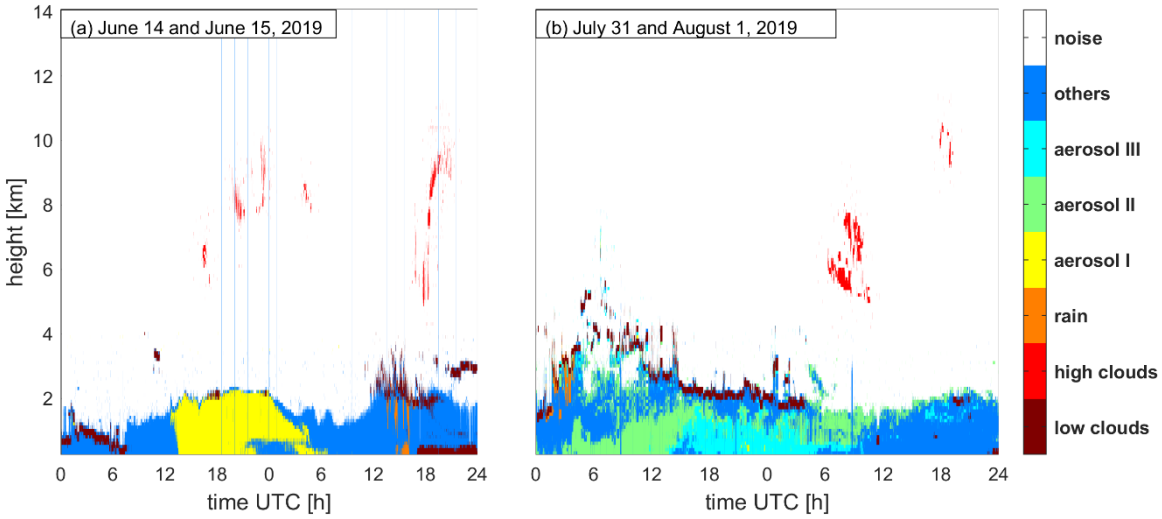

Figure 4.2 Labeled lidar data classes on (a) June 14-15, (b) July 31- August 1, 2019. The vertical blue lines are introduced due to measurement gaps. This data will be used to train and validate the models.

The labeled non-noise data contains the target classes to train, and we select four training features: i) height, ii) CNR, iii) backscatter coefficient (β) and iv) depolarization ratio (δ). The lidar system was re-calibrated and rebooted in July 2019, which leads to a slight difference in the absolute measured value between June and July. Here we normalize each day's lidar data accordingly. Due to the large data size, 10% of randomly selected data points were used to train the model. Figure 4.3 demonstrates the workflow, from the lidar output to the trained models, including the data clustering, labeling and features used for training.

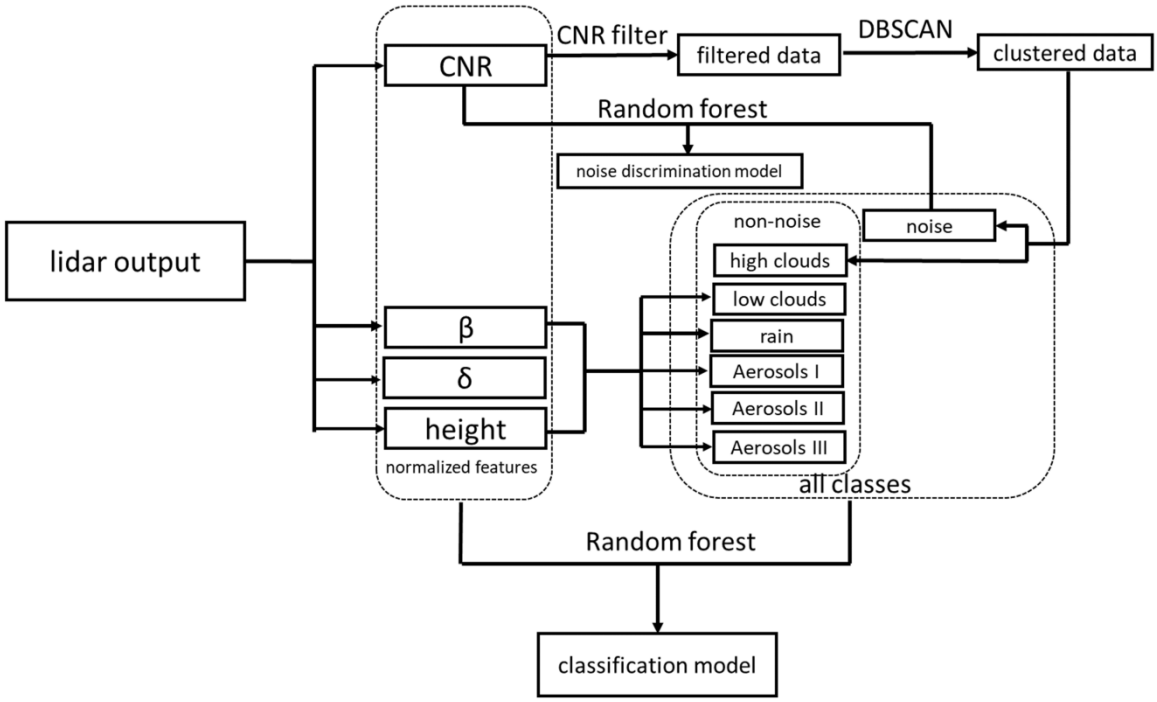

Figure 4.3. Overview of the process of the method. The texts above the arrows are the methods used for that procedure. The noise discrimination model and the classification model are the two trained models.

With the trained noise discrimination model and the classification model, the lidar data is processed in two steps: 1) CNR is used as the input of noise discrimination model, to separate the noise and non-noise data points; 2) the height and normalized CNR, β and δ are used as the input of classification data, to classify the non-noise data points from step one.

4.2.3 Model performance evaluation

One way to evaluate the performance of trained models is to use the confusion matrix (Fawcett, 2006). For instance, one data set consists of a group of data with two predefined classes: positive (P) and negative (N), and they are the true classes. A classifier will classify this data set as two predicted classes as well. If one data point is positive and it is classified as positive, it is counted as a true positive (TP), but if it is classified as negative it is counted as a false negative (FN). Similarly, if one data point is negative and classified as negative it is counted as a true negative (TF) but if it is classified as positive, it is counted as a false positive (FP). In this way, a two-by-two confusion matrix (Figure 4.4) can be used to evaluate the performance of a classification model. More TPs and TNs mean better performance of the classifier. The accuracy is the rate of all data, how much is correctly classified as eq.4.1:

$$accuracy = \frac{TP+TN}{P+N} \qquad \text{eq. 4.1}$$

For a certain class, the true positive rate (TPR, also called hit rate and recall) of a model (Fawcett, 2006) is eq. 4.2:

$$TPR = \frac{correctlyclassifiedpositives}{totalpositives} = \frac{TP}{P} \qquad \text{eq. 4.2}$$

Similarly, the false-positive rate (FPR, also called false alarm rate) of a model (Fawcett, 2006) is eq. 4.3:

$$FPR = \frac{incorrectlyclassifiedpositives}{totalnegatives} = \frac{FP}{N} \qquad \text{eq. 4.3}$$

For the negative class, the true negative rate (TNR, also called specificity) and false negative rate are given a $TNR = \frac{TN}{N}$s: and $FNR = \frac{FN}{P}$. These ratios, TPR, TNR, FPR and FNR, describe the percentages of correctly and incorrectly classified data for each true class. For each predicted class, there are positive predictive values ($PPV = \frac{TP}{TP+FP}$), negative predictive values ($NPV = \frac{TN}{TN+FN}$), false discovery rates ($FDR = \frac{FP}{TP+FP}$), and false omission rates ($FOR = \frac{FN}{TN+FN}$) used to indicate the correctly and incorrectly classification of each predicted class. In Figure 4.4, these ratios are shown in the row/column summary in percentage. For the data set with more than two classes, we can treat each class as a 'positive' class to evaluate, then the row summary will be TPR v.s. FNR and the column summary will be PPV v.s. FDR.

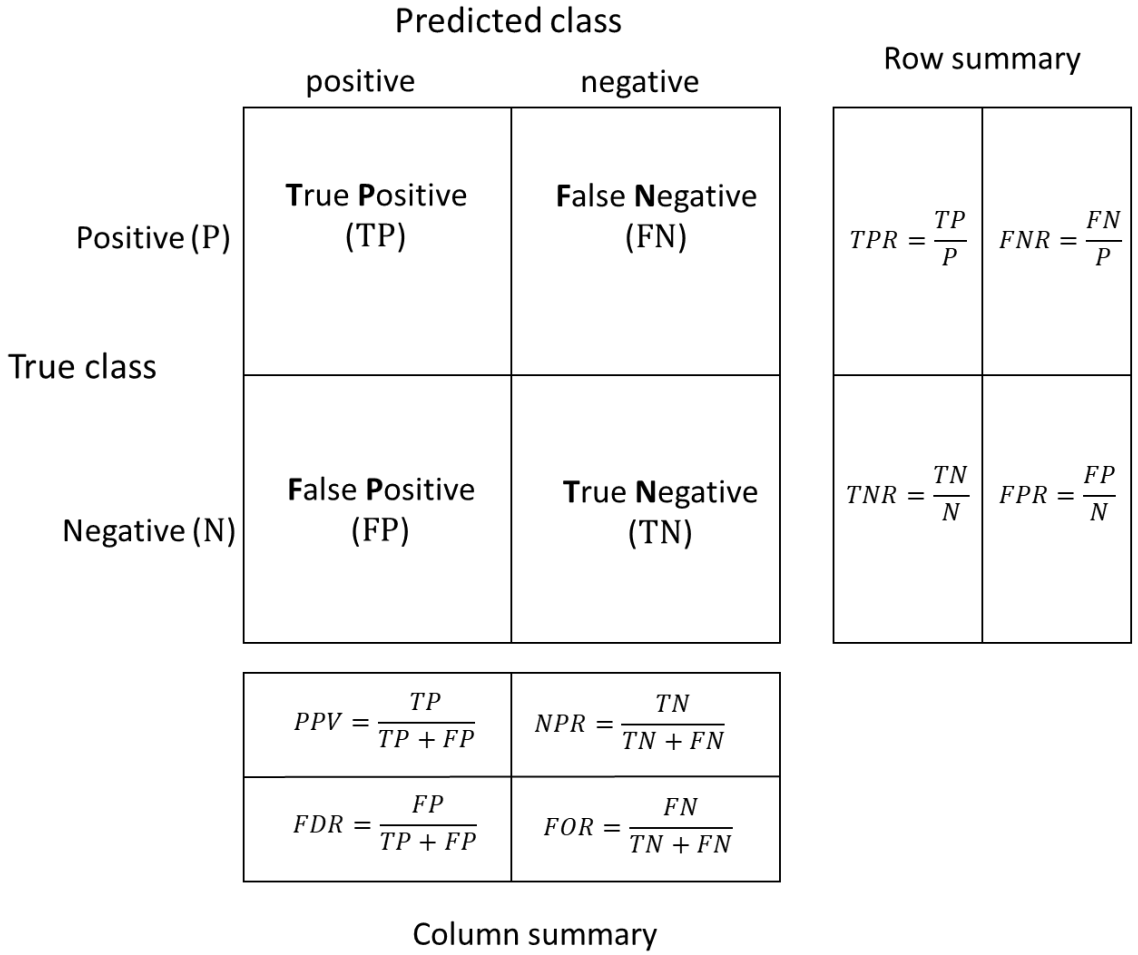

Figure 4.4. A concept diagram of a confusion matrix can be used for evaluating the model prediction. True class is the original labeled class, and the predicted class is the model predicted class. Row summary displays the percentages of correctly and incorrectly classified data for each true class. The column summary displays the percentages of correctly and incorrectly classified data for each predicted class.

4.3 Results

As mentioned in section 4.2, randomly selected 10% of the data points were used for the model training. The remained 90% were used as a testing data set to examine the trained models. The overall accuracy of the trained classification model is 97.3% and 99.3% for the trained noise discrimination model. Figure 4.5 and 4.6 show the confusion matrix of test data and predicted results using the trained noise discrimination model and classification model, respectively. The noise discrimination model worked relatively well on separating the noise and non-noise data with high accuracy. Only a very few noise data (FNR=0.3%) were wrongly classified as non-noise data, and most of them were classified as noise again by the classification model. For the non-noise class, 3.1% of them are classified as noise, but they might not all be wrongly classified. In Figure 4.1(d), there are some points with a lower density, which might be noise but mislabeled.

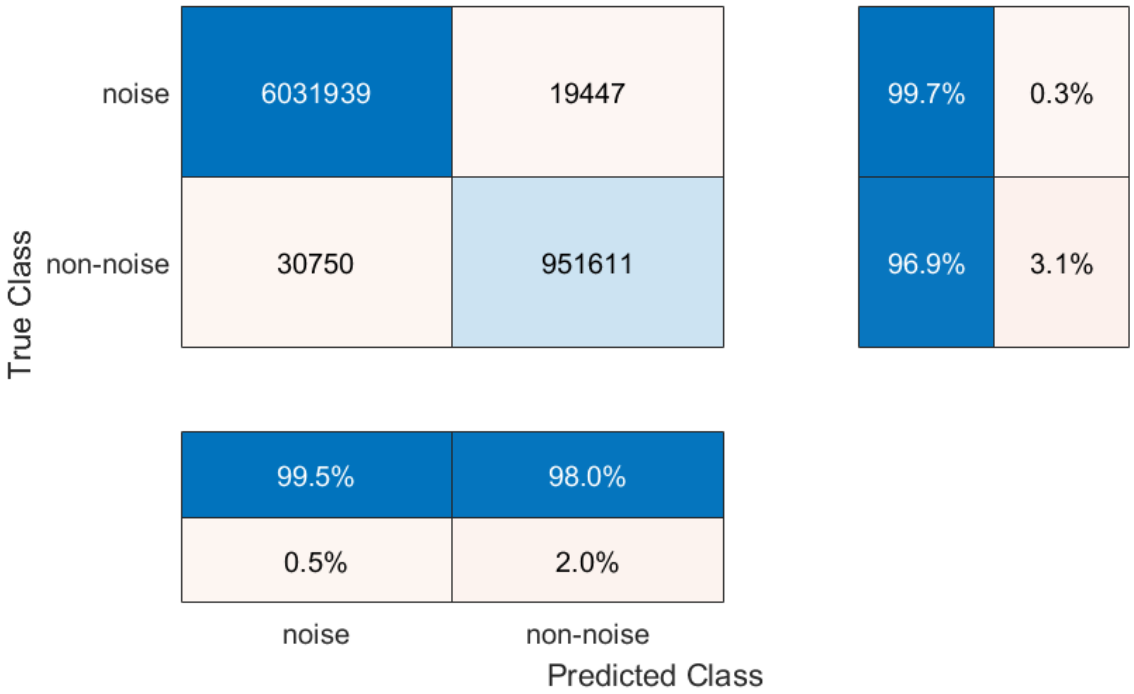

Figure 4.5. The evaluation of the noise discrimination model: the confusion matrix chart of the noise discrimination model with the testing data set, which is 90% of all data points. The number in the matrix is the count of data points for each class, blue colours indicate corrected predicted (TP) and red colours incorrectly predicted data (FN). Darker colour means higher percentage accordingly. The row summary is TPR (blue) and FNR (red) for each true class (row), respectively. The column is PPV (blue) and FDR (red) for each predicted class (column) respectively.

The performance of the classification model varies, depending on the classes. As mentioned above, a small portion of noise data is not identified by the noise discrimination model but most of them (TPR=94.6%) are classified as noise by the classification model. The TPR and PPV value of most classes are larger than 93%, which means the model performs quite well in classifying these classes. The rain class is the worst predicted one, with TPR of 56% but PPV higher with a value of 70.9%. In other words, the model may underestimate the rain data by around 40%, but for each predicted rain data point, we have around 70% confidence that it is rain class.

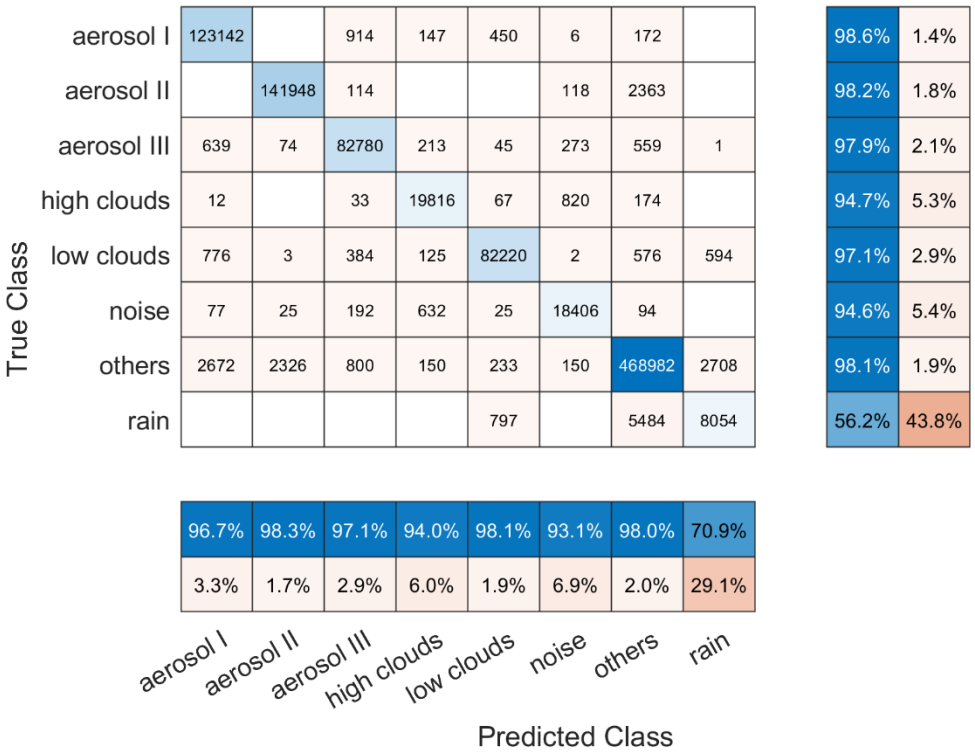

Figure 4.6. The evaluation of the classification model: the confusion matrix chart of the classification model with the testing data set, which is 90% of all data points. The number in the matrix is the count of data points for each class, blue colours indicate corrected predicted (TP) and red colours incorrectly predicted data (FN). Darker colour means higher percentage accordingly. The row summary is TPR (blue) and FNR (red) for each true class (row), respectively. The column is PPV (blue) and FDR (red) for each predicted class (column), respectively.

Since the training and testing data set could be mislabeled, the results by specific cases need to be assessed. Figure 4.7 shows the predicted classes of June 15, 2019, along with CNR, β and δ values. In this case, the trained model did well in predicting the classes of clouds and aerosol type I (high β and high δ), and the rain that fell around 15 UTC. Some data points are classified as aerosol type III (high β and lower δ), but are not labeled in Figure 4.2. We cannot say if these points are wrongly predicted. The depolarization ratio was high in the afternoon, and therefore, these could be some remaining aerosols, not cleaned out by the precipitation. However, these data points stayed at a similar height around 600 m, which is an artifact. That is, the lidar was designed to focus at a certain range to maximize the detection distance, which could lead to an artifact high backscatter coefficient layer.

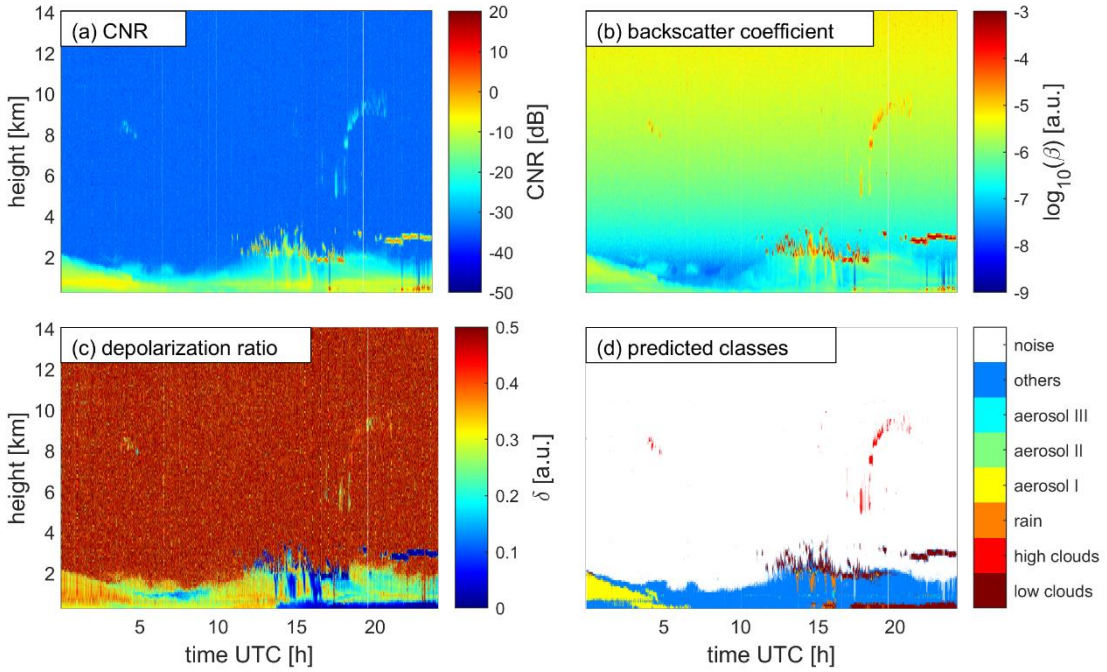

Figure 4.7. The lidar measurements on June 15, 2019 at Reykjavik (a) CNR, (b) backscatter coefficient, (c) depolarization ratio and the machine learning classification result (d) predicted classes.

As mentioned before, the lidar was re-calibrated and rebooted in July 2019. Accordingly, the observations and classification might be influenced by the re-calibration. However, with a normalized input data set, the trained model can classify the measurements well. Figure 4.8 shows the results of July 31. The physical properties of the aerosols are different in this case, compared to those on June 14 and 15. We can find a clear transition from the type II aerosols to the type III aerosols at around 15 UTC. The rain in the morning around 03 UTC was also classified but is underestimated since the rain data points do not reach the surface. In both examples (June 15 and July 31), we find that there are some missing data due to measurement gaps, which are labeled as others in the training data set but are classified as noise signal here.

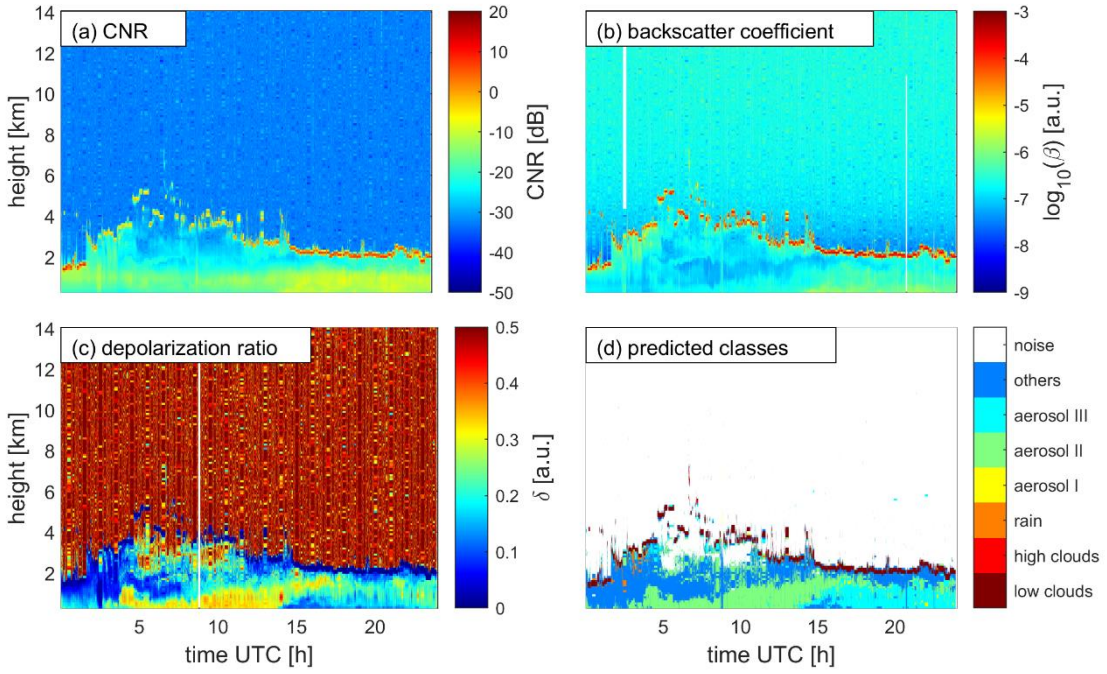

Figure 4.8. The lidar measurements on July 31, 2019, at Reykjavik (a) CNR, (b) backscatter coefficient, (c) depolarization ratio and the machine learning classification result (d) predicted classes.

These trained models have been applied to other data sets. Another dust event was observed from July 9 to 10, 2019. Figure 4.9 presents the results of the two models based on the measurements on July 10. It can be seen that there is a mixture of three types of aerosols in the morning but dominated by type II (high δ and lower β). The dust event lasted until the end of the day.

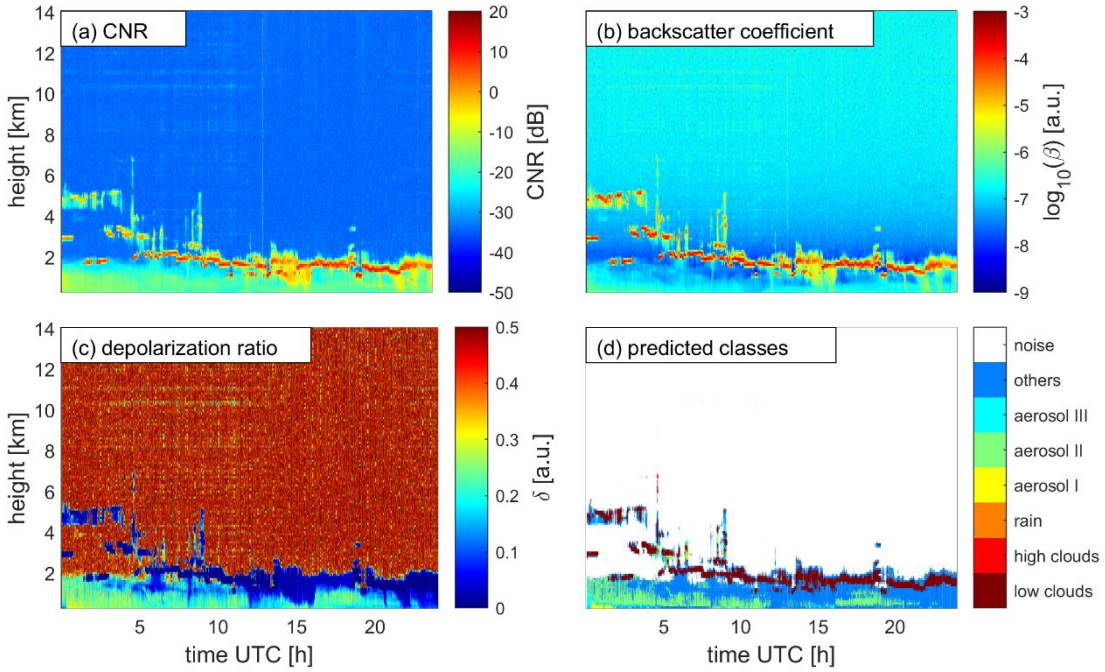

Figure 4.9. The case with the data not used for model training: the lidar measurements on July 10, 2019, at Reykjavik (a) CNR, (b) backscatter coefficient, (c) depolarization ratio and the machine learning classification result (d) predicted classes.

The same models have been applied to the data collected from the lidar at Keflavik, Figure 4.10 shows an example from July 31, 2019. The CNR values of noise data points are slightly lower than from the lidar at Reykjavik, but the models still work well, except for an artifact layer of 'other' class around 600 m above the surface, which as mentioned earlier is a result of the focal effect.

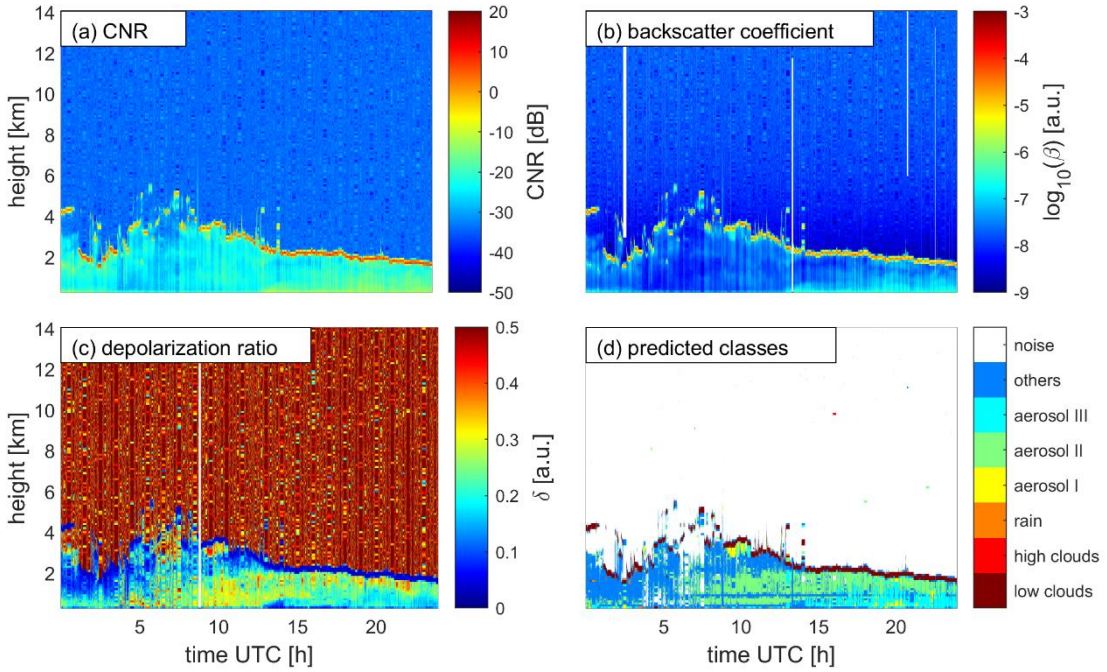

Figure 4.10. The case with the data collected by the Keflavik lidar: the lidar measurement on July 31, 2019 (a) CNR, (b) backscatter coefficient, (c) depolarization ratio and the machine learning classification result (d) predicted classes.

4.4 Discussion and suggestion

One of the well-known features of the machine learning method is that the model itself is a 'black-box' to the user. The models trained here can identify the noise signals very well and performs better than the conventional CNR filtering method. But how did the models achieve that? Did the models apply a similar CNR filtering, but with a more precise threshold than the conventional CNR filtering? Table 4.3 shows the statistics of the data points that are classified as noise by the models from different data sets. If there is a CNR threshold, that would be the maximum value. As we can see, the maximum value varied between data sets. An exception is for the cases of June 15 and July 31 where they have the same maximum value, because they were used for model training together. Besides, these maximums are around -13 to -10 dB, which are much higher than the thresholds normally used, i.e. -32 dB or -28 dB, in previous studies (Boquet et al., 2016; Yang et al., 2020a). To further explain this, a good example is during the morning of July 10, which results can be found in Figure 4.9. There are some horizontal stripes caused by instrumental factors, with higher CNR values that should be classified as noise. With a conventional CNR threshold approach, these signals may exceed the threshold and thus be kept after filtering. The trained models classify them as noise signals successfully. Figure 4.11 presents the model classified data points distribution over different CNR values. Figure 4.11(a) shows all data points on that day, classified by the model as noise and non-noise data. There is a boundary between noise and non-noise data at -28 dB, due to the noise labeling method we use (first filter the data with -28 dB then apply DBSCAN method). But unlike the conventional threshold-based LUT method, there is some overlap around -28 dB. Some classified noise data has CNR values larger than -28 dB and some non-noise data has CNR values lower than that. Figure 4.11(b) presents these data points which are different from the conventional CNR filtering results. These data have a 'long tail', which means the models do not simply filter the data with a CNR threshold, either the same or different from the value we used to apply, but use

a more complicated method.

Table 4.3 CNR value for model classified noise data points.

location	date	CNR of noise points [dB]		
		mean	minimum	maximum
Reykjavik*	06/15/2019	-34.11	-41.29	-10.75
Reykjavik	07/10/2019	-33.88	-41.28	-12.82
Reykjavik*	07/31/2019	-32.40	-40.25	-10.75
Keflavik	07/31/2019	-33.92	-49.79	-12.82

* Data used to train the model

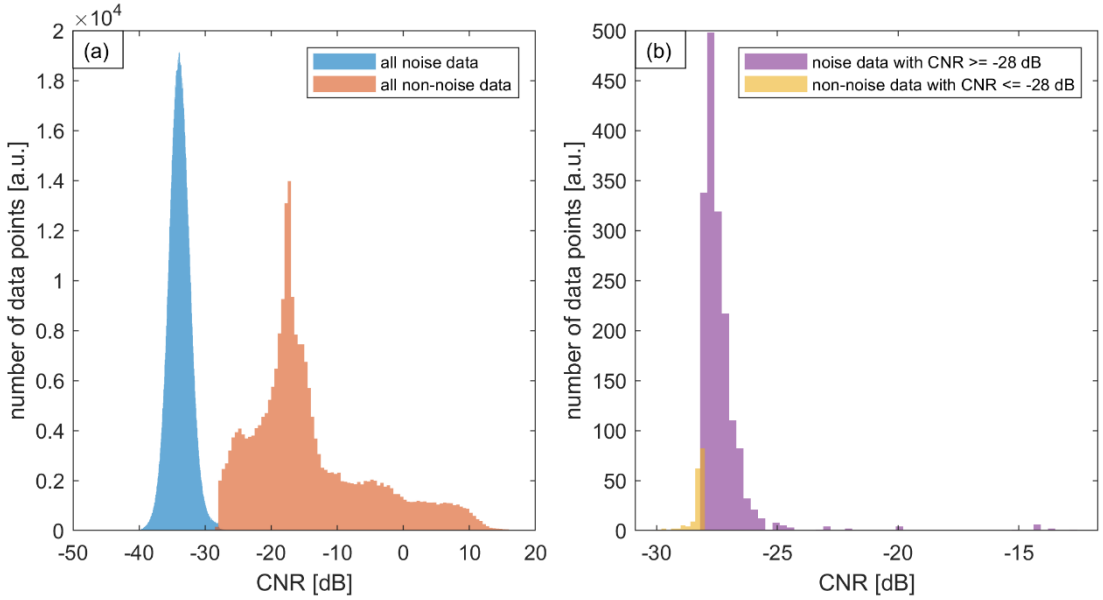

Figure 4.11. Model classified data points distribution as a function of CNR. Data collected on July 10, 2019, at Reykjavik. (a) All data are classified by the model as noise (blue) and non-noise (orange). (b) specifically, only the data points classified differently by the model than by the conventional CNR threshold method: the data points classified as noise but with CNR greater or equal to -28 dB (purple) and the data points classified as non-noise but with CNR lower or equal to -28 dB (yellow).

As a supervised machine learning, the performance of RF is directly related to the labeled data set used for training. The accuracy of the noise discrimination model is higher than the classification model, partly because the noise of lidar measurements is better studied and easier to label, compare to other classes. For non-noise classes, the rain classification has the worst performance, one reason is that this lidar is not sensitive to rain, and the way we label the rain data is mainly by descending movements, which could be hard to distinguish if the β or δ values are similar to that of the background. Also, the rain data are relatively rare in the training data set we use. For rain classification, training on extended data sets with more rain events is needed. Including data from other instruments, such as ceilometer and rain gauge next to the lidar, might also help labeling the rain data. Another way forward is to explore the possibility of detecting solid precipitation in wintertime. For cloud classification, the method in this study is quite promising. However, for now, we only distinguish the low and high clouds based on different labeling methods. A possible improvement to be implemented would be to include more data collected in wintertime with low ice clouds and snow. Hopefully, the model can distinguish water clouds and ice clouds, and it could be more meaningful for meteorological monitoring and research. For the

classification of aerosols, the major challenge is having a better understanding of lidar aerosols measurements. For example, the boundary between aerosol type II and III on July 31 is not entirely clear and we do not know the exact physical difference between these aerosol types yet. Unlike type I, type II and III are aerosols considered sharing the same origin, which is the west of the Icelandic highlands. The main difference is due to the i) weather conditions and ii) aerosols concentration: type II had a lower concentration in a relatively dry atmosphere, so the δ value was high but β value was lower, while type III had a higher concentration in a more humid atmosphere. These features are not necessary for aerosols classification, any particles with similar observations could be identified as these types of aerosols, and this can be checked in operations. For possible eruptions in Iceland, the two models can identify the signals from volcanic ash with similar properties as these three types of aerosols but may miss the ash particles that are different. In general, a larger data set with more precise labels is recommended for improving the performance of the lidar classification model. For the 'others' class, which is considered as the observations when the backscattered lidar signal is strong enough (not noise), and no special phenomenon (clouds, rain, aerosols) was identified, i.e. the air should be relatively clean air within the boundary layer. As we mentioned above, the rain class was underestimated, which means some rain data was classified as others. Besides the rain, some low clouds are also difficult to distinguish and label, which means some low clouds may be mislabeled and classified as others. However, compared to the rain class, this mislabel issue is of little importance, since the lidar signal is more sensitive to cloud than rain droplets. A better labeling data set could improve this.

Neither model uses measurement time as the input feature, that is the classification is not time-dependent. This means that these models can be deployed for real-time classification. This has been examined by compiling a profile-by-profile classification (not shown). The features of the classification model are normalized, because the lidar calibrations are different in June and July 2019. From an operational perspective, if a lidar has stable operations, the model can be re-trained without normalization. Otherwise, the newly measured data need to be normalized with the data measured 6-24 hours before the event. What also needs to be kept in mind for applying this method is that the models are sensitive to lidar calibration parameters, so a well-calibrated lidar system is needed.

Based on our results it is advisable to apply the presented machine learning algorithms during operations and explore the application on a larger data set, with more phenomena, including winter measurements, when the boundary layer can be shallower and the precipitation liquid and/or frozen. This would lead to a continuously improved classification of the lidar observations.

4.5 Conclusion

In this study, we applied machine learning methods to classify the signals retrieved from lidar measurements in Iceland. The first challenge is to label the lidar data for the supervised machine learning algorithm. We used an unsupervised data clustering method, DBSCAN, and combined it with the conventional threshold-based method and manual correction. We applied the method to classify four days of data, obtained during two dust events in 2019. Subsequently, we use this labeled data set to train two models, the noise discrimination model and the classification model with the RF algorithm. With these two trained models, we can accurately identify the noise data, and classify the lidar data into eight classes, including three types of aerosols, two types of clouds and rain. For all classes except rain,

the true positive rate is higher than 94%, however the model is underpredicting rain. In most cases, the model can identify rain correctly, but cannot identify all rain data points. The accuracy of model prediction is directly related to labeling accuracy. With more accurate labeled lidar data, the classification model can be further improved. A larger data set with more and different weather conditions may also improve the performance of the model. In addition, the calibration and correction of lidar data can also affect the results. We found an artifact layer at around 600 m due to the lack of focal correction of lidar depolarization channel in some cases.

This method has been tested on different data sets for different dates and events as well as from two identical Doppler lidars in Iceland. It proves that the machine learning method can be used for the classification of lidar measurements.

Machine learning algorithms depend on the training data sets. Based on our results we conclude that a continuous application of new training data would improve the results further. Accordingly, the presented algorithms may be useful to interpret in real-time lidar observations and provide valuable information to end-users, such as aviation service providers and air quality controllers.

4.6 References

Ansmann, A. and Müller, D.: Lidar and Atmospheric Aerosol Particles, in: Lidar: Range-Resolved Optical Remote Sensing of the Atmosphere, edited by: Weitkamp, C., Springer, New York, NY, 105–141, https://doi.org/10.1007/0-387-25101-4_4, 2005.

Belgiu, M. and Drăguţ, L.: Random forest in remote sensing: A review of applications and future directions, ISPRS J. Photogramm. Remote Sens., 114, 24–31, https://doi.org/10.1016/j.isprsjprs.2016.01.011, 2016.

Bilbro, J., Fichtl, G., Fitzjarrald, D., Krause, M., and Lee, R.: Airborne Doppler Lidar Wind Field Measurements, Bull. Am. Meteorol. Soc., 65, 348–359, https://doi.org/10.1175/1520-0477(1984)065<0348:ADLWFM>2.0.CO;2, 1984.

Boquet, M., Royer, P., Cariou, J.-P., Machta, M., and Valla, M.: Simulation of Doppler Lidar Measurement Range and Data Availability, J. Atmospheric Ocean. Technol., 33, 977–987, https://doi.org/10.1175/JTECH-D-15-0057.1, 2016.

Brakhasi, F., Hajeb, M., and Fouladinejad, F.: Discrimination Aerosol Form Clouds Using Cats-iss Lidar Observations Based On Random Forest And Svm Algorithms Over The Eastern Part Of Middle East, ISPRS - Int. Arch. Photogramm. Remote Sens. Spat. Inf. Sci., XLII-4/W18, 235–240, https://doi.org/10.5194/isprs-archives-XLII-4-W18-235-2019, 2019.

Breiman, L.: Random Forests, Mach. Learn., 45, 5–32, https://doi.org/10.1023/A:1010933404324, 2001.

Chouza, F., Reitebuch, O., Groß, S., Rahm, S., Freudenthaler, V., Toledano, C., and Weinzierl, B.: Retrieval of aerosol backscatter and extinction from airborne coherent Doppler wind lidar measurements, Atmospheric Meas. Tech., 8, 2909–2926, https://doi.org/10.5194/amt-8-2909-2015, 2015.

Di Noia, A. and Hasekamp, O. P.: Neural Networks and Support Vector Machines and Their Application to Aerosol and Cloud Remote Sensing: A Review, in: Springer Series in Light Scattering: Volume 1: Multiple Light Scattering, Radiative Transfer and Remote Sensing, edited by: Kokhanovsky, A., Springer International Publishing, Cham, 279–329, https://doi.org/10.1007/978-3-319-70796-9_4, 2018.

Dubayah R. O. and Drake J. B.: Lidar Remote Sensing for Forestry, J. For., 98, 44–46, https://doi.org/10.1093/jof/98.6.44, 2000.

Ester, M., Kriegel, H.-P., Sander, J., and Xu, X.: A density-based algorithm for discovering clusters in large spatial databases with noise, in: Proceedings of the Second International Conference on Knowledge Discovery and Data Mining, Portland, Oregon, 226–231, 1996.

Farhani, G., Sica, R. J., and Daley, M. J.: Classification of Lidar Measurements Using Supervised and Unsupervised Machine Learning Methods, Atmospheric Meas. Tech. Discuss., 1–18, https://doi.org/10.5194/amt-2019-495, 2020.

Fawcett, T.: An introduction to ROC analysis, Pattern Recognit. Lett., 27, 861–874, https://doi.org/10.1016/j.patrec.2005.10.010, 2006.

Gao, H., Cheng, B., Wang, J., Li, K., Zhao, J., and Li, D.: Object Classification Using CNN-Based Fusion of Vision and LIDAR in Autonomous Vehicle Environment, IEEE Trans. Ind. Inform., 14, 4224–4231, https://doi.org/10.1109/TII.2018.2822828, 2018.

Groß, S., Tesche, M., Freudenthaler, V., Toledano, C., Wiegner, M., Ansmann, A., Althausen, D., and Seefeldner, M.: Characterization of Saharan dust, marine aerosols and mixtures of biomass-burning aerosols and dust by means of multi-wavelength depolarization and Raman lidar measurements during SAMUM 2, Tellus B Chem. Phys. Meteorol., 63, 706–724, https://doi.org/10.1111/j.1600-0889.2011.00556.x, 2011.

Gryning, S.-E., Floors, R., Peña, A., Batchvarova, E., and Brümmer, B.: Weibull Wind-Speed Distribution Parameters Derived from a Combination of Wind-Lidar and Tall-Mast Measurements Over Land, Coastal and Marine Sites, Bound.-Layer Meteorol., 159, 329–348, https://doi.org/10.1007/s10546-015-0113-x, 2016.

Gryning, S.-E., Mikkelsen, T., Baehr, C., Dabas, A., Gómez, P., O'Connor, E., Rottner, L., Sjöholm, M., Suomi, I., and Vasiljević, N.: Measurement methodologies for wind energy based on ground-level remote sensing, in: Renewable Energy Forecasting, Elsevier, Sawston, Cambridge, 29–56, https://doi.org/10.1016/B978-0-08-100504-0.00002-0, 2017.

Haarig, M., Ansmann, A., Gasteiger, J., Kandler, K., Althausen, D., Baars, H., Radenz, M., and Farrell, D. A.: Dry versus wet marine particle optical properties: RH dependence of depolarization ratio, backscatter, and extinction from multiwavelength lidar measurements during SALTRACE, Atmospheric Chem. Phys., 17, 14199–14217, https://doi.org/10.5194/acp-17-14199-2017, 2017.

Kotsiantis, S. B., Zaharakis, I. D., and Pintelas, P. E.: Machine learning: a review of classification and combining techniques, Artif. Intell. Rev., 26, 159–190, https://doi.org/10.1007/s10462-007-9052-3, 2006.

Leosphere, Inc: WINDCUBE 100s-200s User Manual, 2013.

Liu, B., Xu, Z., Kang, Y., Cao, Y., and Pei, L.: Air Pollution Lidar Signals Classification Based on Machine Learning Methods, in: 2020 39th Chinese Control Conference (CCC), 2020 39th Chinese Control Conference (CCC), 13–18, https://doi.org/10.23919/CCC50068.2020.9189314, 2020.

Maxwell, A. E., Warner, T. A., and Fang, F.: Implementation of machine-learning classification in remote sensing: an applied review, Int. J. Remote Sens., 39, 2784–2817, https://doi.org/10.1080/01431161.2018.1433343, 2018.

Mellor, A., Boukir, S., Haywood, A., and Jones, S.: Exploring issues of training data imbalance and mislabelling on random forest performance for large area land cover

classification using the ensemble margin, ISPRS J. Photogramm. Remote Sens., 105, 155–168, https://doi.org/10.1016/j.isprsjprs.2015.03.014, 2015.

Ólafsson, H., Furger, M., and Brümmer, B.: The weather and climate of Iceland, Meteorol. Z., 16, 5–8, https://doi.org/10.1127/0941-2948/2007/0185, 2007.

Schubert, E., Sander, J., Ester, M., Kriegel, H. P., and Xu, X.: DBSCAN Revisited, Revisited: Why and How You Should (Still) Use DBSCAN, ACM Trans. Database Syst., 42, 19:1-19:21, https://doi.org/10.1145/3068335, 2017.

Thobois, L., Cariou, J. P., and Gultepe, I.: Review of Lidar-Based Applications for Aviation Weather, Pure Appl. Geophys., 176, 1959–1976, https://doi.org/10.1007/s00024-018-2058-8, 2019.

Yang, S., Petersen, G. N., Löwis, S. von, Preißler, J., and Finger, D. C.: Determination of eddy dissipation rate by Doppler lidar in Reykjavik, Iceland, Meteorol. Appl., 27, e1951, https://doi.org/10.1002/met.1951, 2020a.

Yang, S., Preißler, J., Wiegner, M., von Löwis, S., Petersen, G. N., Parks, M. M., and Finger, D. C.: Monitoring Dust Events Using Doppler Lidar and Ceilometer in Iceland, Atmosphere, 11, 1294, https://doi.org/10.3390/atmos11121294, 2020b.

Zeng, S., Vaughan, M., Liu, Z., Trepte, C., Kar, J., Omar, A., Winker, D., Lucker, P., Hu, Y., Getzewich, B., and Avery, M.: Application of high-dimensional fuzzy k-means cluster analysis to CALIOP/CALIPSO version 4.1 cloud–aerosol discrimination, Atmospheric Meas. Tech., 12, 2261–2285, https://doi.org/10.5194/amt-12-2261-2019, 2019.

Chapter 5

Conclusions and outlook

This Ph.D. thesis investigates how Leosphere WindCube 200S Doppler lidar can enhance aviation safety and meteorology research in Iceland, by detecting and monitoring the wind field and atmospheric aerosols. The results suggested that using Doppler lidar in Iceland can identify hazardous phenomena, e.g. severe turbulence, high-concentration aerosols, and the end-users can easily recognize such information with the help of artificial intelligence.

5.1 Atmospheric turbulence measurement

An algorithm has been developed to retrieve the EDR as the turbulence intensity indicator, from conic-shaped VAD scans, based on the Kolmogorov theory. The results of this algorithm have been compared with the retrieval using vertical scans, and it shows that EDR has been successfully retrieved, under different weather conditions. Furthermore, different data screening thresholds (CI v.s. CNR, multiple thresholds values), calculation approaches (azimuthal v.s. longitudinal), scan strategies (low elevation angle v.s. high elevation angle), have been compared and discussed. Our research suggested taking a CNR threshold of -32 dB, combined with CI to filter the lidar data for wind measurement. For a certain time, the longitudinal approach can provide a horizontal distribution of atmospheric turbulences, while the azimuthal approach delivers a more accurate result for time-height cross-section analysis. The low-elevation angle scans come with a higher vertical resolution, but higher uncertainty for further range gates. We recommend combining the two elevation angle scans: low elevation angle scan for measurement close to the surface and the instrument but high elevation angle scan for further range gates.

5.2 Airborne aerosol detection

To detect the atmospheric aerosols in Iceland, two types of lidar: ceilometer and Doppler wind lidar have been used, and supplemented with other instruments, i.e. sun-photometer, radio sounding, webcam, and particulate monitor. It is the first time to explore the ability to detect aerosols with WindCube 200S Doppler lidar with depolarization measurement, as well as the first time to compare the ceilometer and Doppler lidar measurement in Iceland. A whole process has been developed to calibrate and correct the ceilometer and Doppler lidar measurement for aerosol detection. The results reveal that both instruments can detect the re-suspended dust aerosols in Iceland, with similar temporal and spatial distribution, but different absolute backscatter coefficient values. The difference can be explained as the varied wavelength of the two instruments.

Besides, the lidar measurements are directly related to the physical properties of the particles, such as their shape and size. These physical properties, on the one hand, depending

on the dust origins, on the other hand, could be affected by the weather conditions, specifically the relative humidity. When the air is humid and the particles condense, the aerosols particles are more visible from the background signal by backscatter coefficient measurements compared to depolarization ratio measurements.

5.3 Classification with machine learning

To make it easier for the end-users of the lidar data, e.g. air traffic controllers, weather forecasters, a classification algorithm is expected. Considering the conventional method may need a lot of calibration work for different lidar systems as well as the training for the lidar users, here we explored the use of the machine learning method to classify the lidar measurements. We combined DBSCAN, an unsupervised machine learning algorithm, and radon forest, a supervised machine learning algorithm, to discriminate the noise data and classify the non-noise data points. The DBSCAN method has been applied together with the conventional CNR filers to separate the noise v.s. non-noise data. Then the dataset has been further labelled based on meteorological analysis. The labelled data has been used to train a noise discrimination model and a classification model. The data collected during the dust events in 2019 (June 14, June 15, July 31 and August 1) at Reykjavik has been used to train (10% of the total) and verify (90% of the total) the models. The Results suggested that the models can predict most of the identified classes, including noise, aerosols, clouds, with high accuracy, but relatively low accuracy on the classification of the measurement of rain. The models have been applied on other datasets, including the data from the lidar at Keflavik, and most of them show a similar performance with the training dataset. And in some cases, the noise discrimination model can perform better than the conventional CNR filtering method when there are some distortion or artifact value in the dataset.

5.4 Outlooks

As the first scientific project to explore the potential of using the Doppler lidar in Iceland, we can conclude that the Doppler lidars can provide valuable information regarding the wind fields, severe turbulence, and aerosol-rich layers. For future studies regarding these topics, these options can be taken as we suggest:

Applying a more precise data filtering method for the turbulence retrieval, maybe the machine learning approach since it has already shown a good potential on this;

Combining the remote sensing method and the laboratory study on the aerosol particles, to find out how the physical properties of particles can affect the lidar measurements;

Extrapolate the machine learning approach on more datasets to explore how robust are the models and how can we improve them;

Include more weather phenomena, i.e. snow, hail, in the machine learning models to make sure the models can be fully used in Iceland

In general, the Ph. D. projects proves that the Doppler lidar can significantly enhance aviation safety in Iceland by measuring atmospheric turbulence and aerosols. The lidar

measurements can provide substantial information to the air traffic controller, weather forecaster, and more stakeholders. The project also evaluated the performance of the lidar systems in Iceland, which could be the fundamental of future works.

School of Technology
Reykjavík University
Menntavegur 1
101 Reykjavík, Iceland
Tel. +354 599 6200
Fax +354 599 6201
www.ru.is